Ph.D. DISSERTATION

Microstructural Study on Heterostructures of TiO_2 and Two-Dimensional Transition Metal Disulfides for Solar Water Splitting

물분해 광전극 응용을 위한 MoS_2/TiO_2 이종계면의 미세구조 분석에 관한 연구

By

Seung-Pyo Hong

February 2018

DEPARTMENT OF MATERIALS SCIENCE AND ENGINEERING

COLLEGE OF ENGINEERING

SEOUL NATIONAL UNIVERSITY

Microstructural Study on Heterostructures of TiO_2 and Two-Dimensional Transition Metal Disulfides for Solar Water Splitting

Advisor: Prof. Ho Won Jang

By

Seung-Pyo Hong

A thesis submitted to the Graduate Faculty of Seoul National University
in partial fulfillment of the requirements
for the Degree of Doctor of Philosophy
Department of Materials Science and Engineering

February 2018

Approved

By

Chairman of Advisory Committee: Jin Young Kim
Vice-Advisory Committee: Ho Won Jang
Advisory Committee: Jeong-Yun Sun
Advisory Committee: Byoung Woo Kang
Advisory Committee: Junwoo Son

Abstract

In order to achieve the superior performance photoelectrode, TiO_2 nanorods were synthesized on F doped SnO_2 (FTO) substrates; TiO_2 single crystal with (001), (101), and (110) substrates; and *p*-type Si substrates by the hydrothermal method. The growth mechanism of TiO_2 nanorods is proposed by the hydrothermal processes with various synthesis condition, such as the temperature and time, the concentration of the precursor and HCl, and the growth on the diverse substrates. During the hydrothermal synthesis, the morphology of the TiO_2 nanorods are strongly depends on the surface energy of each lattice plane of the TiO_2 and the chemistry of the synthesis solution. Most of all, those two parameters can be controlled by the concentration of HCl in the solution simultaneously. The morphological evolutions of the TiO_2 nanorods with the HCl concentration were confirmed. In terms of the formation of the TiO_2 nanorods, the rod shape can be constructed by the generation of four TiO_2 {110} planes, which exhibit the lowest surface energy, and preferential growth on {001} planes, which possess the highest surface energy, resulting in growth along the [001] direction. It has been revealed that the HCl concentration is the most effective parameter to control the morphology of the TiO_2 nanorods. The {110} planes of the TiO_2 nanorods were stabilized by the selectively absorption of the Cl^- ions on the {110} planes, resulting in the preferential growth along the [001] direction. Furthermore, TiO_2 nanorods were grown on the *p*-Si by the hydrothermal method to reduce the disadvantages of *p*-Si as a photocathode on the photocorrosion and high reflectance. The photoelectrochemical (PEC) performances were effectively enhanced. It can be elucidated that the hydrothermally grown TiO_2 nanorods can act both as the passivation and the antireflection layer. In addition, MoS_2, which is known as one of the 2D-TMD materials with excellent photocatalytic properties, was decorated on TiO_2 nanorods by the hydrothermal synthesis. Both the photocurrent and overpotential were further enhanced after the MoS2 decoration. By

the high resolution-transmission electron microscope (HR-TEM), the fast furrier transformation (FFT), and X-ray photoelectron spectroscopy (XPS) analysis, the MoS_2 synthesized by the hydrothermal method was confirmed. The formation of the MoS_2/TiO_2 heterojunction was verified by ultraviolet photoemission spectroscopy (UPS) analysis.

Seung-Pyo Hong

Table of Contents

List of Tables

List of Figures

Chapter 1

Introductions

1.1 Background

In the late 18th and early 19th centuries, human beings, which formed the agricultural society, have undergone the First Industrial Revolution by the development of the steam engine and industrialization centered on consumer goods and light industries. After this period, in the mid-19th century the internal combustion engine was developed, resulting in the Second Industrial Revolution characterized by the expansion of new industries for the mass production such as steel, petroleum and electricity. As a result, the demand and usage of fossil fuels such as coal and oil had explosively soared. Since the First Industrial Revolution, and until now human beings have begun to worry about new issues of energy problems. Since the 1970s, in earnest, since the 1990s to the present, we have lived in the era of the Third Industrial Revolution. The global concerns about the environmental problems and the demand for new renewable energy to solve them, which have not been worried about, have come to the fore. Even if it is not only the problem of an exhaustion of the fossil fuels, the climate change issues such as the global warming by the use them have been risen. As an energy conversion and use through the steam engines and the internal combustion engines in the First and Second Industrial Revolutions have made most of the industrial changes and innovations, respectively. New renewable energy sources to solve the problems and methods for an efficient use, a conversion and storage of energy should be discovered. Due to the objectives as stated above, at the era of the Third Industrial Revolution, a key parameter of the renewable energy is to establish the fundamental infrastructures of the renewable energy fields and their related the production, conversion, and storage technologies. The various efforts and dedications to innovate diverse renewable energy sources (hydropower, wind, geothermal, and hydrogen etc.) have been sustained. However, because of its superiority the hydrogen production can be the most attractive and potential solution in terms of the clean and renewable energy source

1.2 Hydrogen Production for the Renewable Energy Source

1.2.1 Pathways for Hydrogen Production

Hydrogen production as a renewable energy source has more considerable merits because the hydrogen is inexhaustible and power density is high. Most of all, in terms of cleanness, one important feature is that the only product after combustion of the hydrogen is water. The hydrogen can be produced by several methods as shown in Figure 1.1. The pathways for the hydrogen production can be classified into two types: 1) steam reforming, 2) water splitting. Firstly, the steam reforming, accounts for about 95% of the total producing hydrogen, is the method to produce H_2 and CO by reacting steam with methane in natural gas and. The general reaction formula is as follows.

$$CH_4 + H_2O \leftrightarrow CO + 3H_2 \qquad \text{Eq. 1.1}$$

$$CO + H_2O \leftrightarrow CO_2 + H_2 \qquad \text{Eq. 1.2}$$

This reaction is only possible at a high temperature of about 700–1100 ℃, and the production efficiency is known to be about 65–75 %. Although it is the most widely used method of the hydrogen production, this method has a disadvantage that there is a problem of greenhouse gas emission.

Secondly, the another method to generate the hydrogen is the water splitting. This method can be divided into three different ways; thermolysis, electrolysis, and photoelectrochemical water splitting. The three methods have in common with the reaction in which the water is decomposed to obtain the hydrogen. There is a difference among those processes in terms of the energy sources used to split the water into the hydrogen.

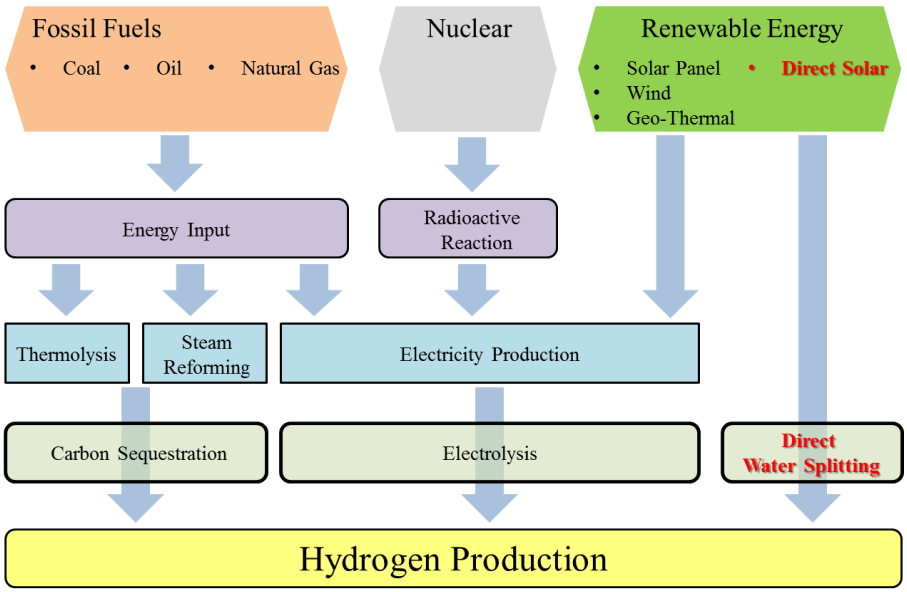

Figure 1.1 Several pathways for the hydrogen production from the various energy sources

First of all, the thermolysis water splitting should be conducted at over 2000 ℃ to decompose the water molecules. In order to achieve that high temperature, numerous quantity of the fossil fuels should be burned. It is well known that the production efficiency of the thermolysis is extremely low. Second, in the electrolysis, the hydrogen and oxygen can be produced at the cathode and anode, respectively by applying a high DC electrical power. To carry out the electrolysis, the extremely high electric power, which is usually provided by the radioactive reactions in nuclear power plants, has to be also supplied. In the water splitting by the upper mentioned two methods; thermolysis and electrolysis, the total production processes are not environmental friendly and are not efficient because they use the fossil and nuclear fuels, resulting in emission of greenhouse gases and in production of radioactive wastes. Thus, the thermolysis and electrolysis are the methods cannot be preferred for the water splitting. Lastly, photoelectrochemical (PEC) water splitting is the method by using the photoactive electrode materials and the solar light only. Hence,

the PEC water splitting has great advantages and potentials because any fossil fuel is not combusted and the extra energy input is not required.

1.2.2 Photoelectrochemical Solar Water Splitting for Hydrogen Production

In terms of the sunlight as an energy source, the solar energy, the energy source of direct solar water splitting for hydrogen production, is enormously irradiated on the earth. In other words, the amount of energy that the sun irradiates to the earth for an hour is greater than the total amount of energy that the earth consumes in a year.[1] By achieving an efficient conversion and utilization directly of the enormous amounts of solar energy or by storing it in another form, the solar water splitting will be a solution to the upcoming energy problems. Direct water splitting has been regarded as one of the more practical and efficient ways to deal with the huge amount of solar power, in which the solar energy is converted and stored in the form of chemical energy.[2] Hence, the hydrogen production as one of the most potential methods to generate the renewable energy, is considered to be the optimum way to solve the several energy issue. After the first report about the Photoelectrochemical of water using TiO_2 as a photoelectrode by Honda and Fujishima,[3] many researchers have focused on the direct solar water splitting.

The direct water splitting has great advantages: the hydrogen is produced from the water and the sun which are the infinite and sustainable natural resources and the only product during burning the hydrogen is the only water without any other greenhouse gases or wastes. Thus, if the effective conversion and storage of the solar energy can be achieved, the clean energy can be produced, stored, transported, and utilized without any harmful byproduct.[4-9] Furthermore, in an economic perspective, extensive system costs in manufacturing and facility construction can be avoided, comparing to other hydrogen production processes.[10] The another requirement for total PEC cell for water splitting is to reduce an intermittent energy supply (to

provide stable and constant energy flux), and to secure the cost-effectiveness of storage of solar energy by maintaining the stability of the electrical system.[7, 11, 12] In terms of materials, the materials for solar water splitting applications should be satisfied with following characteristics: harvesting the broad range of solar spectrum with a high efficiency and rapid charge transfer at the interface.[7]

Even though the production cost of the electrolysis, including photoelectrochemical way is still necessary to secure competitiveness compare to that of thermolysis using fossil fuels,[4, 9, 13] direct solar water splitting will be a sustainable clean renewable energy based on the hydrogen generation, when the scientific and technical advances are accomplished in the energy industry.

1.2.2.1 Basic Principles for the Direct Solar Water Splitting

The direct water splitting, in scientific and engineering points of view, is the process where a water molecule is decomposed using semiconductor materials as a light absorber and an energy convertor into the simplest chemical bond of H_2.[14] In a solar water splitting system, the light with specific wavelength (solar energy) is absorbed and is converted into the chemical energy via the electrochemical reaction. The reaction is composed of following processes. The light from the sun is absorbed and converted at the photoelectrodes, where redox reactions of the water are taken place. Specifically, the reduction of the water at a photocathode (*p*-type photoelectrode) and the oxidation of the water at a photoanode (*n*-type photoelectrode) occur. In other words, the hydrogen is generated at the photocathode (hydrogen evolution reaction: HER) and the oxygen is produced at the photoanode (oxygen evolution reaction: OER). The photoelectrochemical cell can be organized when one of the both photoelectrodes, the counter electrode (CE), and the reference electrode (RE) connected with an external circuit are placed in the electrolyte.

The other feature of the PEC cell is that the reaction happens directly at the interface between the photoactive materials and the liquid electrolyte. Therefore, the hydrogen

and oxygen can be collected separately because the HER and OER occur at the each photoelectrode, respectively. As shown in Figure 1.2, the photons from the incident light are absorbed by the photoactive semiconductor materials and then the electron-hole pairs are generated. Thereby the hydrogen ions (or water) are reduced (or oxidized) by the photogenerated electrons (or holes) at the photocathode (photoanode), respectively.

$$2OH^- + 2H^+ \rightarrow H_2O + {}^1/_2\, O_2 \qquad \text{Eq. 1.3}$$

$$2OH^- + 2H^+ \rightarrow H_2O + {}^1/_2\, O_2 \qquad \text{Eq. 1.4}$$

$$\therefore\ H_2O \rightarrow H_2 + {}^1/_2\, O_2 \qquad \text{Eq. 1.5}$$

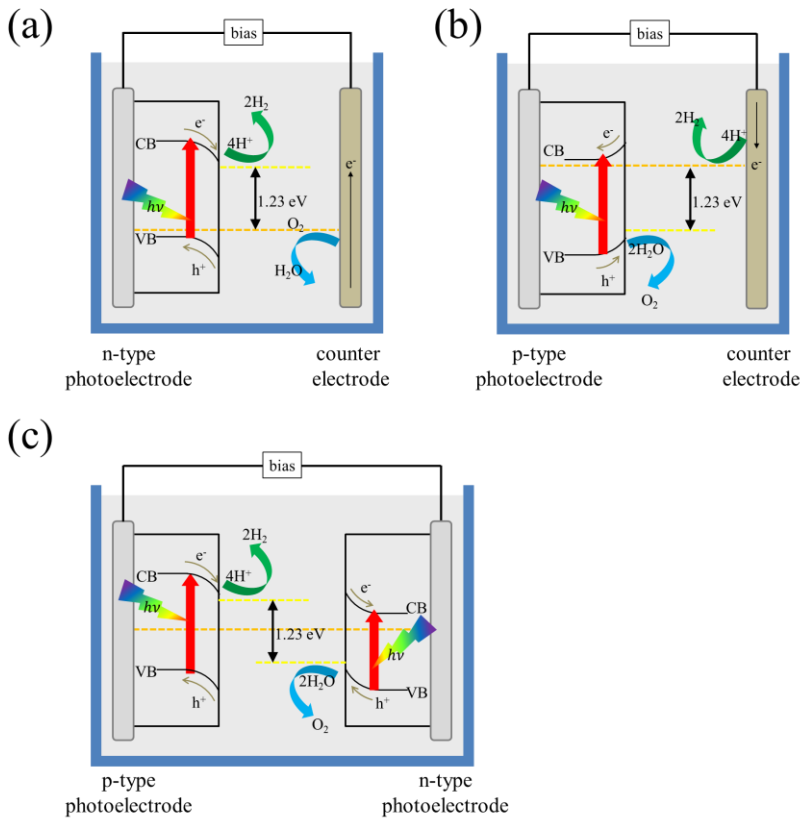

Figure 1.2 Schematics of the photoelectrochemical (PEC) water splitting reactions (a) hydrogen evolution reaction (HER) at a photocathode (b) oxygen evolution reaction (OER) at a photoanode (c) the photocathode and photoanode in tandem configuration

Theoretical standard energy barrier of water oxidation is calculated to be ΔG = 237.12 KJ/mole, which is corresponds to ΔE° = 1.23 V per electron transfer according to the Nernst equations.

$$\Delta E^{o} = E^{o}_{cation} - E^{o}_{anion} = -1.23\ eV \qquad \text{Eq. 1.6}$$

However, the higher potential is required to drive the reaction in a practical PEC water splitting system because the potential loss occurs in the bulk semiconductor electrodes, at the interface between the semiconductors, and the high Gibbs free energy of the photoelectorods for hydrogen/oxygen adsorptions exists. The potential loss (overpotential), which is closely related to the efficiency of the cell, will be discussed in the next section.

Until now, the expensive materials have been used such as (Al)GaAs and GaInP for the photoactive materials or Pt, RuO_2, IrO_2 for the photoactive catalysts. Moreover, strong acidic or basic electrolytes, which cause extra cost for maintaining the facilities and post-processing for the wastes, have been required.[15] Hence, the necessity and importance of the new photoactive materials have been constantly discussed. With regard to the investigation and selection among the photoactive materials, several requirements should be considered. The high enough photocurrent should be generated from the photoactive materials. The high voltage can be accompanied by the low photocurrent. In addition, if the materials have the large band gap, the separation of the electron and hole becomes much easier. However, the spectral match upon the sun light is reduced if the material has a large band gap. Thus, the photoactive materials should have narrow band gap to absorb the large solar spectrum, resulting in the high photocurrent.[16, 17] Another requirement in terms of the band gap for the photoactive materials is that the band gap should be higher enough than the free energy difference, including the overvoltage induced by a surface catalyst for the desired reaction in a given PEC system.[18] In addition, the band edges of the materials should straddle the oxidation and reduction potential of H_2O.[17] In other words, the conduction band (CV) of the photoactive material is more negative than the reduction potential of the water, and the valence band (VB) is more positive than the oxidation potential of the water in the electrochemical energy scale. Figure 1.3 shows the redox potential of the water and a proper band gap of a photoactive semiconductor. The other important requirement is the high efficiency during the photogenerated carriers are converted into the products of the water

splitting. Furthermore, with regard to the economic considerations, high stability in the aqueous solution and low production cost should be secured.[17] In selecting photoactive materials diverse parameters should be carefully considered: a band gap and its proper band edge positions against the redox potential of the water, light absorption in the visible range, production costs, stability in the operating conditions, and overall efficiency etc.[18] For examples, even though the transition metal oxide such as TiO_2 shows the sufficient stability, the only UV light can be absorbed in the total solar illumination due to the large band gap ($E_g = 3.0$ eV in the rutile phase) of the TiO_2. Despite the proper band edge positions with the narrow band gap, such as InP, the stability of is poor in the aqueous environment.[19] By using the III–V semiconductor materials consisting a tandem configuration, the solar-to-hydrogen (STH) efficiency of about 12% has been achieved, which is the highest value reported, however the disadvantage on production cost still remains.[20] Various materials for PEC cell have been studied extensively, but the optimum material has yet been found that fulfills those sensitive requirements.[21] The stability should be ensured in a practical PEC cell because the HER and OER occur directly at the interface between the photoelectrodes and electrolyte, avoiding the photocorrosion. The photocorrosion can take place competitively with the redox reactions of the water if the cathodic (or anodic) corrosion potential is placed inside of the band gap. Due to the fact that the corrosion reaction of the materials generally has low energetics, the photocorrosion can be thermodynamically preferred rather than the redox reactions, resulting in the instability of the photoelectrodes.[22] In order to avoid the photocorrosion, introducing the protecting layer (passivation layer) is one of the promising solution, which will be discussed. In order to reduce the production cost of the hydrogen remarkably, new photoactive materials should be investigated which fulfill the requirements such as not only high STH efficiency, stability but also thermodynamic and kinetic characteristics.[12]

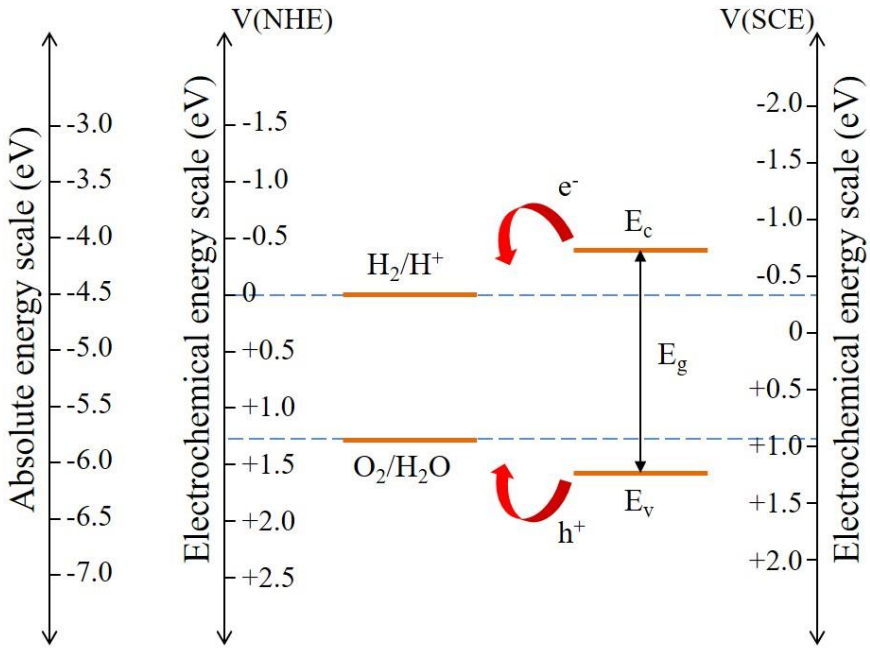

Figure 1.3 Schematic diagram for the solar water splitting in liquid electrolyte with zero pH. The proper positions for the conduction band (E_C) and valance band (E_V) of a photoactive semiconductor vs. absolute energy scale and electrochemical energy scale.

1.2.3 Efficiency of the Photoelectrochemical Cells

For a practical solar water splitting system with a high capacity for the hydrogen generation, the production cost should be significantly reduced. In order to lower the cost, several researchers have reported that to achieve the high solar-to-hydrogen (STH) efficiency which can provide a most powerful driving force into the hydrogen production industries.[23-25] The highest efficiency of the PEC cell composed with one semiconductor/liquid junction system is reported as 12.4%.[20, 26] The theoretical maximum efficiencies calculated with diversion assumptions in a tandem cell configuration are evaluated to 23–32%.[7, 27-30] As stated above, if a material has large enough band gap of which the conduction band (Ec) and valence band (E_V) which are placed between the redox potential of the water, the HER/OER can tack place.

Within this processes, in order to react one of the HER or OER avoiding unnecessary recombination, the photogenerated carriers should be transferred toward the liquid junction and then the desired reaction should be brought about at the surface of the material. The potential loss cannot be avoidable through the electron-transfer processes at each electrode/liquid interface because of the kinetic overpotential for the activating desired reaction. Hence, the energy required for the water splitting at the photoelectrodes are reported as over 1.23 eV resulted from the loss in general.[10, 27] Thus, to minimize the kinetic overpotential is essential to enhance the overall efficiency of a PEC device for the practical applications. In this regard, the evaluation method to estimate the properties of the water splitting devices has been required. The solar-to-hydrogen (STH) efficiency as a universal standard scale is the scientific and appropriate method, which can provide not only the property and limitation, but also the insight of the material itself. Several values have been employed to describe the efficiency of water splitting systems. The overall STH efficiency of the cell is the most important parameter to evaluate the performance of the PEC devices. In fact, because the material system designed can be identified by the highest STH value, each value can be used for comparing the devices each other.[1] However, there are various ways, which can be classified into four, to express the efficiency of the PEC devices. The reason is that there are diverse measurements for evaluating efficiency as follows.[31, 32]

- Solar-to-Hydrogen conversion efficiency (STH)
- Applied Bias Photon-to-current Efficiency (ABPE)
- Incident Photon-to-Current Efficiency (IPCE)
- Absorbed Photon-to-Current Efficiency (APCE)

1.2.3.1 Solar-to Hydrogen Efficiency (STH)

The STH efficiency, which can represent the overall efficiency of the PEC cell at the zero-bias condition and can cover the entire solar irradiation. (e.g., Air Mass 1.5 Global illumination, abbreviated AM 1.5 G),[33-36] is considered to be the most prior method over other values. The "zero-bias" indicates that no voltage between the working electrode (WE) and the counter electrode (CE) is applied, and that the energy source for the overall water splitting process is only supplied by the light. In order to evaluate the direct STH efficiency, the WE and CE are operated under short-circuit condition, so voltages versus the reference electrode (RE) or the open-circuit voltage are not relevant.[31] In addition, the direct STH cannot be measured if the WE and CE are placed in the different pH solutions. Thus, both the WE and CE should be put into the same pH solution. Furthermore, any sacrificial donor or acceptor should not be contained in the electrolyte because the redox reaction cannot reflect the true water splitting if the sacrificial donor or acceptor exist in the electrolyte.

The STH efficiency is defined as the chemical energy of the hydrogen produced divided by the solar energy input from the solar irradiation. The chemical energy of the hydrogen produced can be obtained by multiplying the rate of the hydrogen production and the change in Gibbs free energy per mole of H_2 (ΔG_0= 237 kJ/mole at 25 ℃). In addition, the solar energy input from the solar irradiation can be calculated by multiplying the illumination power density (P_{total}, mW/cm^2) and the area of the WE (cm^2). One important thing is that the illumination source has to fulfill the condition of Air Mass 1.5 Global (AM 1.5 G) G173 standard.[36] Hence, the STH efficiency can be expressed as following equation.

$$\mathrm{STH} = \left[\frac{(\mathrm{mmol\ H_2/s}) \times (237000)(\mathrm{J/mol}) \times \eta_F}{P_{total}(\mathrm{mW/cm^2}) \times \mathrm{Area(cm^2)}}\right]_{\mathrm{AM\ 1.5G}} \qquad \text{Eq. 1.7}$$

In the equation 1.7, the power output is calculated by the measuring true H_2 production rate, which are generally carried out via the gas chromatography or mass spectrometry. Instead of the numerator in the equation 1.7, the power output can be obtained by using voltage, current, and the Faradaic efficiency for hydrogen evolution (η_F) as shown in equation 2.2.

$$\mathrm{STH} = \left[\frac{j_{sc}(\mathrm{mA/cm^2}) \times (V_{redox})(\mathrm{V}) \times \eta_F}{P_{total}(\mathrm{mW/cm^2})}\right]_{\mathrm{AM\ 1.5G}} \qquad \text{Eq. 1.8}$$

In this equation, the current should be normalized by the area of the electrode as a short-current photocurrent density (j_{sc}, mA/cm^2), the V_{redox} is 1.23V ($\Delta E°$ based on the thermodynamic redox potential at 25 ℃). The short-circuit in the PEC devices indicates that the external bias is zero. It is important to note that the photogenerated carriers are equilibrated at the separated redox potentials which correspond to both half-reactions for the water splitting.

1.2.3.2 Applied Bias Photon-to-Current Efficiency (ABPE)

The other efficiency value should be considered if the external bias is applied between WE and CE because it cannot reflect the true solar-to-hydrogen conversion process. From this necessity, new concept of applied bias photon-to-current efficiency (ABPE) has been introduced. When a bias is applied into the device, the consuming current is increased in general. Therefore, even though the measurement of ABPE cannot represent the true solar-to-hydrogen efficiency, it can be a worth parameter for developing photoactive materials. The ABPE can be calculated with following equation

$$\mathrm{ABPE} = \left[\frac{j_{sc}(\mathrm{mA/cm^2}) \times (V_{redox} - V_{app})(\mathrm{V}) \times \eta_F}{P_{total}(\mathrm{mW/cm^2})}\right]_{\mathrm{AM\ 1.5G}} \qquad \text{Eq. 1.9}$$

where j_{sc} is the photocurrent density obtained under an applied voltage V_{app}.

1.2.3.3 Incident Photon-to-Current Efficiency (IPCE)

The Incident Photon-to-Current Efficiency (IPCE), which may also be referred to as the external quantum efficiency (EQE), is the one of the most important values for characterizing a PEC device. This value represents the photocurrent collected per incident photon flux as a function of illumination wavelength. In the ideal case, the maximum possible STH efficiency over the solar spectrum can be estimated by integrating the IPCE data of a device. It is noted that the measuring IPCE should be carried out under zero-bias (2-electrode, short-circuit) condition. Because the three fundamental processes are considered for the IPCE measurement, the IPCE has a great merit. The IPCE can be expressed by using the three processes as follows,

$$\mathrm{IPCE} = \mathrm{EQE} = \eta_{e-h} \cdot \eta_{transport} \cdot \eta_{collection} \qquad \text{Eq. 1.10}$$

where η_{e-h} is the efficiency for electron–hole (e^-/h^+) pairs generation per incident photon flux, $\eta_{transport}$ is charge transport efficiency at the solid–liquid interface, and $\eta_{collection}$ is interfacial charge transfer efficiency. IPCE can be calculated as the following equation.

$$\mathrm{IPCE}(\lambda) = \frac{j_{ph}(\mathrm{mA/cm^2}) \times h \cdot c(= 1239.8)(\mathrm{V \times nm})}{P_\lambda(\mathrm{mW/cm^2}) \times \lambda(\mathrm{nm})} \qquad \text{Eq. 1.11}$$

where j_{ph} is the photocurrent density, h is the Plank's constant, c is the speed of the light, and P_λ is the power of the light at a particular wavelength.

In order to avoid confusing STH or IPCE, the important differences should be recognized.

① STH describes efficiency in terms of power $\left(\frac{\text{power out}}{\text{power in}}\right)$, while IPCE represents $\left(\frac{\text{electrons out}}{\text{photons in}}\right)$.

② STH efficiency is measured under solar-simulated illumination (AM 1.5G), but IPCE can be carried out with any calibrated and monochromatic illumination source.

③ STH should be conducted at the zero-bias condition. However, IPCE can be done with external bias.

1.2.3.4 Absorbed Photon-to-Current Efficiency (APCE)

The efficiency of a PEC device by using STH or IPCE is calculated regardless of the reflected and/or transmitted photons (certain loss of the incident photons). Thus, it can be an advantageous method to understand the inherent properties if the absorbed photons are considered only. This consideration led to the concept of the absorbed photon-to-current efficiency (APCE) based on the photocurrent collected per incident photon absorbed. This is usually used to characterize the photoresponse efficiency of a photoelectrode materials under an applied voltage. In addition, the APEC is regarded as the identical meaning of the internal quantum efficiency (IQE), which can be expressed as

$$\text{APCE} = \text{IQE} = \frac{\text{IPCE}}{\eta_{e^-/h^+}} = \eta_{\text{transport}} \cdot \eta_{\text{interface}} \qquad \text{Eq. 1.12}$$

where η_{e^-/h^+} is the absorptance, which can be defined as the faction of the electron-hole pairs produced per incident photon flux. Because η_{e^-/h^+} describes the first process of the three fundamental processes, and $\eta_{transport}\cdot$ can be obtained. Moreover, if the transport is insufficient and/or the interface kinetics is low, the efficiency could be poor. In addition, η_{e^-/h^+} and IPCE could be almost equal when $\eta_{interface}$ becomes close enough to unity by optimizing a redox couple. In ideal case, $\eta_{transport}$ is independent of the redox couple. However, the redox couple should be carefully considered since $\eta_{interface}$ depends on it to achieve 100% interfacial charge transfer. Consequently, by merging IPCE with the equation for η_{e^-/h^+}, APCE can be manifested as the following equation.

$$APCE(\lambda) = \frac{j_{ph}(mA/cm^2) \times h \cdot c(= 1239.8)(V \times nm)}{P_\lambda(mW/cm^2) \times \lambda(nm) \times \eta_{e^-/h^+}(= 1 - 10^{-A})} \qquad \text{Eq. 1.13}$$

1.3 Transmission Electron Microscope (TEM)

For the last several years, new research fields, which are associated with the nanodevices and/or their materials with unique physical and chemical properties, have discovered and the investigation of the application also for have continued. Various nanodevices, which are utilized nanostructured materials with different morphologies synthesized via diverse methods, are developed. Especially, the one-dimensional (1D) nanoarray such as nanowire, nanorods, and nanotubes array have been focused on the research subjects due to their superior electric properties induced by providing high surface area and rapid electrical pathways.[42-46] Moreover, since larger surface area can be obtained, more complicated three-dimensional (3D) array such as nanotrees, nanoflowers, and dendritic array have also been investigated for applications in sensors, catalysis, optoelectronic devices, photovoltaic devices, and environmental protection.[42, 47-56] The properties of the nanostructured materials are closely related to not only the composition, size, and phase but also to crystallographic characteristics, including crystal structure, orientation and so on.[57-59] In addition to chemical details, in order to understand the relationship between these superior features and structures, structural characteristics should also be closely examined. To this end, transmission electron microscope (TEM), which possesses the high enough spatial resolution, analysis should be carried out for identifying the reason for the structural and morphological issue.

1.3.1 Spatial Resolution of the Transmission Electron Microscope

Since the electrons are accelerated up to a few hundred kV in TEM, the electrons have an extremely high energy. According to the De-Broglie wave theory, the momentum of the accelerated electron, P can be defined as $P = mv = \sqrt{2mE}$ and the relationship between the electrons and its wavelength can be expressed as follows.

$$\lambda = \frac{h}{P} = \frac{h}{\sqrt{2mE}} \qquad \text{Eq. 1.15}$$

where λ is the De Broglie wavelength, h is the Planck's constant, m is the mass of the electron, E is the energy of electron. In addition, because the velocity of the accelerated electron (tens to hundreds of kV) is close to the speed of the light, the quantum mechanical point of view should be considered. For this interested, the wavelength of the accelerated electron can be calculated from following equation.

$$\lambda = \frac{h}{\sqrt{2m_0 E\left(1 + \frac{E}{2m_0 c^2}\right)}} \qquad \text{Eq. 1.16}$$

where m_0 is the electron rest mass and c is the speed of light. With acceleration voltages of a few hundred kV, this yields a wavelength in the pm (10^{-12}m) range. This value is far enough to resolve atoms. Although this resolution is not possible due to imperfect lenses and the interaction of electrons with each other, sub angstrom has been achieved. The relationship between the acceleration voltage and the corresponding wavelength of the electron can be plotted as shown in Figure 1.4 (The constants are summarized in Table 1.1). As stated above, a wavelength for the acceleration voltage over tens of kV is evaluated in the range of tens of pm. Usually the acceleration voltage in the a few–30kV range (shaded in red) is utilized for scanning electron microscope (SEM) and that in over 200kV range is employed for transmission electron microscope (TEM) and/or scanning TEM (STEM).

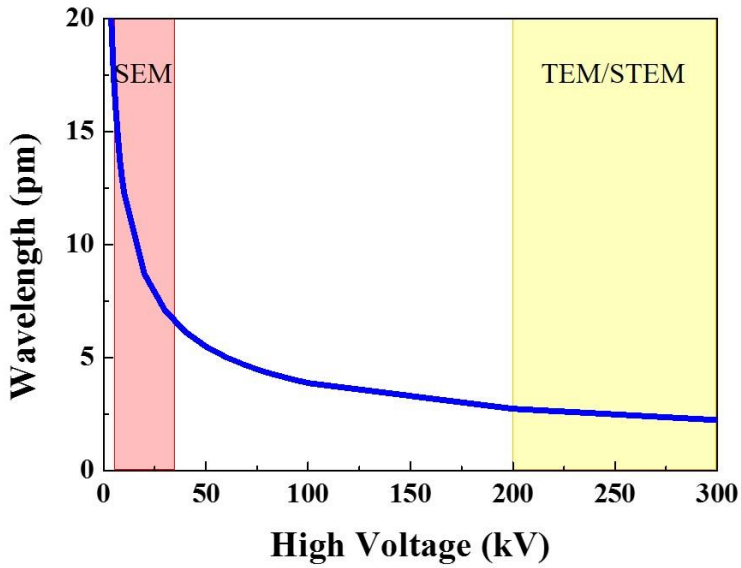

Figure 1.4 The relationship between the acceleration voltage and the corresponding wavelength of the electron.

Table 1.1 The constants for Equation 1.15-16

Charge (e)	-1.602×10^{-19}C
Rest mass (m_0)	9.109×10^{-31}kg
Rest energy (m_0c^2)	511 keV
Planck's constant (h)	6.626×10^{-34}N · m · s
Speed of light in vacuum (c)	2.998×10^{8}m/sec

Even though achieving the high spatial resolution by using the accelerated electrons can be a great advantage, the high energy of the electrons, resulted from the extremely short wavelength, should be considered. Because the thickness of the samples for TEM is below ~100 nm it can be damaged by the high power of the accelerated electrons. Therefore, recently in order to enhance the spatial resolution less than 200 kV region and to reduce the damage on samples, the aberrations from

the electromagnetic lens equipped in a TEM have been corrected and introduced (aberration-corrected TEM).

1.3.2 Interaction between the Electron Beam and Specimen

The specimen for TEM should be less than 100 nm thick to transmit the accelerated electrons through the sample. An image than can be formed from the interaction of the electrons with the sample. The image is magnified and focused onto an imaging device, such as a fluorescent screen, a layer of photographic film, or a sensor such as a charge-coupled device (CCD) camera.

When the accelerated electrons are encountered on to the surface of the sample, the electrons interact with the sample. At this moment, the high kinetic energy of the electrons has been lost and can be transferred and/or released after the interaction in various forms such as x-ray, light, and elastic/inelastic electrons. These diverse forms of interaction products can be utilized as signals of certain detectors and can be reproduced as specific information of the sample.

To adopt usefulness of electron microscopy, the interactions between the electrons and a TEM specimen should be understood. The diverse interaction products can carry chemical, crystallographic, or topographic information. These signals include

- Transmitted electrons – transmitted through a specimen to form an image (TEM and HRTEM)
- Secondary electrons – absorbed energy from a primary electron and have been released from the nucleus (SEM)
- Backscattered electrons – scattered in opposite the direction of the incident electron beam (Electron Back-Scattered-Diffraction: EBSD)
- X-rays – a result of electrons falling to empty orbitals (Energy Dispersive Spectroscopy: EDS)
- Inelastically scattered electrons – lost energy in the sample and have been transmitted through the sample (Electron Energy Loss Spectroscopy: EELS)

- Light – electron induced light (Cathodoluminescence: CL)

The HRTEM and SAED are considerably useful for interpretations of crystallographic and morphological characteristics. Due to the advantages on the high resolution and imaging immediately, precise analysis can be possible. Particularly, the Fast Fourier Transformation (FFT) based on the HRTEM images is one of the useful tools for the atomic scale structure analysis. In addition, by controlling the incident and/or diffraction condition of the electron beam, 2D- and/or 3D-structural information can be constructed. The signals from the interaction between the accelerated electron and the samples are described as shown in Figure 1.5.

Hence, the TEM analysis for nanostructured materials synthesized is essential because it can provide not only the morphological, chemical features but also the crystallographic information in detail.

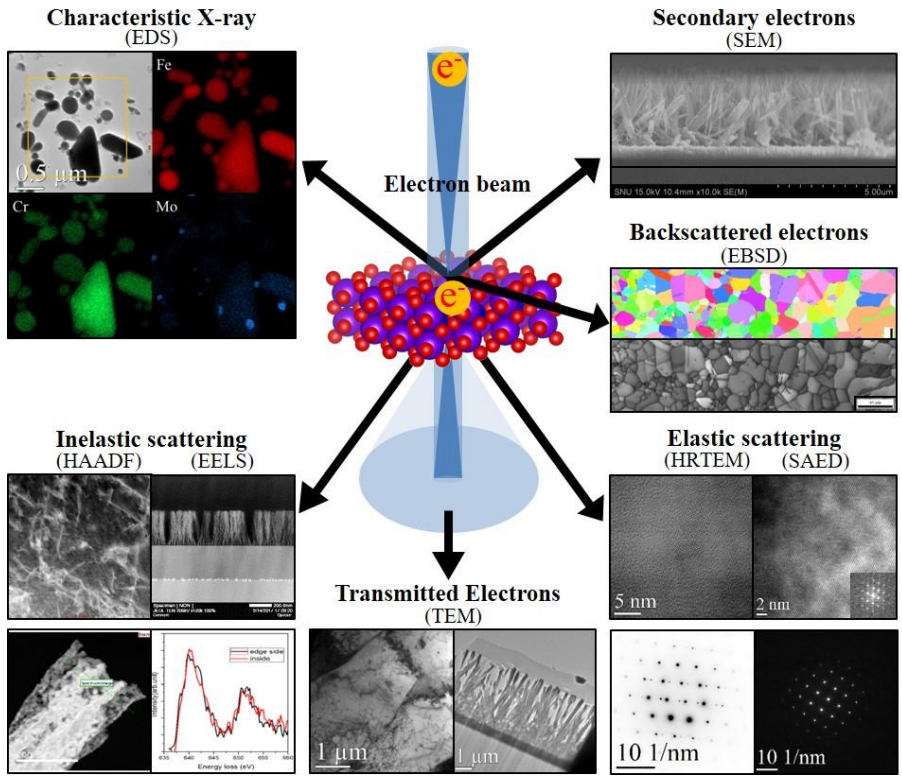

Figure 1.5 The signals from the interaction between the accelerated electrons and TEM samples

1.4 Scope and Organization

This thesis has focused on the growth of the TiO_2 nanorods during the hydrothermal process, and the microstructural analysis of the heterostructure TiO_2 and transition metal dichalcogenide (TMD) for the direct solar water splitting applications. The growth of the TiO_2 nanorods by the hydrothermal method has intensively investigated. In addition, the effects of the various parameters for controlling the morphology of the hydrothermally grown TiO_2 nanorods were examined. Furthermore, the photoelectrochemical (PEC) performances of the MoS_2/TiO_2 heterostructure were measured for the solar water splitting applications. Finally, the microstructure analyses of the MoS_2/TiO_2 heterostructure carried out.

Chapter 1 includes the overall introductions and theoretical backgrounds are overviewed as stated above.

Chapter 2 deals with the growth mechanism of the TiO_2 nanorods synthesized by the hydrothermal method and reveals the effects of the various parameters on the growth of the rutile phase TiO_2 nanorods.

Chapter 3 consists of the PEC performances of the 2D-MoS_2/TiO_2 nanorods heterostructure and its microstructural analyses. Especially, the evolution of the performance of the 2D-TMD MoS_2 on the TiO_2 nanorods synthesized by hydrothermal method has measured and the main factor for the enhancement in PEC performance were investigated in the microstructural point of view.

Finally, the entire context of this thesis was summarized in conclusion.

1.5 References

1. N. S. Lewis, A. N. Laboratory and U. S. D. o. E. O. o. Science, *Basic Research Needs for Solar Energy Utilization: Report on the Basic Energy Sciences Workshop on Solar Energy Utilization*, Argonne National Laboratory, 2005.
2. M. Gratzel, *Nature*, 2001, **414**, 338-344.
3. A. Fujishima and K. Honda, *Nature*, 1972, **238**, 37.
4. T. Abbasi and S. A. Abbasi, *Renew Sust Energ Rev*, 2011, **15**, 3034-3040.
5. M. Balat, *International Journal of Hydrogen Energy*, 2008, **33**, 4013-4029.
6. J. Nowotny, C. C. Sorrell, L. R. Sheppard and T. Bak, *International Journal of Hydrogen Energy*, 2005, **30**, 521-544.
7. M. G. Walter, E. L. Warren, J. R. McKone, S. W. Boettcher, Q. Mi, E. A. Santori and N. S. Lewis, *Chem Rev*, 2010, **110**, 6446-6473.
8. F. Yilmaz, M. T. Balta and R. Selbas, *Renew Sust Energ Rev*, 2016, **56**, 171-178.
9. J. Turner, G. Sverdrup, M. K. Mann, P.-C. Maness, B. Kroposki, M. Ghirardi, R. J. Evans and D. Blake, *International Journal of Energy Research*, 2008, **32**, 379-407.
10. J. A. Turner, *Science*, 1999, **285**, 687-689.
11. N. S. Lewis, *Science*, 2007, **315**, 798-801.
12. W. Septina and S. D. Tilley, *Current Opinion in Electrochemistry*, 2017, **2**, 120-127.
13. J. D. Holladay, J. Hu, D. L. King and Y. Wang, *Catalysis Today*, 2009, **139**, 244-260.
14. A. J. Bard and M. A. Fox, *Accounts of Chemical Research*, 1995, **28**, 141-145.
15. S. Y. Reece, J. A. Hamel, K. Sung, T. D. Jarvi, A. J. Esswein, J. J. H. Pijpers and D. G. Nocera, *Science*, 2011, **334**, 645-648.

16. J. W. Jang, C. Du, Y. Ye, Y. Lin, X. Yao, J. Thorne, E. Liu, G. McMahon, J. Zhu, A. Javey, J. Guo and D. Wang, *Nat Commun*, 2015, **6**, 7447.
17. K. Sivula, F. Le Formal and M. Gratzel, *ChemSusChem*, 2011, **4**, 432-449.
18. A. Guerrero and J. Bisquert, *Current Opinion in Electrochemistry*, 2017, **2**, 144-147.
19. M. Szklarczyk and J. O. Bockris, *J Phys Chem-Us*, 1984.
20. O. Khaselev and J. A. Turner, *Science*, 1998, **280**, 425-427.
21. S. Giménez and J. Bisquert, *Photoelectrochemical Solar Fuel Production: From Basic Principles to Advanced Devices*, Springer International Publishing, 2016.
22. S. Y. Chen and L. W. Wang, *Chemistry of Materials*, 2012, **24**, 3659-3666.
23. S. A. Bonke, M. Wiechen, D. R. MacFarlane and L. Spiccia, *Energy & Environmental Science*, 2015, **8**, 2791-2796.
24. B. A. Pinaud, J. D. Benck, L. C. Seitz, A. J. Forman, Z. B. Chen, T. G. Deutsch, B. D. James, K. N. Baum, G. N. Baum, S. Ardo, H. L. Wang, E. Miller and T. F. Jaramillo, *Energy & Environmental Science*, 2013, **6**, 1983-2002.
25. M. Dumortier, S. Tembhurne and S. Haussener, *Energy & Environmental Science*, 2015, **8**, 3614-3628.
26. J. W. Ager, M. R. Shaner, K. A. Walczak, I. D. Sharp and S. Ardo, *Energy & Environmental Science*, 2015, **8**, 2811-2824.
27. J. R. Bolton, S. J. Strinkler and J. S. Connolly, *Nature*, 1985, **316**.
28. S. Hu, C. X. Xiang, S. Haussener, A. D. Berger and N. S. Lewis, *Energy & Environmental Science*, 2013, **6**, 2984-2993.
29. R. E. Rocheleau and E. L. Miller, *International Journal of Hydrogen Energy*, 1997, **22**, 771-782.
30. L. C. Seitz, Z. Chen, A. J. Forman, B. A. Pinaud, J. D. Benck and T. F. Jaramillo, *ChemSusChem*, 2014, **7**, 1372-1385.

31. Z. Chen, H. N. Dinh and E. Miller, *Photoelectrochemical Water Splitting: Standards, Experimental Methods, and Protocols*, Springer New York, 2013.
32. N. Chouhan, R. S. Liu and J. Zhang, *Photochemical Water Splitting: Materials and Applications*, CRC Press, 2017.
33. T. Bak, J. Nowotny, M. Rekas and C. C. Sorrell, *International Journal of Hydrogen Energy*, 2002, **27**, 991-1022.
34. H. Mullejans, A. Ioannides, R. Kenny, W. Zaaiman, H. A. Ossenbrink and E. D. Dunlop, *Measurement Science and Technology*, 2005, **16**, 1250-1254.
35. G. P. Smestad, F. C. Krebs, C. M. Lampert, C. G. Granqvist, K. L. Chopra, X. Mathew and H. Takakura, *Solar Energy Materials and Solar Cells*, 2008, **92**, 371-373.
36. A. B. Murphy, P. R. F. Barnes, L. K. Randeniya, I. C. Plumb, I. E. Grey, M. D. Horne and J. A. Glasscock, *International Journal of Hydrogen Energy*, 2006, **31**, 1999-2017.
37. N. S. Lewis, *Accounts of Chemical Research*, 1990, **23**, 176-183.
38. J. H. Werner, S. Kolodinski and H. J. Queisser, *Phys Rev Lett*, 1994, **72**, 3851-3854.
39. E. L. Miller, D. Paluselli, B. Marsen and R. E. Rocheleau, *Solar Energy Materials and Solar Cells*, 2005, **88**, 131-144.
40. M. F. Weber, *Journal of The Electrochemical Society*, 1984, **131**, 1258.
41. R. C. Kainthla, S. U. M. Khan and J. O. Bockris, *International Journal of Hydrogen Energy*, 1984, **12**.
42. Y. W. Jun, Y. Y. Jung and J. Cheon, *J Am Chem Soc*, 2002, **124**, 615-619.
43. I. Gonzalez-Valls and M. Lira-Cantu, *Energy & Environmental Science*, 2009, **2**, 19-34.
44. A. I. Hochbaum and P. Yang, *Chem Rev*, 2010, **110**, 527-546.
45. S. C. Pang, M. A. Anderson and T. W. Chapman, *Journal of the Electrochemical Society*, 2000, **147**, 444-450.

46. S. L. Chou, J. Z. Wang, S. Y. Chew, H. K. Liu and S. X. Dou, *Electrochemistry Communications*, 2008, **10**, 1724-1727.

47. H. Wang, X. H. Zhang, X. Fan, C. S. Lee and S. T. Lee, *Chem Commun (Camb)*, 2009, DOI: 10.1039/b910360k, 5916-5918.

48. T. L. Sounart, J. Liu, J. A. Voigt, J. W. P. Hsu, E. D. Spoerke, Z. Tian and Y. B. Jiang, *Advanced Functional Materials*, 2006, **16**, 335-344.

49. Y. Zhao, Y. Xie, J. S. Jie, C. Y. Wu and S. Yan, *Journal of Materials Chemistry*, 2009, **19**, 3378-3383.

50. Z. Q. Liu, L. X. Ding, Z. L. Wang, Y. C. Mao, S. L. Xie, Y. M. Zhang, G. R. Li and Y. X. Tong, *Crystengcomm*, 2012, **14**, 2289-2295.

51. L. Wang and Y. Yamauchi, *Chemistry of Materials*, 2009, **21**, 3562-3569.

52. G. Xu, W. B. He, Y. G. Zhao, Y. Liu, Z. H. Ren, G. Shen and G. R. Han, *Crystengcomm*, 2011, **13**, 1498-1503.

53. M. L. Yang, *Journal of Materials Chemistry*, 2011, **21**, 3119-3124.

54. M. J. Bierman, Y. K. A. Lau and S. Jin, *Nano Letters*, 2007, **7**, 2907-2912.

55. D. Wang, F. Qian, C. Yang, Z. H. Zhong and C. M. Lieber, *Nano Letters*, 2004, **4**, 871-874.

56. D. Moore, Y. Ding and Z. L. Wang, *Angew Chem Int Ed Engl*, 2006, **45**, 5150-5154.

57. T. Zhang, W. Dong, M. Keeter-Brewer, S. Konar, R. N. Njabon and Z. R. Tian, *J Am Chem Soc*, 2006, **128**, 10960-10968.

58. J. Zhang, Q. Xu, Z. Feng, M. Li and C. Li, *Angew Chem Int Ed Engl*, 2008, **47**, 1766-1769.

59. T. L. Sounart, J. Liu, J. A. Voigt, M. Huo, E. D. Spoerke and B. McKenzie, *J Am Chem Soc*, 2007, **129**, 15786-15793.

Chapter 2

Synthesis of TiO_2 Nanostructures by Hydrothermal Methods

2.1 Introduction

Since the first repot by Fujishima and Honda[1] about the photocatalytic water splitting of TiO_2 electrode under UV light and an impressive report by Grätzel[2] about the TiO_2 based dye-sensitized solar cell (DSSC), diverse researches have been carried out.[3-12] TiO_2 nanostructured materials have been investigated and utilized due to their superior features such as electrical, optical, catalytic properties, and high chemical stability, low recombination rate.[5, 13, 14] In order to take the beneficial characteristics, several applications including sensors, solar cells and catalysts have been reported.[1, 2, 10, 15-21] Above all, the hydrogen generation by water photoelectrolysis, and photocatalysis is the most active research field for those properties[1, 2, 17, 19, 22-25] because it can be a good solution for the global issue of energy and environmental problems. Hence, in order to achieve the well-crystallized TiO_2 nanostructured materials for those kinds of applications various synthesizing methods such as the template assisted method,[26] electrochemical methods,[27] chemical vapour deposition (CVD),[28] and sol–gel process,[29] solvothermal method,[30-41] and hydrothermal method,[42] have been investigated. Most remarkably, the hydrothermal method is the most fascinating route for the synthesis the TiO_2 materials since the reaction times is short, the cost of process is low, and especially, it is the facile method to vary the morphologies of TiO_2 nanostructured materials.[14, 43, 44] In other words, in a hydrothermal process, by not only varying the synthesizing time and/or temperature, but also by controlling the concentration and/or pH of solvents, the concentration of precursors, and catalysts, the crystalline TiO_2 nanostructure with diverse morphologies can be easily produced. Due to this diversity, optimum condition for desired nanostructured has been required.

The properties of the nanostructured TiO_2 are strongly dependent on the structures, size and/or morphologies of the crystal.[45-55] The formation of TiO_2 nanorods is affected by the surface energy and chemistry of the precursor.[56-59] In the crystallographic point of view, TiO_2 has three different phases; rutile, anatase, and

brookite. The rutile and anatase are the tetragonal structure and the brookite is the orthorhombic structure. Furthermore, in a thermodynamic point of view, the rutile phase is most stable at room temperature, while anatase is kinetically preferred, which indicates the formation of the anatase occurs first.[14] In addition, the rutile phase TiO_2 has higher refractive index.[60] The atomic structures[61] and lattice parameters are summarized in Figure 2.1 and Table 2.1.

The new physical and chemical properties appear if the size of the particles becomes smaller and smaller near or below nm scale. Moreover, those unique features can be changed and/or obtained by varying not only the size but also morphology of the particle.[20] Based on these approaches, several specific morphologies of the TiO_2 particles have been developed such as nanowires, spheres, nanotubes, nanocorals, nanorods, nanoribbons, nanotubes, nanosheets and hollow spheres.[44, 62-69] Especially, one-dimensional (1D) morphology along the specific orientation can be achieved by using the advantages of growth rate difference among the crystallographic facets.[70] It has been reported that Introducing a photoelectrode with 1D crystalline nanostructure arrays can highly enhance the performance of the photoelectrochemical (PEC) cells because it provides the high specific surface area, leading to drastic increase in a surface-to-volume ratio, the channel for transportation from the interface to the electrodes, and the effect of facilitating ion diffusion,[71-75] resulting in a dramatic enhancement of 1D arrays devices.

As one of the most potential photocatalysts, TiO_2 can play an important role to solve the severe environmental problems in the applications for the direct solar water splitting device.

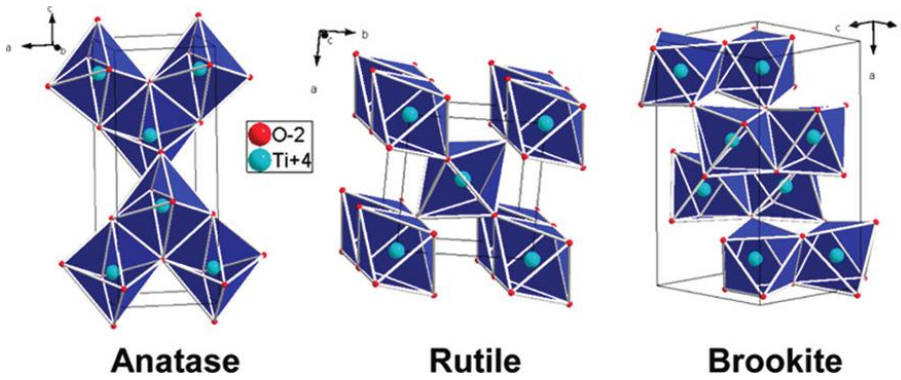

Figure 2.1 Three polymorphs of the TiO_2: anatase, rutile, and brookite

Table 2.1 The crystal structures and the lattice parameters of the polymorphs of TiO_2

Phase	anatase	rutile	brookite
Crystal structure	Tetragonal	Tetragonal	Orthorhombic
Lattice Parameters	a = b = 3.7845 Å c = 9.5143 Å α = β = γ = 90°	a = b = 4.652 Å c = 2.970 Å α = β = γ = 90°	a = 5.4558 Å, b = 9.1819 Å, c = 5.1429 Å α = β = γ = 90°

2.2 Experimental Procedures

TiO_2 nanorods Synthesis on FTO substrates

Fluorine doped Tin Oxide (F: SnO_2, FTO, 1.5 cm × 2 cm × 0.2 cm) substrates, which is widely used as a transparent conducting substrates, were cleaned in sequence with acetone, isopropanol, and deionized (DI) water for 10 minutes in a ultrasonificator, respectively. Then the surface of the substrates was dried with an Argon blow gun. After the cleaning of the FTO substrates, TiO_2 nanorods were grown on the substrate by the typical hydrothermal method. In detail, 0.5–2 ml (8.6–34.1 mM) of Titanium(IV) tetra isopropoxide (TTIP) as a Titanium precursor was dissolved at room temperature under vigorous magnetic stirring in the mixture of 200 ml of hydrochloric acid (HCl) and DI water solution. The volume of the HCl was varied from 90 to 120 ml (5.5–7.3 M HCl). The stirring was maintained until the cloudy solution became clear. The experiments were performed under various temperature, time, precursor concentration, and HCl concentrations to establish the optimum synthesizing conditions for the TiO_2 nanorods while the total volume of the mixture solution was remained in 200 ml. 50 ml of the mixture solution was transferred into the 100 ml–volume–Teflon vessel where the substrates were placed at the bottom. The active faces of the FTO substrates were facing up during the whole synthesis process. The Teflon vessel with the precursor solution and the substrate was put into a stainless steel autoclave and was sealed tightly. The growth of the TiO_2 nanorods was carried out for 1.5–5 hours at 180–200 ℃ in a box furnace. After the growth, the autoclaves were cooled down to the room temperature naturally. The substrates with TiO_2 nanorods on active surfaces were rinsed smoothly with DI water several times and dried with Argon blow. The dried substrates were annealed in a box furnace with air atmosphere at 350 ℃ for an hour (the heating rate is 5℃·min^{-1}).

TiO_2 nanorods Synthesis on TiO_2 single crystal with various orientations

The identical hydrothermal sequence for the TiO_2 nanorods on a FTO substrate was conducted for the growth on TiO_2. The single crystal TiO_2 substrates with the orientations of (001), (101), and (110) were introduced. In order to investigate the growth behaviors, the surface morphologies on the polished and unpolished surface were examined.

TiO_2 nanorods Synthesis on *p*-Si

A single-side-polished *p*-Si (100) wafer was cut into 2 cm × 2 cm and cleaned carefully with same method as FTO substrates. A piece of cleaned wafer was soaked in 2% hydrofluoric acid (HF) for 1 minute to remove the SiO_2 native oxide layer and organic residues on the polished surface. Right after the HF etching, etched surfaces were rinsed with DI water for 1 minute. 5–20 nm–thick TiO_2 film was deposited as a passivation layer and a seed layer using an electron-beam evaporator (KVE-E2004L), of which deposition rate was controlled for 0.2 $Å \cdot sec^{-1}$. TiO_2 film deposited *p*-Si substrates were annealed at 500 ℃ in a tube furnace with N_2 atmosphere. After the annealing, TiO_2 nanorods were synthesized by the hydrothermal method. Briefly, 2 ml (34.1–67.6 mM) of TTIP was dissolved at room temperature under vigorous magnetic stirring in the mixture of 5.5–7.3 M HCl aqueous solution. The stirring was continued until the mixture solution became transparent. After the TiO_2 film deposited *p*-Si substrate was placed at the bottom of the Teflon vessel, of which the film side was facing up, 50 ml of the mixture solution was filled into the vessel. The Teflon vessel was put into a stainless steel autoclave. Tightly sealed autoclave was placed in the box furnace. Then, the growth of the TiO_2 nanorods was conducted for 1.5–5 hours at 200 ℃. After the growth process, the autoclaves were naturally cooled down to the room temperature. The substrates were taken out from the vessel and were washed carefully with DI water several times and were dried. The dried substrates were annealed in a tube furnace with N_2 atmosphere at 500 ℃ for 30 minutes. In particular, the tube was purged with N_2 for 2 hours before the annealing was started and the heating rate is 5 $℃ \cdot min^{-1}$

Microstructural Analysis

Field Emission-Scanning Electron Microscope (FE-SEM).

The surface morphology of substrates was analyzed by using field-emission scanning electron microscopy (FE-SEM, Hitachi, SU-70; Carl Zeiss, Supra) at the accelerating voltage of 2–15 kV, the working distance of ~5–10mm. In order to avoid the electron charge effects and to achieve a high resolution image, conducting path were connected from the sample to the SEM sample holder. Briefly, the one edge of the FTO substrate was smoothly scratched with a knife. Then, Ag paste were covered and dried in the air. On the other hand, in p-Si substrate case, the back side of the substrate was ground ~50 μm to remove the native SiO_2 layer and was immediately covered with the Ag paste over it. Finally, the samples were dried in the air.

Transmission Electron Microscope (TEM).

The transmission electron microscope (TEM, JEOL, JEM-2100F) analysis were carried out at an accelerating voltage of 200 kV, which was equipped with high-angle annular dark-field image (HADDF), scanning TEM (STEM), and energy dispersive spectroscopy (EDS). The samples for TEM analysis were prepared in three different methods as needed; drop casting, ion-milling, and focused ion beam (FIB). First, TiO_2 nanorods synthesized were scratched off from the substrate and the powders scratched were dispersed in ethanol. The dispersion solutions were sonicated for 10 minutes. A drop of the solution was dropped onto a carbon coated copper mesh TEM grid and dried with an infrared lamp. Second, the TiO_2-grown-sides of the samples were attached facing each other with M-bond 610, which is chemically and mechanically stable in high vacuum. The samples were cut into less than 3 mm long and were polished on lapping films (the grit sizes of the films are 15–0.5 μm) in the thickness direction until the thickness was about 1 μm. After the polishing, the sample was bonded with M-bond 610 on a copper grid with an oval

hole. Then, the grid was transferred into the precision ion polishing system (PIPS, Gatan, model 691) and Ar ion beam thinning was carried out at 5kV with an incident angle of 6–15°. Third, the sample was placed inside a dual beam focused ion beam (FIB, Seiko, SMI3050SE). Before using the Ga^+ ion beam to prepare the samples for TEM, it was necessary to protect the surface of the sample from accelerating focused Ga^+ ions. Furthermore, these protecting layer can enhance the uniformity in terms of the milling rate of the samples. This was achieved by depositing platinum and/or carbon film with a thickness of ~ 2 μm onto the surface. This process was conducted using an accelerating voltage of 15 kV and a beam current of maximum 20 nA. After the thinning, the cross-sectioned surfaces were then smoothly polished at 5kV to remove the Ga^+ embedded damage layer during the thinning process. In order to achieve a damage-minimized-surface, Nano-mill (Fischione, M1040) cleaning was followed. The high-resolution TEM (HR-TEM) images were acquired at 200kV. The structural analysis was conducted by analyzing the Fast Fourier Transform (FFT) patterns and by measuring interplanar spacing of particular planes. In addition, scanning TEM (STEM) high-angle annular dark field (HAADF) images and Z-contrast images which are sensitive to variations in the atomic number of atoms were obtained. In order to confirm the elemental distributions of the samples synthesized, elemental mappings were carried out by using energy-dispersive X-ray spectroscopy (EDS).

2.3 Results and Discussions

The hydrothermal method is one of the facile and simple processes compared to other synthesis methods because any vacuum process is necessary and the growth temperature is relatively low. TiO_2 nanostructures can be synthesized by the simple process, as shown in Figure 2.2. First of all, the solution, which is consist of a precursor as a Ti source is filled into a Teflon beaker, where the sample is placed. The solution containing Teflon beaker is transferred into a stainless steel autoclave. After that, the autoclave tightly sealed is kept in an oven or furnace with a specific temperature and time. The morphology of the products can be controlled by the synthesizing conditions, which can be classified into three factors. The various parameters related to the hydrothermal synthesis were summarized as shown in Table 2.2. At first, in the perspective of the solution, the precursor concentration of the solution can control the number of nucleation sites as a Ti source. In addition, the concentration of the HCl, which is one of the most crucial parameters has roles to determine the phase among the TiO_2 polymorphs and the kinetics in the growth and to enable a preferential growth. These factors will be discussed. Second, since the synthesis temperature and time facilitates the kinetics of the reactions, it shows linear relation with the growth of TiO_2. Finally, the morphology of TiO_2 nanorods can be controlled by the surface conditions and/or the multiple synthesis.

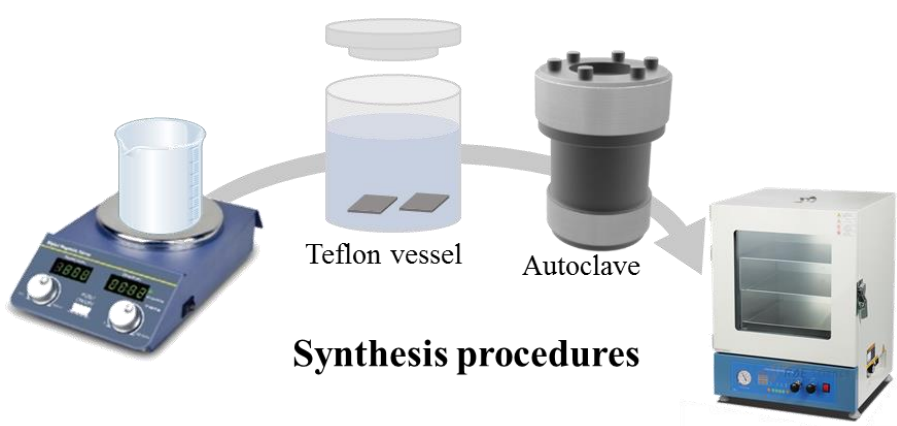

Figure 2.2 The synthesis procedures for hydrothermal method

Table 2.2 Several parameters related to the hydrothermal synthesis, which are closely connected each other

Reaction	Temperature/Time	• Nucleation kinetics • Growth (length, diameter)
Solution	Precursor concentrations	• Number of nucleation • Amount of Ti source
	pH	• Phases (Rutile, Anatase, Brookite) • Preferential growth • Growth kinetics
	Volume	• Partial pressure (water, HCl)
Etc.	Substrates	• Nucleation sites (seed layer) • Lattice mismatch
	The number of times	• 2^{nd} and/or 3^{rd} nucleation

2.3.1 Preferential Growth of TiO_2 Nanorods

The synthesis of TiO_2 nanorods by hydrothermal method is the facile way to obtain the desired morphology. The synthesizing TiO_2 nanorods on a substrate, unlike the powder synthesis, the specific parameter such as a preferential growth should be considered because the one-dimensional (1D) growth should be intentionally generated. Figure 2.3 (a) and (b) shows the typical SEM images of TiO_2 nanorods by hydrothermal method. As shown in Figure 2.3 (c), the rutile phase TiO_2 nanorod has four identical {110} planes as side faces and grows preferentially along the [001] direction. It has been reported that the (110) plane is the most stable plane, followed by (100), (101), and finally (001) plane, which exhibits the highest surface energy.[76-80] Thus, the formation of the rod shape is originated from the surface energy difference in the thermodynamical point of view. Other critical factors for the preferential growth of the TiO_2 nanorods is the concentration of HCl. Generally, the HCl concentration has been regarded as an indicator to determine the phase of the TiO_2 and/or morphology. The rutile phase is stable that other polymorphs in a low pH solution whereas the anatase phase is stable in a high pH solution.[76-78, 80]

There are three polymorphs of TiO_2 in nature[61] as shown in Figure 2.1. Rutile is tetragonal ($P4_2/mnm$) structure and anatase is also tetragonal ($I4_1/amd$) structure.

However, even though those two polymorphs possess the same crystal structure, difference between the two polymorphs is originated from the fact that how the octahedra are connected. In rutile, [TiO_6] octahedrons as shown in Figure 2.4 (a), which can be regarded as a building unit, linked with each other by sharing two edges along the c axis to construct chains (edge-shared connection), and then the chains were connected with corner-shared bonding. However, the anatase TiO_2 was constructed by sharing four edges of the [TiO_6] octahedron (face-shared connection) [81-84] as shown in Figure 2.4 (b). Highly acidic solutions appear to be preferable for synthesizing rutile and basic solutions for the anatase phase as mentioned above.[82-85] Furthermore, the growth is suppressed in a low pH solution. Figure 2.5 shows the stable morphology of the rutile and anatase TiO_2 under diverse conditions of the solution.[80] Therefore, the growth process is highly influenced by the concentration of the HCl as a crucial parameter for defining the stable phase and morphology of TiO_2. Figure 2.6 describes the reaction process during the hydrothermal synthesis of TiO_2.[86] In chemistry, protonation means the addition of a proton (H^+) to an atom, molecule, or ion. On the other hand, deprotonation is the removal of a proton in an acid-base reaction. Olation is the process by which metal ions form polymeric oxides in aqueous solution. A condensation reaction in which an oxo bridge is formed between two metal centers, which indicated that the formation of the oxo-dimer.[86, 87] The chemical reaction during the hydrothermal synthesis of TiO_2 can be expressed as follow.

$$Ti^{4+} + 2H_2O \rightarrow TiOH^{2+} + 2H^+ \qquad \text{Eq) 2.1}$$

$$TiOH^{2+} + O_2 \rightarrow Ti(IV)\text{oxo species} + O^{2-} \rightarrow TiO_2 \qquad \text{Eq) 2.2}$$

In these reaction, the Ti^{4+} precursor hydrolyzes continuously into $TiOH^{2+}$, and the required OH^- ions are formed by decomposition from water molecules from the Ti

precursor aqueous solution. $TiOH^{2+}$ would be slowly oxidized to the Ti(IV) oxo species as a building unit by consuming dissolved oxygen from the inside of a Teflon beaker. The Ti(IV) oxo species is considered as an intermediate between TiO^{2+} and TiO_2, which is finally dehydrated into TiO_2.[86, 87]

Hence, there are specific roles of acid. First, it suppresses the hydrolysis of Ti precursors under acidic conditions. Second, it also acts as a linear chain support for the adsorption of Cl^- ions from the acid. The Cl^- ions, supplied by the solution, can be selectively adsorbed onto the {110} planes of rutile TiO_2 and prohibits further growth of the planes, accelerating the anisotropic growth in the [001] direction. Therefore, the growth of 1D rutile TiO_2 nanorods can be achieved by selectively attaching Cl^- ions on {110} planes and by the surface energy difference among lattice planes of the rutile phase.

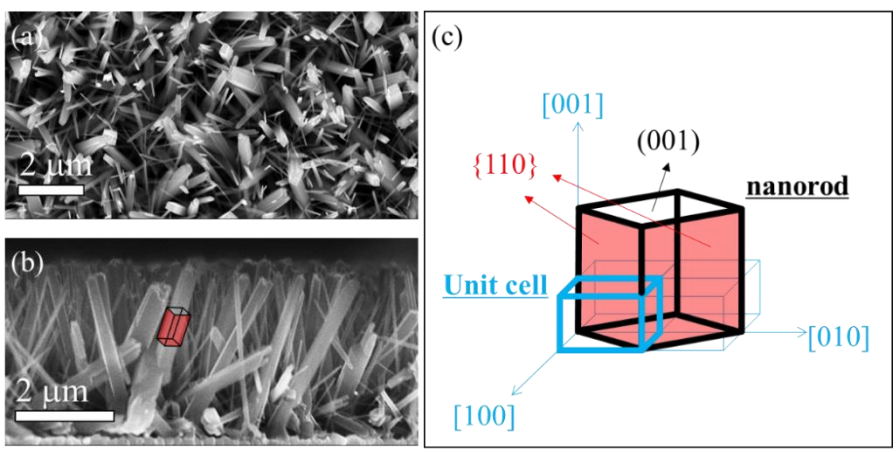

Figure 2.3 Typical morphology of the TiO_2 nanorods on a FTO substrate by a hydrothermal method (a) top view, (b) cross-sectional view, and (c) the crystallographic orientation of TiO_2 nanorod; the hexahedron shaded in red in (b) corresponds to that in (c)

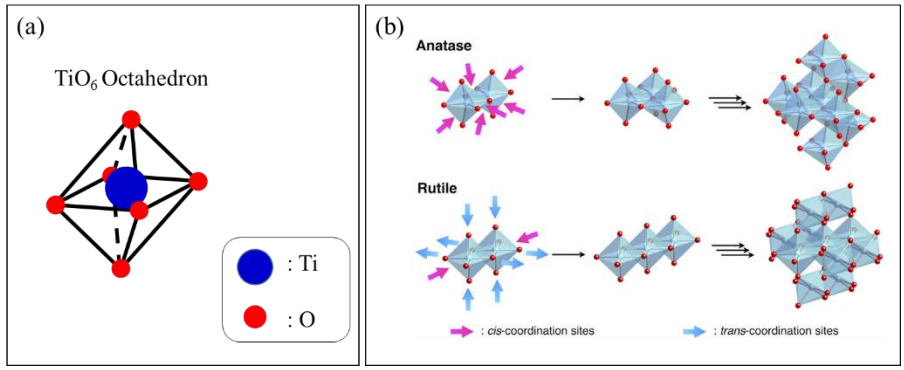

Figure 2.4 TiO_6 octahedron, one Ti atom is connected with six O atoms (b) The formation of the anatase and rutile phases of TiO_2; face-shared connections form an anatase phase while edge-shared connections generate a rutile phase.[81]

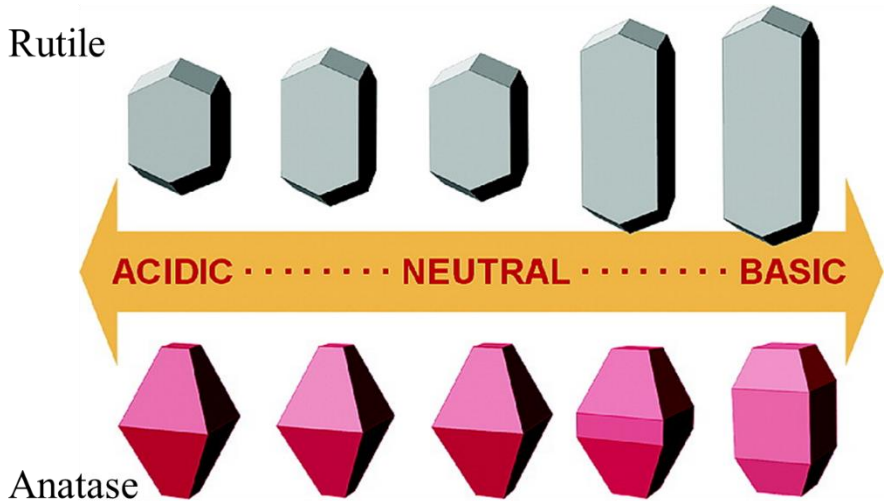

Figure 2.5 Morphology predicted for rutile (top) and anatase (bottom) phased in various pH conditions[80]

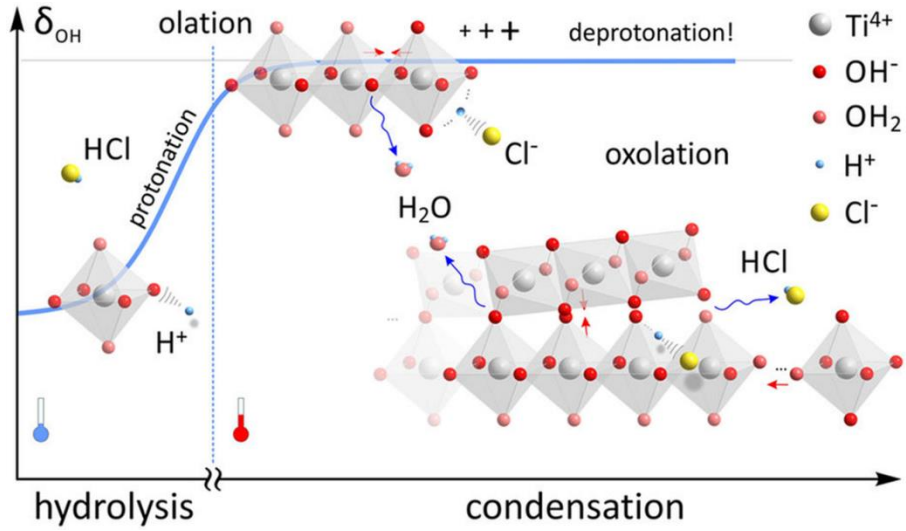

Figure 2.6 Schematic of Hydrolysis and condensation processes during the hydrothermal method[86]

2.3.2 Growth of the TiO2 Nanorods on a FTO Substrates

The FTO substrate as one of the transparent conducting substrates is widely used for synthesizing TiO_2 nanorods. Especially, the lattice mismatch between SnO_2 and TiO_2 is negligible so that it can have a role as a seed for TiO_2 nanorods. Thus, TiO_2 can nucleate on FTO with just same crystallographic orientation of SnO_2 and grow in the form of rods. Figure 2.7 (a)–(b) shows the morphology of the bare FTO substrate. It can be easily noticed that the surface of the FTO has crystals with facets of tens to hundreds of nanometer scale and the roughness of the surface is also same scale. The TiO_2 nanorods grown on FTO have similar diameter of the SnO_2 and the length of them is ~2 μm (Figure 2.7 (c)– (d)). Interesting thing is that ~ 500 nm-thick film was formed at the bottom of the nanorods (near the interface between the FTO and TiO_2) and as closer to the top surface uniformly aligned nanorods were formed along a similar direction nanorods with relatively low density compare to the bottom of the rods. It can be elucidated that TiO_2 nanorods grown preferentially along each [001] direction from the randomly distributed SnO_2 crystals were blocked by adjacent rods

and the blocked rods can grow only laterally. Thus, only unblocked rods can continuously grow, resulting in uniformly aligned nanorods.

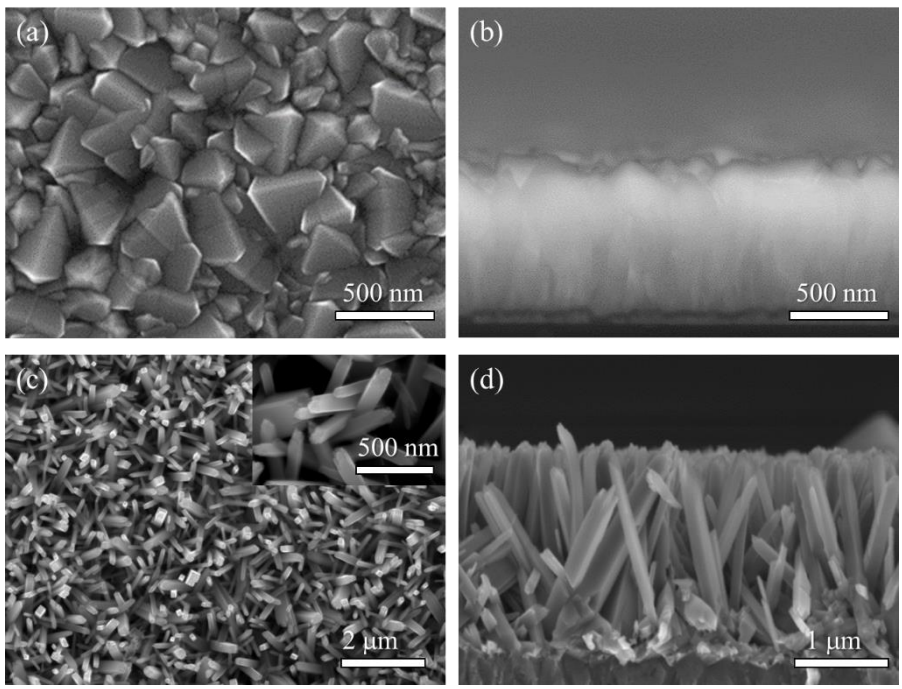

Figure 2.7 SEM images of the (a) plane view of a bare FTO glass (b) cross-sectional view of the FTO glass, typical morphology of the TiO_2 nanorods on a FTO substrates by hydrothermal method (c) plane view and (d) cross-sectional view

2.3.3 Growth Temperature

Figure 2.8 (a)–(f) shows the SEM images of hydrothermally grown TiO_2 nanorods on FTO substrates with various synthesizing temperature. The 50 ml of solutions for the synthesis were composed of 44.9 mM Titanium(IV) tetra isopropoxide (TTIP) and 6.1 M HCl. The hydrothermal synthesis was conducted at 150–180 ℃ for 3 hours. In order to compare quantitatively, the measured diameters and lengths of nanorods were plotted as shown in Figure 2.8 (g). The growth of nanorods showed a linear relationship with increasing temperature. In other words, as the synthesizing

temperature is increased from 150 to 180 ℃, the size of the nanorods is also increased from ~200 nm to ~500 nm in laterally and from tens of nm to ~ 5 μm in vertically, respectively. As shown in Figure 2.8 (d) and (f), the nanorods are attached each other like a film, the film like morphology cab be removed by tuning the concentration of HCl, which will be discussed next sections.

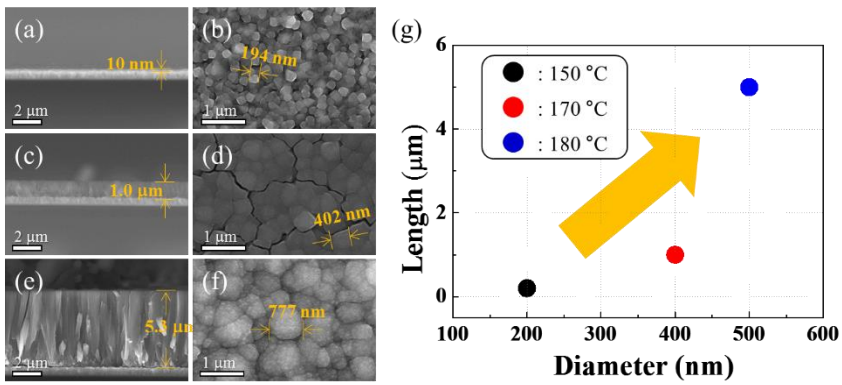

Figure 2.8 Cross-sectional and plane SEM images of the TiO_2 nanorods hydrothermally grown on FTO glasses under the various synthesizing temperatures, where other synthesis conditions were fixed. (a)–(b) 150 ℃, (c)–(d) 170 ℃, and (e)–(f) 180 ℃, (g) evolutions of the size of the TiO_2 nanorods

2.3.4 Growth Time and Precursor Concentration

Figure 2.9 shows the SEM images of the morphologies of hydrothermally grown TiO_2 nanorods with various synthesizing times and precursor concentrations, respectively. In order to finely tune the morphology of the nanorods, *p*-Si and Titanium(IV) isopropoxide (TTIP) were introduced as the substrate and Ti precursor, respectively. The 50 ml of solutions for synthesis were prepared with 34 mM TTIP and 7 M HCl. Furthermore, the synthesizing temperature is fixed at 200 ℃ (20 ℃ higher than the previous section) to confirm the effects of the synthesizing time and precursor concentration. The growth of the nanorods were accelerated not only under increase in time (Figure 2.9 (a)–(c)) but also the precursor concentration (Figure 2.9

(d)–(f)) under fixed temperature. It should be noted that the nanorods grew from the certain regions (regarded as seeds) and formed flower shapes, and began to grow preferentially, and after that the nanorods covered entire area of the substrate under sufficient synthesizing time. This feature indicates that uniformly grown nanorods can be synthesized when nucleation sites are sufficiently formed on a substrate. In order to increase the nucleation sites, the growth behaviors with the precursor concentrations were examined. Other synthesis conditions were fixed except the precursor concentrations from 50.9 to 84.1 mM TTIP and synthesizing time of 1.5 hours to confirm the initial state of the growth. As shown in Figure 2.9 (d)–(f), the increase of precursor concentration showed a significant effect on the increase in the number of the nucleation sites. However, since increasing precursor concentration corresponds to an increase in the Ti source, overall growth of the nanorods was accelerated both laterally and vertically.

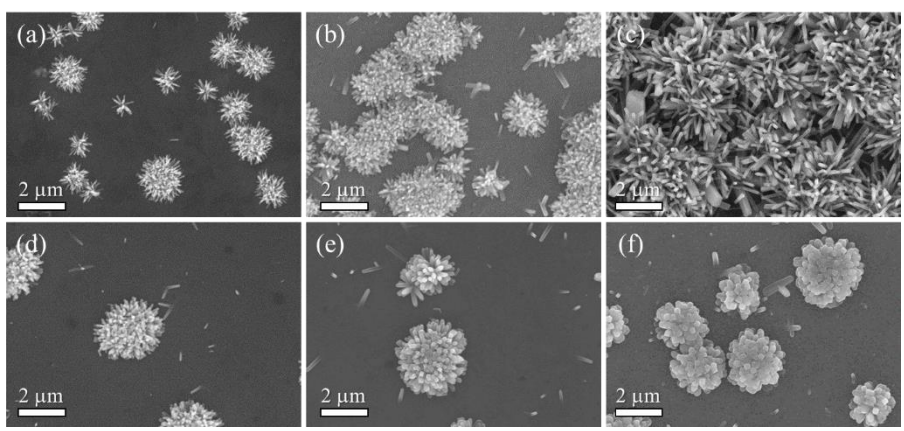

Figure 2.9 Surface morphologies of the TiO_2 nanorods hydrothermally grown on *p*-Si substrates for various growth time (a) 2 hours, (b) 3 hours and (c) 5 hours; and for various Ti precursor concentrations (d) 50.9 mM, (e) 59.3 mM and (f) 67.6 mM

2.3.5 Concentration of the Hydrochloric Acid

The growth and morphology of the TiO_2 nanorods are significantly influenced by the acidity of the solution as briefly stated in the section 2.3.1. Figure 2.10 represents the morphological changes with the HCl concentrations from 6.1 to 7.0 M under the conditions in which the synthesis temperature, time, and precursor concentrations were fixed. The morphology of the nanorods was drastically affected by changing the moles of HCl in the solution, compared to other variations. In other words, the increase in the number of moles of HCl resulted in the formation of thinner, sharper rods and the reduction in the number of relative nucleation sites. Thus, it can be elucidated that the adsorption of the Cl^- ions on the {110} planes was taken place effectively, resulting in the suppression of the lateral growth of the nanorods during the hydrothermal synthesis.

One interesting feature is that the particles, which can be defined as initial state of the growth were observed as shown in Figure 2.10 (d)–(f), providing a clue for the analysis of the growth mechanism. The stable morphology of the TiO_2 should be a hexahedron (a rod shape), which consists of four {110} planes for side faces and two {001} planes for top and bottom, in the thermodynamical and kinetical considerations. The nuclei could possess a spherical shape to reduce the entire surface energy at the initial stage of the nucleation. Through an extended synthesis the building unit can be attached on the nuclei, resulting in a development of the stable planes. The four {110} planes developed are formed as side faces and grown in the [001] direction, which finally can be a rod shape. Clusters were formed by several hexahedrons with well-defined facets at the low moles of HCl. However, the number of the hexahedrons decreased in a cluster, finally it became a tiny single hexahedron, as the concentration of the HCl is increased up to 7.0 M. The existence of the particles composed of several well-defined-facet hexahedrons indicates that it is possible to grow in various directions (in fact, they are [001] directions in individual crystals) from the one point. Same as the growth form the FTO substrate

(the growth on FTO substrates will be discussed in the next section), a growth of the individual rods can be suppressed when they reach adjacent rods, resulting in enabling the lateral growth only. Thus, the final morphology became a bulky cauliflower shape. Furthermore, due to the fact that the number of Cl^- ions increased with the increase of the number of moles of HCl, so that the growth along the <110> is effectively inhibited, resulting in thinner and sharper rods. For a prolonged growth, each cluster developed into the shape of cauliflowers and the shape of chrysanthemum with HCl concentrations, respectively.

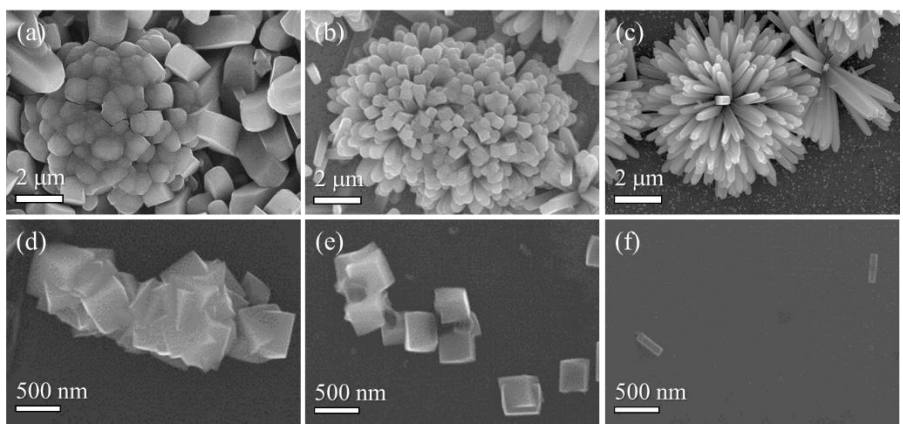

Figure 2.10 Surface morphologies of the TiO_2 nanorods hydrothermally grown on *p*-Si substrates for various HCl concentration: 6.1 M for (a) and (d); 6.7 M for (b) and (e); 7.0 M for (c) and (f)

2.3.6 Synthesis on Various Substrates

In order to understand the growth mechanism of the TiO_2 nanorods, the hydrothermal synthesis with various substrates (FTO, TiO_2 single crystal with different orientations) were carried out. The FTO substrate has great advantages of not only a transparent conducting substrate but also negligible lattice mismatch with TiO_2. The single crystal TiO_2 substrates with various orientations were introduced to investigate the growth behaviors upon the identical material. The morphologies of the hydrothermally grown TiO_2 on single crystal TiO_2 substrates with (001), (101),

and (110) orientations are shown in the Figure 2.11. By hydrothermal synthesis, the surface morphologies showed different characteristics on the orientations as well as the surface roughness. TiO_2 grew in the form of film on the polished surface (Figure 2.11 (a)–(c)) whereas it formed rods on the unpolished (backside) surface (Figure 2.11 (d)–(f)). In addition, only few rods remaining the clean surface can be observed on the polished (110) surface. Moreover, the crystallographic orientations of the films and cracks on polished surfaces (generated to reduce the strain during the formation of the film on polished surfaces) formations can be identified by considering the orientation of the substrates and observing surface of the films shown as Figure 2.12 (a)–(c). The ~50 nm-scale square shape specific features were uniformly distributed as marked in the Figures 2.12 (a) and (b). From each lattice plane in the unit cell shown in Figure 2.12 (d)–(f), it can be confirmed that the specific features have the identical orientation of the single nanorod, which have four {110} for the side faces and {001} planes for the top and bottom faces. In fact, the growth of the film on (110) substrate was inhibited due to the lowest surface energy, so that any distinguish feature is noticeable. Furthermore, the direction of the cracks can be identified as approximately <110> and <100> directions in the substrate with (001) orientation and <100> and <110> directions in that with (101) orientation. The formation of the features and cracks with the specific directions, and of few rods on (110) oriented substrate can be elucidated by the surface energy of each lattice plane in the TiO_2. Even though the growth occurred in the form of film on the (001), (101) oriented substrates and it was remarkably suppressed on (110) substrate, the growth mechanism is consistent. In detail, the TiO_2 nanorod grows to form a {110} as a side faces to minimize the surface energy of the rod, and especially the Cl^- ions were adsorbed on {110} surfaces, resulting in effectively suppression of the lateral growth. The growth of the nanorods is strongly influenced by the surface conditions such as the lattice mismatch, roughness, and orientations. The rods can be grown from the surface if the lattice mismatch is negligible such as the FTO substrate, even though the substrate has randomly oriented rough surface. On the TiO_2 substrates, TiO_2 film

with the identical orientation of the substrate can be synthesized, if the roughness of the surface is low enough. The effects of the synthesis parameters for the hydrothermally grown the TiO_2 nanorods on the morphological evolutions were represented in Figure 2.13.

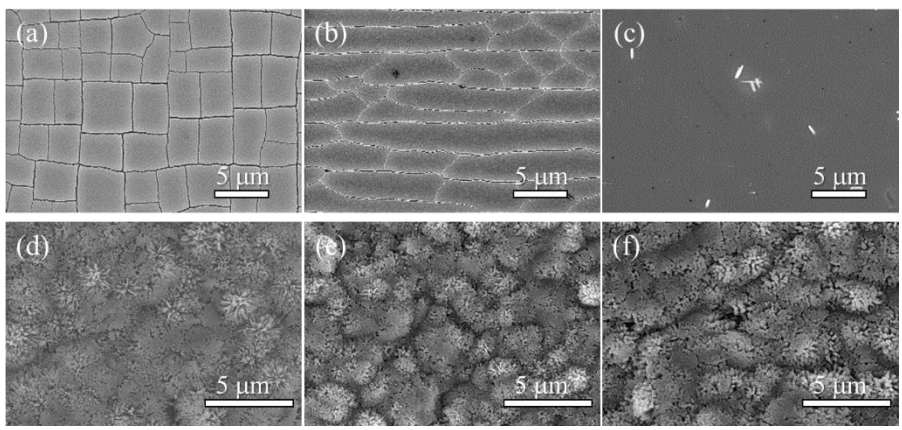

Figure 2.11 Surface morphologies of the hydrothermally grown the TiO_2 structures on TiO_2 single crystal substrates with diverse crystallographic orientations: (a) TiO_2 (001) polished surface, (b) TiO_2 (101) polished surface, (c) TiO_2 (110) polished surface, (d) TiO_2 (001) unpolished surface, (e) TiO_2 (101) unpolished surface, and (f) TiO_2 (110) unpolished surface

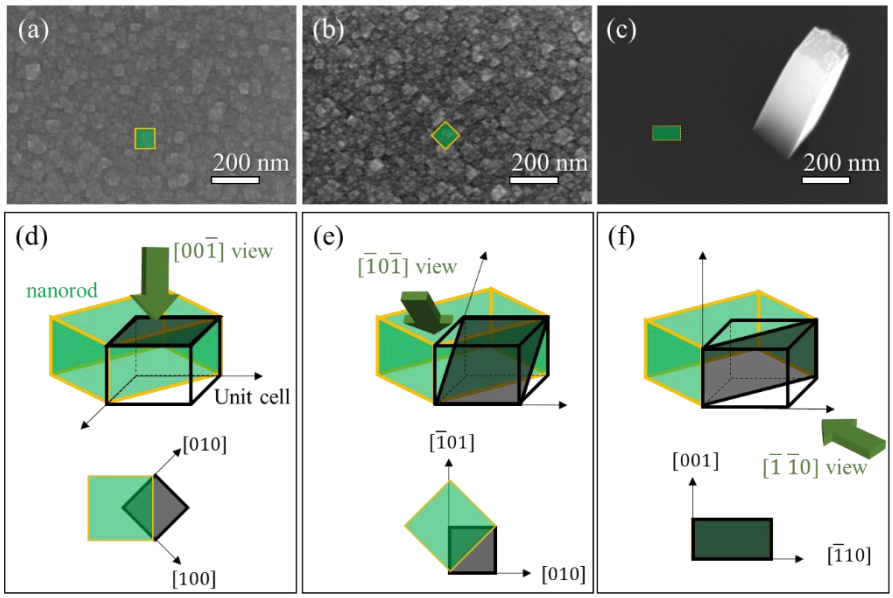

Figure 2.12 High magnification SEM images of the surface morphologies after the hydrothermal synthesis on the single crystal TiO_2 substrates with the various orientation; (a) TiO_2 (001), (b) TiO_2 (101), and (c) TiO_2 (110) substrates, Crystallographic relations between the substrate and TiO_2 nanostructure; (d) TiO_2 (001), (e) TiO_2 (101), and (f) TiO_2 (110) substrates, The green rectangular marks in (a)-(c) corresponds to those in the bottom row of the (d)-(f)

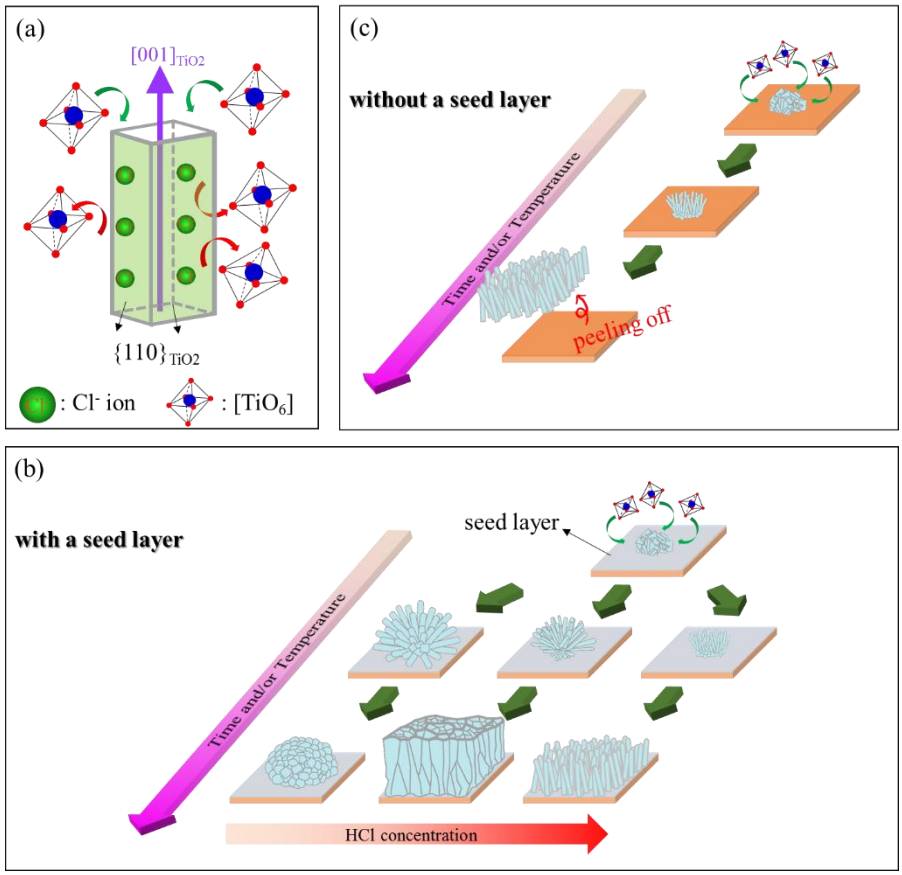

Figure 2.13 Schematic growth mechanism for TiO_2 nanorods during the hydrothermal synthesis: TiO_2 nanorods were preferentially grown along the [001] direction, which are originated from the selectively absorption of Cl^- ions on {110} plane of the TiO_2 nanorods, morphological evolutions of the TiO_2 nanostructures on a substrate (b) with a seed layer and (c) without a seed layer under the various synthesizing conditions

2.4 Summary

The growth of the nanorods is strongly affected by the surface energy of lattice planes during the hydrothermal process. It can be elucidated that forming a rod shape is attributed to the surface energy of the (110) plane is lowest and that of the (001) is highest in the rutile TiO_2. Thus, the nanorods synthesized have {110} for the side faces and grow along the [001] direction.

The solution chemistry, especially the concentration of HCl, is one of the crucial parameters for hydrothermal synthesis and can have a critical role to control the morphology of the rods. It is noted that the Cl^- ions in the solution can selectively adsorbed on to the {110} planes of the rutile crystals and can stabilize those planes, resulting in effectively suppression of the lateral growth of the nanorods. Hence, the thinner and sharper nanorods can be obtained under the higher molarity of HCl solution even though the entire growth kinetics can be decelerated with a higher HCl concentration.

Finally, the morphology of the nanorods can be influenced by the surface condition of the substrate such as the lattice mismatch, roughness, and orientation

2.5 References

1. A. Fujishima and K. Honda, *Nature*, 1972, **238**, 37.
2. M. Gratzel, *Nature*, 2001, **414**, 338-344.
3. M. Adachi, Y. Murata, J. Takao, J. Jiu, M. Sakamoto and F. Wang, *J Am Chem Soc*, 2004, **126**, 14943-14949.
4. E. Hosono, S. Fujihara, K. Kakiuchi and H. Imai, *J Am Chem Soc*, 2004, **126**, 7790-7791.
5. Q. H. Zhang and L. Gao, *Langmuir*, 2003, **19**, 967-971.
6. Y. W. Jun, M. F. Casula, J. H. Sim, S. Y. Kim, J. Cheon and A. P. Alivisatos, *J Am Chem Soc*, 2003, **125**, 15981-15985.
7. P. D. Cozzoli, A. Kornowski and H. Weller, *J Am Chem Soc*, 2003, **125**, 14539-14548.
8. R. Tenne and C. N. R. Rao, *Philosophical Transactions of the Royal Society of London. Series A: Mathematical, Physical and Engineering Sciences*, 2004, **362**, 2099-2125.
9. Y. N. Xia, P. D. Yang, Y. G. Sun, Y. Y. Wu, B. Mayers, B. Gates, Y. D. Yin, F. Kim and Y. Q. Yan, *Advanced Materials*, 2003, **15**, 353-389.
10. K. Shankar, J. Bandara, M. Paulose, H. Wietasch, O. K. Varghese, G. K. Mor, T. J. LaTempa, M. Thelakkat and C. A. Grimes, *Nano Lett*, 2008, **8**, 1654-1659.
11. G. K. Mor, K. Shankar, M. Paulose, O. K. Varghese and C. A. Grimes, *Nano Lett*, 2005, **5**, 191-195.
12. M. Grätzel, *Journal of Photochemistry and Photobiology A: Chemistry*, 2004, **164**, 3-14.
13. M. K. B. Ahmad and K. Murakami, *Journal of Advanced Research in Physics*, 2012, **3**.
14. J. K. Oh, J. K. Lee, S. J. Kim and K. W. Park, *Journal of Industrial and Engineering Chemistry*, 2009, **15**, 270-274.

15. X. S. Fang, Y. Bando, U. K. Gautam, C. Ye and D. Golberg, *Journal of Materials Chemistry*, 2008, **18**, 509-522.
16. R. Wang, K. Hashimoto, A. Fujishima, M. Chikuni, E. Kojima, A. Kitamura, M. Shimohigoshi and T. Watanabe, *Nature*, 1997, **388**, 431-432.
17. A. Hagfeldt and M. Gratzel, *Chemical Reviews*, 1995, **95**, 49-68.
18. M. R. Hoffmann, S. T. Martin, W. Y. Choi and D. W. Bahnemann, *Chemical Reviews*, 1995, **95**, 69-96.
19. A. L. Linsebigler, G. Q. Lu and J. T. Yates, *Chemical Reviews*, 1995, **95**, 735-758.
20. X. Chen and S. S. Mao, *Chem Rev*, 2007, **107**, 2891-2959.
21. A. Fujishima, T. N. Rao and D. A. Tryk, *Journal of Photochemistry and Photobiology C Photochemistry Reviews*, 2000, **1**.
22. G. K. Mor, H. E. Prakasam, O. K. Varghese, K. Shankar and C. A. Grimes, *Nano Letters*, 2007, **7**, 2356-2364.
23. T. Wang, S. Wang, W. X. Chen, W. Wang, Z. L. Xu, Y. Liu and T. Hori, *Journal of Materials Chemistry*, 2009, **19**, 4692-4694.
24. A. Mills and S. LeHunte, *J Photoch Photobio A*, 1997, **108**, 1-35.
25. Z. Zhang, C.-C. Wang, R. Zakaria and J. Y. Ying, *Journal of Physical Chemistry B*, 1998, **102**.
26. J. T. Jiu, F. M. Wang and M. Adachi, *Materials Letters*, 2004, **58**, 3915-3919.
27. G. M. Wang, H. Chen, H. Zhang, C. W. Yuan, Z. J. Lu, G. M. Wang and W. Y. Yang, *Applied Surface Science*, 1998, **135**, 97-100.
28. J. H. Chang, A. V. Ellis, Y. H. Hsieh, C. H. Tung and S. Y. Shen, *Science of the Total Environment*, 2009, **407**, 5914-5920.
29. M. Y. Song, D. K. Kim, S. M. Jo and D. Y. Kim, *Synthetic Metals*, 2005, **155**, 635-638.
30. L. Zhou, D. S. Boyle and P. O'Brien, *Chem Commun (Camb)*, 2007, DOI: 10.1039/b611476h, 144-146.

31. M. Addamo, M. Bellardita, A. Di Paola and L. Palmisano, *Chem Commun (Camb)*, 2006, DOI: 10.1039/b612172a, 4943-4945.
32. B. O'Regan and M. Gratzel, *Nature*, 1991, **353**.
33. Y. Matsumoto, Y. Ishikawa, M. Nishida and S. Ii, *Journal of Physical Chemistry B*, 2000, **104**, 4204-4209.
34. S. Kobayashi, K. Hanabusa, N. Hamasaki, M. Kimura and H. Shirai, *Chemistry of Materials*, 2000, **12**.
35. E. Hosono, S. Fujihara, H. Imai, I. Honma, I. Masaki and H. Zhou, *ACS Nano*, 2007, **1**, 273-278.
36. C. Wu, L. Lei, X. Zhu, J. Yang and Y. Xie, *Small*, 2007, **3**, 1518-1522.
37. Z. Liu, D. D. Sun, P. Guo and J. O. Leckie, *Chemistry*, 2007, **13**, 1851-1855.
38. J. Du, J. Zhang, Z. Liu, B. Han, T. Jiang and Y. Huang, *Langmuir*, 2006, **22**, 1307-1312.
39. G. F. Zou, H. Li, Y. G. Zhang, K. Xiong and Y. T. Qian, *Nanotechnology*, 2006, **17**, S313-S320.
40. H. G. Yang and H. C. Zeng, *J Am Chem Soc*, 2005, **127**.
41. C. C. Weng, K. F. Hsu and K. H. Wei, *Chemistry of Materials*, 2004, **16**, 4080-4086.
42. Z. Y. Yuan and B. L. Su, *Colloid Surface A*, 2004, **241**, 173-183.
43. S. S. Mali, C. A. Betty, P. N. Bhosale and P. S. Patil, *Crystengcomm*, 2011, **13**, 6349-6351.
44. C. Sun, N. Wang, S. Zhou, X. Hu, S. Zhou and P. Chen, *Chem Commun (Camb)*, 2008, 3293-3295.
45. E. Matijevic, *Langmuir*, 1986, **2**, 12-20.
46. T. Sugimoto, *Advances in Colloid and Interface Science*, 1987, **28**, 65-108.
47. J. Livage, M. Henry and C. Sanchez, *Prog Solid State Ch*, 1988, **18**, 259-341.
48. M. A. Anderson, M. J. Gieselmann and Q. Y. Xu, *Journal of Membrane Science*, 1988, **39**, 243-258.

49. E. A. Barringer and K. K. Bowen, *Langmuir*, 1985, **1**.

50. J. H. Jeam and T. A. Ring, *Langmuir*, 1986, **2**.

51. J. L. Look and C. F. Zukoski, *Journal of the American Ceramic Society*, 1992, **75**, 1587-1595.

52. B. A. Morales, O. Novaro, T. López, E. Sánchez and R. Gómez, *Journal of Materials Research*, 2011, **10**, 2788-2796.

53. D. Vorkapic and T. Matsoukas, *J Colloid Interface Sci*, 1999, **214**, 283-291.

54. R. L. Penn and J. F. Banfield, *Geochimica Et Cosmochimica Acta*, 1999, **63**, 1549-1557.

55. C. J. Barbe, F. Arendse, P. Comte, M. Jirousek, F. Lenzmann, V. Shklover and M. Gratzel, *Journal of the American Ceramic Society*, 1997, **80**, 3157-3171.

56. H. Z. Zhang and J. F. Banfield, *Journal of Materials Chemistry*, 1998, **8**, 2073-2076.

57. H. Z. Zhang and J. F. Banfield, *Journal of Physical Chemistry B*, 2000, **104**, 3481-3487.

58. A. Navrotsky, *Geochemical Transactions*, 2003, **4**, 34.

59. P. K. Naicker, P. T. Cummings, H. Z. Zhang and J. F. Banfield, *Journal of Physical Chemistry B*, 2005, **109**, 15243-15249.

60. K. Kakiuchi, E. Hosono, H. Imai, T. Kimura and S. Fujihara, *Journal of Crystal Growth*, 2006, **293**, 541-545.

61. D. Dambournet, I. Belharouak and K. Amine, *Chemistry of Materials*, 2010, **22**, 1173-1179.

62. Y. X. Zhang, G. H. Li, Y. X. Jin, Y. Zhang, J. Zhang and L. D. Zhang, *Chemical Physics Letters*, 2002, **365**, 300-304.

63. L. Dong, Y. Ma, Y. W. Wang, Y. T. Tian, G. T. Ye, X. L. Jia and G. X. Cao, *Materials Letters*, 2009, **63**, 1598-1600.

64. Y. J. Kim, M. H. Lee, H. J. Kim, G. Lim, Y. S. Choi, N.-G. Park, K. Kim and W. I. Lee, *Advanced Materials*, 2009, **21**, 3668-3673.

65. S. S. Mali, P. S. Shinde, C. A. Betty, P. N. Bhosale, W. J. Lee and P. S. Patil, *Applied Surface Science*, 2011, **257**, 9737-9746.

66. S. S. Mali, S. K. Desai, D. S. Dalavi, C. A. Betty, P. N. Bhosale and P. S. Patil, *Photochem Photobiol Sci*, 2011, **10**, 1652-1658.

67. B. Liu and E. S. Aydil, *J Am Chem Soc*, 2009, **131**, 3985-3990.

68. N. Viriya-empikul, T. Charinpanitkul, N. Sano, A. Soottitantawat, T. Kikuchi, K. Faungnawakij and W. Tanthapanichakoon, *Materials Chemistry and Physics*, 2009, **118**, 254-258.

69. X. Li, Y. Xiong, Z. Li and Y. Xie, *Inorg Chem*, 2006, **45**, 3493-3495.

70. Q. Zhang, S. J. Liu and S. H. Yu, *Journal of Materials Chemistry*, 2009, **19**, 191-207.

71. J. H. Park, S. Kim and A. J. Bard, *Nano Lett*, 2006, **6**, 24-28.

72. J. B. Baxter and E. S. Aydil, *Applied Physics Letters*, 2005, **86**, 053114.

73. M. Law, L. E. Greene, J. C. Johnson, R. Saykally and P. Yang, *Nat Mater*, 2005, **4**, 455-459.

74. A. P. Alivisatos, *J Phys Chem-Us*, 1996, **100**, 13226-13239.

75. X. Chen, Y. Lou, S. Dayal, X. Qiu, R. Krolicki, C. Burda, C. Zhao and J. Becker, *J Nanosci Nanotechnol*, 2005, **5**, 1408-1420.

76. M. Ramamoorthy, D. Vanderbilt and R. D. King-Smith, *Physical Review B*, 1994, **49**, 16721-16727.

77. G. Liu, H. G. Yang, J. Pan, Y. Q. Yang, G. Q. Lu and H. M. Cheng, *Chem Rev*, 2014, **114**, 9559-9612.

78. J. Lin, Y. U. Heo, A. Nattestad, Z. Sun, L. Wang, J. H. Kim and S. X. Dou, *Sci Rep*, 2014, **4**, 5769.

79. A. S. Barnard and P. Zapol, *Journal of Physical Chemistry B*, 2004, **108**, 18435-18440.

80. A. S. Barnard and L. A. Curtiss, *Nano Lett*, 2005, **5**, 1261-1266.

81. N. Satoh, T. Nakashima and K. Yamamoto, *Sci Rep*, 2013, **3**, 1959.

82. T.-D. Nguyen Phan, H.-D. Pham, T. V. Cuong, E. J. Kim, S. Kim and E. W. Shin, *Journal of Crystal Growth*, 2009, **312**, 79-85.

83. P. M. Oliver, G. W. Watson, E. T. Kelsey and S. C. Parker, *Journal of Materials Chemistry*, 1997, **7**, 563-568.

84. N. M. Kinsinger, A. Wong, D. Li, F. Villalobos and D. Kisailus, *Crystal Growth & Design*, 2010, **10**, 5254-5261.

85. J. Su and L. Guo, *RSC Advances*, 2015, **5**, 53012-53018.

86. V. Jordan, U. Javornik, J. Plavec, A. Podgornik and A. Recnik, *Sci Rep*, 2016, **6**, 24216.

87. X. Y. Wang, Y. Liu, X. Zhou, B. J. Li, H. Wang, W. X. Zhao, H. Huang, C. L. Liang, X. Yu, Z. Liu and H. Shen, *Journal of Materials Chemistry*, 2012, **22**, 17531-17538.

Chapter 3

2D-MoS_2/TiO_2 nanorods heterostructure on *p*-type Silicon Photocathodes for Water Splitting by Hydrothermal Methods

3.1 Introduction

Solar energy as the energy source of direct solar water splitting for hydrogen production, illuminates on the earth constantly. In order to achieve the efficient conversion and utilization of solar energy or for storage it in another form, solar water splitting can be one of the most crucial solutions to the energy issues. Direct water splitting has been regarded as one of the more practical and efficient ways to deal with the huge amount of solar power, in which the solar energy is converted and stored in the form of chemical energy.[1] Hence, hydrogen production as one of the most potential methods to generate the renewable energy, is considered to be the optimum way to solve the several energy issue. After the first report about the Photoelectrochemical of water using TiO_2 as a Photoelectrode by Honda and Fujishima[2], many researchers have focused on the direct solar water splitting.

As a superior photoelectrode, Si is the most widely investigated among the diverse photoelectrode materials for the direct water splitting[3-6] because of the suitable bandgap of 1.12 eV, which is capable of absorbing the widest range of entire solar spectrum. However, a Si photoelectrode has a disadvantage that is vulnerable to photocorrosion due to the position of redox potentials.[7] The photocorrosion of the Si photoelectrode occurs through the PEC, EC, and chemical routes. During the PEC and EC routes, net charge transfer is required while degradation and dissolution takes places without the net charge transfer in the chemical corrosion.[8] The corrosion enables to form a surface defect such as an oxide layer. It has been reported that the thick oxide layer on Si surface can prohibit the transfer of the minority carriers from the Si to an electrolyte vice versa.[8]

Furthermore, huge amount of the entire incident light is reflected (~37 %) because the reflective index of the Si is higher than 4.0.[9-11] These critical advantages (rapid photocorrosion and high reflective index) negatively affect not only the STH efficiency but also the life of the PEC cell.[4] Especially, there are several physical means are implied when the TiO_2 thin film is introduced as a passivation layer for *p*-

Si. TiO_2 is a *n*-type semiconductor with a wide bandgap of 3.0–3.2 eV). The heterojunction is generated when TiO_2 thin film is deposited on a *p*-Si substrate at the interface of the TiO_2 and *p*-Si. Moreover, the electron affinity of p-Si (X_{Si} = 4.0 eV)[12] is slightly lower than that of the TiO_2 (X_{TiO2} = 4.3–4.5 eV),[13, 14] and the work function of the *p*-Si is higher than that of the TiO_2. Thus, the transport of the photogenerated carriers (electrons) from the *p*-Si to the site of the hydrogen evolution reaction (HER) via TiO_2 is facilitated due to the band alignment and resulting band bending.[15] In addition, incident light can be sufficiently transmitted since the transmittance of the TiO_2 thin film under visible light region.[15] Several advantages can be obtained by using the TiO_2 nanorods compared to TiO_2 thin film. First of all, a much larger number of reaction sites can be provided since the surface area is significantly increased. In addition, the reflection of the incident light on the *p*-Si surface can be effectively reduced.[15]

In order to achieve high efficiency and high performance, catalysts can be introduced for the sustainable hydrogen production by direct solar water splitting. As the requirements of the material itself, highly active, inexpensive, and earth-abundant materials are required in the selection of catalysts. To date, noble metals such as Pt, Ru, Rh, Au, and Ir or their oxides such as RuO_2 and IrO_2 have been commonly used for catalysts in the solar water splitting systems.[16-22] Among the catalysts, Pt has been regarded as the most powerful catalysts for the hydrogen production because the overpotential is negligible and the it has superior kinetics on HER.[23] However, the cost issue is one of the critical disadvantage.[16] Due to the weakness of the noble metal catalysts, two-dimensional-transition metal dichalcogenide (2D-TMD) can be a suitable candidate to address the need for a new catalyst. As a catalyst with distinct structural characteristics practical application of 2D-TMD becomes higher. Especially, in terms of the structure of the 2D characteristic, 2H–MoS_2 is a semiconductor which exhibits the high stability.[24] Furthermore, the type II heterojunction can be formed by hybridization TiO_2 with MoS_2 since the conduction band of the few layer of the 2H–MoS_2 is lied above the that of the TiO_2.[24] The entire

performance of the PEC cells can be improved by the formation of the heterostructure because the photogenerated carriers are trapped at the surface of the MoS_2, resulting in the reduction of the e–h recombination rate effectively. In addition, the MoS_2 is regarded to one of the promising materials possessing the roles as the not only the photocatalyst but also the reaction site itself for the HER. There are several reports on the enhancement of HER performance using MoS_2 as a catalyst, which has received much attention recently.[25, 26] The higher efficiency, leading to improving the HER activity, have been obtained by using MoS_2 on CdS.[25] In addition, the improvement for photocatalytic activity under visible-light region have been achieved with MoS_2/TiO_2 nanobelt heterostructure.[27]

3.1.1 Atomic Structure of the 2D-MoS_2

The TMD materials are formed by the combination of a transition metal and a chalcogen atom as shown in Figure 3.1. The polymorphs of the TMDs are defined by their stacking sequences. In detail, a monolayer TMD consists of three atomic planes. The three layers are the forms of X–T–X, in which the transition metal (T) is connected to the six chalcogen atoms (X). For example, the atomic structure of the MoS_2[28] is shown in Figure 3.2. The chalcogen atoms of sulfur are placed at the top and the bottom layers and the transition metal atom of molybdenum is located at the middle of the layers, revealing a layered structure.[23, 29] The typical thickness of a TMD monolayer exhibits ~6–7 Å .[23, 30, 31] In terms of the stacking sequence, the hexagonal stacking of a layer with the thickness (= van der Waals gap) determines the formation of the polymorphs. The TMD commonly has three polymorphs classified into the 1T, 2H, and 3R, in which each latter corresponds to the crystal structures (trigonal, hexagonal, and rhombohedral) and the numbers indicates the number of layers in each unit cell.[23, 29] The 2H phase has a trigonal prismatic coordination with the hexagonal symmetry stacking and consists of two layers (such as AbA BaB stacking; the capital and lower-case latter denote the Chalcogen and

transition metals, respectively.).[7, 23] The 3R phase, on the other hand, also has a trigonal prismatic coordination with the rhombohedral symmetry and contains three layers (AbA CaC BcB stacking).[32] The stacking sequences of the TMD materials and resulting structures[33] are displayed in Figure 3.3.

The 2H phase is the dominant phase in nature and is more stable than the 3R phase. The 1T phase is a metallic phase, where a transition metal, such as Mo, is located in the octahedral center (AcB stacking)[34] Even though the 1T phase exhibits a superior electrical property as a metallic phase,[35-38] the 1T phase can be transformed into the 2H phase by a calcination and/or aging because it is unstable.[23]

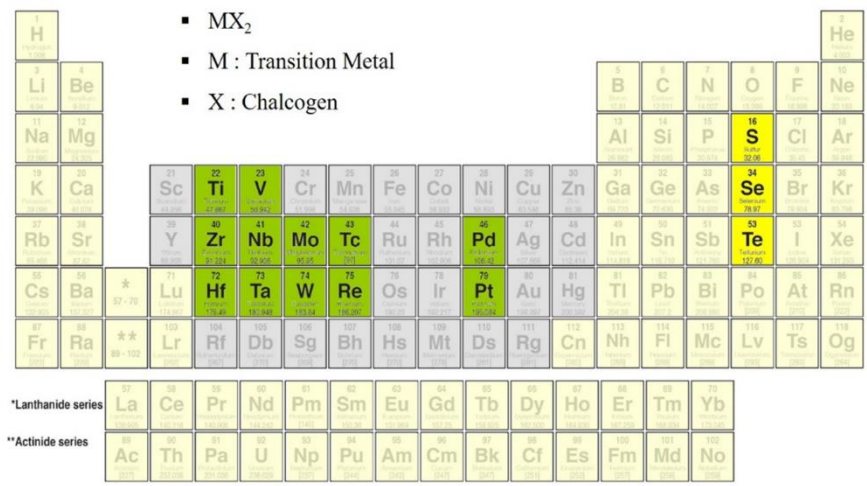

Figure 3.1 The periodic table highlighted with the transition metals shaded in green and the three chalcogen elements shaded in yellow

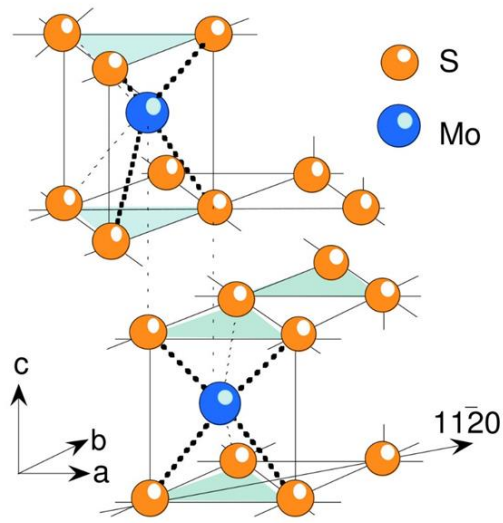

Figure 3.2 The typical atomic structure of the layered MoS_2[28]

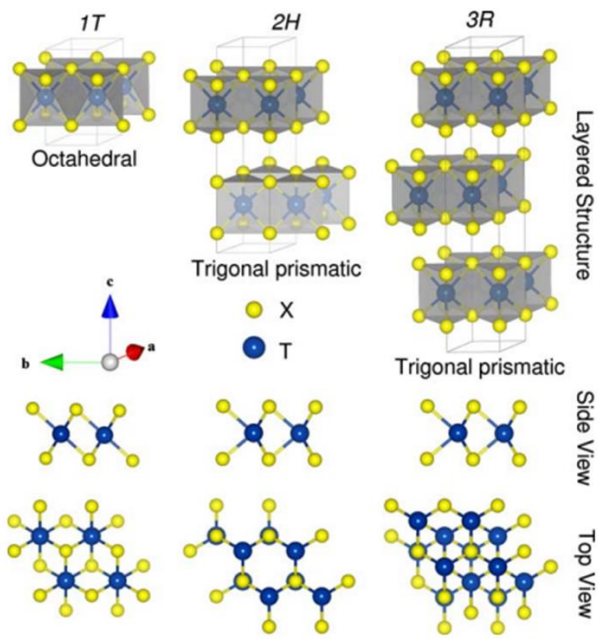

Figure 3.3 The layered structures of a 2D-TMD material, where the stacking sequence determines a phase of the layered 2D-TMD material[33]

3.1.2 Electrical Structure of the 2D-MoS2

The electrical structure of the MoS_2 as a promising photocatalyst, should possess a high stability and a proper energy band structure. The conduction band of the bulk MoS_2 is slightly positive than the hydrogen evolution reaction (HER) potential. However, it is noted that the band gap of the MoS_2 is gradually changed with the number of layers of MoS_2.[23, 39] Particularly, the indirect band gap (1.3 eV) is changed into the direct band gap (1.9 eV) when the thickness of the MoS_2 is reduced down to the monolayer level.[23, 40-42] Thus, the quantum confinement has been adopted, which affects the band gap of the semiconductors to control the band gap of the MoS_2, resulting in tuning a photocatalytic activity of the MoS_2. Therefore, the valance band of the MoS_2 can be shifted more positively, granting a higher oxidation potential.

The effects of the MoS_2 on the catalytic activity for the hydrogen production has been reported.[43] Recently, several researches about the hydrogen production by using the MoS_2 as a co-catalyst have investigated.[20, 21, 44] It is interesting to note that the distribution in the edge site of the MoS_2 has a linear relation to the electrocatalytic activity.[45] The MoS_2 has numerous distinguish surface edges and the motility of the electron or hole along a basal plane is much faster (over 1 order) than that along the perpendicular direction of the layer. The surface of the bulk MoS_2 is composed of the basal planes thermodynamically, which is catalytically inert[46-48] whereas the edge of the MoS_2 exhibits the high activity in HER.[49] The hydrogen binding energy of Mo $(\bar{1}011)$ edge of MoS_2 (0.08 eV; the value is the similar to that of the noble metals such as Pt.) is considerably closer to the optimum value of 0 eV in the In the theoretical density functional theory (DFT) calculations.[50-52] Thus, MoS_2 can be a promising material as a not only effective catalyst but also a photoactive material itself for the hydrogen evolution reaction.

In this chapter, the photoelectrochemical properties and microstructural analysis of the heterostructure of the hydrothermally synthesized TiO_2 nanorods and two

dimensional MoS_2 on the *p*-Si for the applications in the hydrogen production by the direct solar water splitting will be discussed.

3.2 Experimental Procedures

TiO_2 nanorods Synthesis on *p*-Si

A single-side-polished *p*-Si (100) wafer was cut into 2 cm × 2 cm and cleaned carefully with same method as FTO substrates. A piece of cleaned wafer was soaked in 2% hydrofluoric acid (HF) for 1 minute to remove the SiO_2 native oxide layer and organic residues on the polished surface. Right after the HF etching, etched surfaces were rinsed with DI water for 1 minute. 5–20 nm–thick TiO_2 film was deposited as a passivation layer and a seed layer using an electron-beam evaporator (KVE-E2004L), of which deposition rate was controlled for 0.2 $Å \cdot sec^{-1}$. TiO_2 film deposited *p*-Si substrates were annealed at 500 ℃ in a tube furnace with N_2 atmosphere. After the annealing, TiO_2 nanorods were synthesized by the hydrothermal method. Briefly, 2 ml (34.1–67.6 mM) of TTIP was dissolved at room temperature under vigorous magnetic stirring in the mixture of 5.5–7.3 M HCl aqueous solution. The stirring was continued until the mixture solution became transparent. After the TiO_2 film deposited *p*-Si substrate was placed at the bottom of the Teflon vessel, of which the film side was facing up, 50 ml of the mixture solution was filled into the vessel. The Teflon vessel was put into a stainless steel autoclave. Tightly sealed autoclave was placed in the box furnace. Then, the growth of the TiO_2 nanorods was conducted for 1.5–5 hours at 200 ℃. After the growth process, the autoclaves were naturally cooled down to the room temperature. The substrates were taken out from the vessel and were washed carefully with DI water several times and were dried. The dried substrates were annealed in a tube furnace with N_2 atmosphere at 500 ℃ for 30 minutes. In particular, the tube was purged with N_2 for 2 hours before the annealing was started and the heating rate is 5 $℃ \cdot min^{-1}$

2D-TMD/TiO_2 Heterostructure

The 2D-MoS_2/TiO_2 heterostructure was synthesized by a hydrothermal reaction. Briefly, 2.2–13.2 mg (0.17–1 mM) of $(NH_4)_2MoS_4$ powder as a precursor was dissolved in 50 ml of N, N–dimethylformamide (DMF) solution. The solution was sonificated for 30 minutes. After the sonification, 25 ml of the solution was filled into the Teflon vessel, in which the as-grown substrates ware placed at the bottom. The film surfaces were faced up during the synthesizing. Then, the Teflon was transferred into the stainless-steel autoclave and tightly sealed. The Autoclave was placed into the furnace and the growth process was carried out at 200 ℃ for 10 hours. After the growth process, the autoclave was naturally cooled in the furnace. The substrates were taken from the Teflon vessel and rinsed with DI water several times carefully and were dried in the air.

PEC performance

Photocurrent measurements of all samples synthesized were performed using a three-electrode configuration, the *p*-Si substrates with the nanostructured materials as a working electrode, a saturated calomel as the reference electrode, and a platinum foil (1.5 cm × 3 cm) as the counter electrode. The measured potential V vs. calomel were converted to reference hydrogen electrode (RHE) using the following equation.

$$V_{RHE} = E + E_{calomel} + 0.059 \times pH$$

Where E is applied potential vs. calomel and calomel is 0.24 V vs RHE and V_{RHE} is the applied bias potential vs. RHE. The 0.5 M H_2SO_4 standard aqueous solution was used as the electrolyte. An electrochemical workstation (Ivium Technologies, Model: Nstat) was used to measure linear sweep voltammetry (LSV) characteristics of the electrode, with a scan rate of 20 $mV \cdot s^{-1}$. The illuminated areas of the working electrode were 0.3–1 cm^2. In order to obtain simulated sunlight, a Xe arc lamp under AM 1.5G simulated solar irradiation was used as the light source, and the power intensity of the light is 100 $mW \cdot cm^{-2}$. Electrochemical impedance spectroscopy (EIS) measurements were performed under the entire solar spectra illumination in 0.5 M

H_2SO_4 aqueous solution. Incident photon to current efficiency (IPCE) was measured with a light source and a monochromator at 0V vs. RHE.

Characterization

X-ray photoemission spectroscopy (XPS) was carried out on a Sigma Probe model (ThermoVG, U.K) operating at a base pressure of 5×10^{-10} mbar at 300 K with a nonmonochromatized Al K α line at 1486.6 eV, a spherical sector analyzer of 180 °, a mean diameter of 275 mm, an analysis area of 15 μm to 400 μm, and multichannel detectors. The results were corrected for charging effects by using C 1s as an internal reference and the Fermi edge of a gold sample. Ultraviolet photoemission spectroscopy (UPS) was performed by on a PHI 5000 VersaProbe with a He I (21.2eV) source.

Microstructural Analysis

Field Emission-Scanning Electron Microscope (FE-SEM).

The surface morphology of substrates was analyzed by using field-emission scanning electron microscopy (FE-SEM, Hitachi, SU-70; Carl Zeiss, Supra) at the accelerating voltage of 2-15 kV, the working distance of 5-10mm. In order to avoid the electron charge effects and to achieve a high resolution image, conducting path were connected from the sample to the SEM sample holder. Briefly, the one edge of the FTO substrate was smoothly scratched with a knife. Then, Ag paste were covered and dried in the air. On the other hand, in p-Si substrate case, the back side of the substrate was ground ~50 μm to remove the native SiO_2 layer and was immediately covered with an Ag paste over it. Finally, the samples were dried in the air.

Transmission Electron Microscope (TEM).

The transmission electron microscope (TEM, JEOL, JEM-2100F) analysis were carried out at an accelerating voltage of 200 kV, which was equipped with high-angle annular dark-field image (HADDF), scanning TEM (STEM), and energy dispersive spectroscopy (EDS). The samples for TEM analysis were prepared in

three different methods as needed; drop casting, ion-milling, and focused ion beam (FIB). First, TiO_2 nanorods synthesized were scratched off from the substrate and the powders scratched were dispersed in ethanol. The dispersion solutions were sonicated for 10 minutes. A drop of the solution was dropped onto a carbon coated copper mesh TEM grid and dried with an infrared lamp. Second, the TiO_2-grown-sides of the samples were attached facing each other with M-bond 610, which is chemically and mechanically stable in high vacuum. The samples were cut into less than 3 mm long and were polished on lapping films (the grit sizes of the films are 15–0.5 μm) in the thickness direction until the thickness was about 1 μm. After the polishing, the sample was bonded with M-bond 610 on a copper grid with an oval hole. Then, the grid was transferred into the precision ion polishing system (PIPS, Gatan, model 691) and Ar ion beam thinning was carried out at 5kV with an incident angle of 6–15°. Third, the mounted sample was placed inside a dual beam focused ion beam (FIB, Seiko, SMI3050SE). Before using the Ga^+ ion beam to prepare the samples for TEM, it was necessary to protect the surface of the sample from accelerating focused Ga^+ ions. Furthermore, these protecting layer can enhance the uniformity in terms of the milling rate of the samples. This was achieved by depositing platinum and/or carbon film with a thickness of ~ 2 μm onto the surface. This process was conducted using an accelerating voltage of 15 kV and a beam current of maximum 20 nA. After the thinning, the cross-sectioned surfaces were then smoothly polished at 5kV to remove the Ga^+ embedded damage layer during the thinning process. In order to achieve a damage-minimized-surface, Nano-mill (Fischione, M1040) cleaning was followed. The high-resolution TEM (HR-TEM) images were acquired at 200kV. The structural analysis was conducted by analyzing the Fast Fourier Transform (FFT) patterns and by measuring interplanar spacing of particular planes. In addition, scanning TEM (STEM) high-angle annular dark field (HAADF) images and Z-contrast images which are sensitive to variations in the atomic number of atoms were obtained. In order to confirm the elemental

distributions of the samples synthesized, elemental mappings were carried out by using energy-dispersive X-ray spectroscopy (EDS).

3.3 Results and Discussions

3.3.1 Surface Morphology of Hydrothermally Grown TiO_2 Nanorods on *p*-Si

Figure 3.4 shows the surface morphology of the TiO_2 nanorods on the *p*-Si substrates by the hydrothermal method. The growth of the TiO_2 nanorods is greatly affected by the thickness of the seed layers, where the thickness values were varied to investigate the effects of the thin film thickness as a passivation layer and a seed layer. In other words, as the thickness of the seed layer increases from 5 nm to 20 nm, the surface morphology of a film composed of uniform nanorods (5-nm-thick seed layer) were changed into that of a film with sparsely distributed flower-like nanorods clusters (20-nm-thick seed layer). In case of the 10 nm-thick seed layer, the flower-like nanorods clusters were overspread entire region of the substrates, forming a film. The dimensions of the nanorods were similar in length with the ~ 500 nm but were different in diameters: ~55 nm in the 5-nm-thick seed layer, ~58 nm in the 10-nm-thick seed layer, and ~60 nm in the 20-nm-thick seed layer. Furthermore, the difference in the morphology of the TiO_2 nanorods can be more clearly distinguished in the cross-sectional scanning transmission electron microscope (STEM) images in Figure 3.5. The areal density of the distribution of the TiO_2 nanorods with the thickness of the seed layer was reduced as shown in Figure 3.4 and 3.5. The only differences in terms of the morphology are the diameter and areal density of the nanorods after the identical hydrothermal synthesis as stated above. The increase in the thickness of the seed layer has a significant effect on the growth of nanorods, and the 5-nm-thick seed layer has been found to be thick enough to nucleate and grow TiO_2 nanorods. It can be elucidated that the increase in the thickness of the seed layer determines the crystal size of the TiO_2 thin film, which in turn affects not only the thickness of the rods but also the overall coverage of the subsequent hydrothermal synthesis. In the nucleation and growth of nanorods, thin film TiO_2 on the *p*-Si substrates follows the growth mechanism described in the previous chapter and

grows simultaneously in each [001] direction for all crystals at the beginning of growth. However, the nanorods which are encountered with the adjacent crystals could not grow anymore, and uninterrupted TiO_2 nanorods could allow to grow only. Therefore, as shown in the cross-sectional image in Figure 3.5, the density of nanorods is dense, forming a film, near the interface with the *p*-Si substrate, while the density gradually decreases toward the top of the nanorods and maintains a constant density near the surface. The TiO_2 thin film after the deposition by the e-beam evaporator is an amorphous phase. However, the following annealing has crystallized and stabilized the TiO_2 thin film, which in turn determines the grain size of the seed layer. As the crystal grain size becomes smaller, the development of each facet is limited. On the other hand, the crystal grain size is sufficiently large enough to form facets when a thickness of the seed layer is 20 nm. Therefore, the development of facets in each crystal (as a seed for nucleation and growth) is easier than a thin seed layer, which affects preferential growth during hydrothermal synthesis, and finally the PEC characteristics were influenced by the surface structure of the thin film TiO_2.

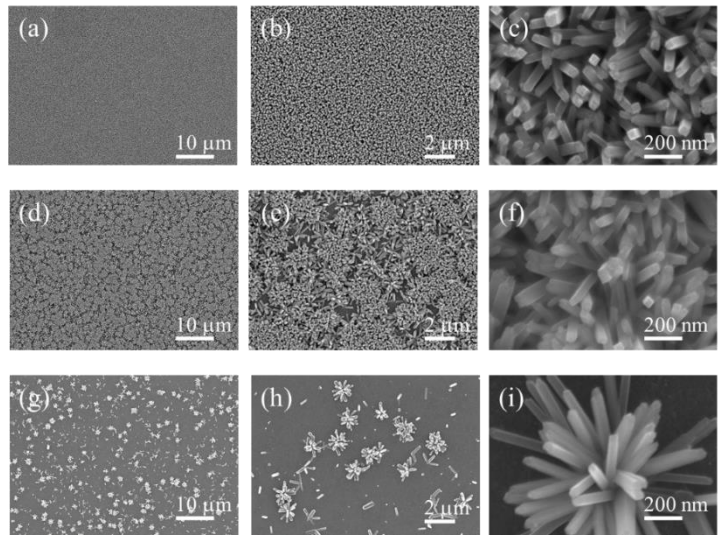

Figure 3.4 The surface morphologies of the TiO_2 nanorods on *p*-Si substrates with (a)-(c) 5-nm-thick seed layer, (d)-(f) 10-nm-thick seed layer, and (g)-(i) 20-nm-thick seed layer

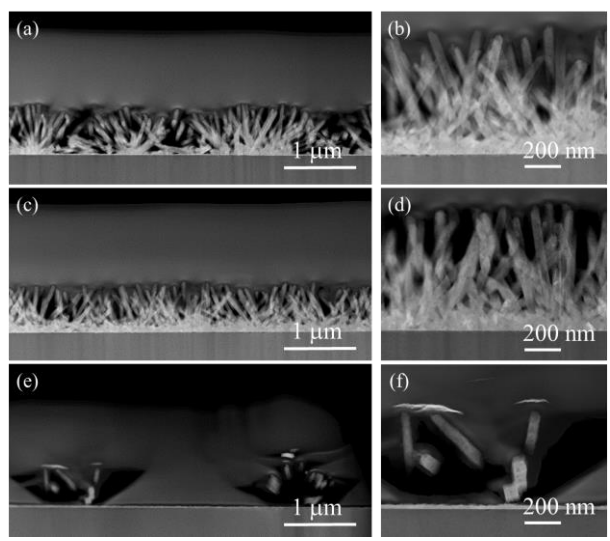

Figure 3.5 The cross-sectional STEM images of the TiO_2 nanorods on *p*-Si substrates with (a)-(b) 5-nm-thick seed layer, (c)-(d) 10-nm-thick seed layer, and (e)-(f) 20-nm-thick seed layer

3.3.2 Photoelectrochemical (PEC) Performances

The photoelectrochemical (PEC) performances were examined for the *p*-Si substrates as a photocathode, TiO_2 thin film deposited by an e-bean evaporator as a passivation layer and seed layer, TiO_2 nanorods synthesized by the facile hydrothermal method, and the MoS_2 decorated by the hydrothermal process. The labels of the photocathodes for this thesis will be used as listed in Table 3.1. Figure 3.6 and 3.7 show the linear sweep voltammetry (LSV) curves for each photocathodes. The LSVs were measured with a three-electrode set-up and a 0.5 M H_2SO_4 aqueous electrolyte without any sacrificial reagent. The surface bubbles originated from the evolution of the hydrogen gas during the hydrogen evolution reaction (HER) reaction, which can influence the PEC performances, were effectively removed using a magnetic stirrer from the electrode surface. The photocurrents ware normalized by the actual area of each photocathode exposed under the light into the photocurrent density. The bare *p*-Si curve measured was the one without a passivation layer, and the curve was used before the gradual degradation for comparison. First, for bare *p*-Si, the saturation current is ~ 30 mA/cm^2 and the onset potential is 0.25 V vs. RHE (from now, the voltages are provided relative to RHE). Compared with the bare *p*-Si, the anodic shift of about 0.5–2 V were observed for the thin film conditions for all conditions (H5-1, H10-1, and H20-1). The enhancements are attributed to the catalytic properties of the TiO_2 layer and the slight reduction in the light reflectance by the thin film. After the synthesis of TiO_2 nanorods, the PEC performances were enhanced additionally regardless of the thickness of the seed layer. Especially, the anodic shift of the onset potential was prominent, and the saturation current also increased up to ~ 35–37.5 mA /cm^2. TiO_2 thin film and nanorods can act not only as a passivation layer and can reduce the reflection of the incident light on the *p*-Si substrate by forming the nanostructure remarkably as expected. In addition, the effect of MoS_2 decoration was also worthy of notice. The onset potentials of all samples were significantly improved after the decoration of MoS_2 nanoparticles

significantly improved. The maximum saturated current densities of H5, H10 and H20 series were 33, 34, and 38 mA/cm^2 at 0 V vs. a reference hydrogen electrode (RHE), respectively. Moreover, the higher concentration of MoS_2 precursor (0.51–1.01 mM) still exhibited catalytic effects in terms of onset potential, but a cathodic shift of about -1.0 V. It could be originated from an excessive coverage of the MoS_2, which can increase a surface resistance. The photocurrent density, and the saturation current density were summarized in Table 3.2 and were plotted in Figure 3.8. In the case of the H20 series, the effect of the MoS_2 decoration was different from that of the H5 series. The effect was not remarkable until the concentration of 0.17 mM MoS_2 precursor (H20-3-a). However, the increase in the photocurrent and onset potential for 0.51 mM MoS_2 precursor concentration (H20-3-b) was the highest. Further higher concentrations of 0.68 and 1.01 mM MoS_2 precursor, the catalytic effect and the increase in photocurrent were reduced. It can be regarded that there is the optimum condition for the MoS_2 decoration on TiO_2 nanostructures. Tafel slope is an inherent property of electrocatalytic material. It is determined by the rate-limiting step of HER. The determination and interpretation of Tafel slope are important for elucidation of the hydrogen evolution mechanism involved.[53] The Tafel line, which was commonly utilized for the assessment of the electrode performance[54] so that the HER kinetics can be estimated by the corresponding Tafel plots of these catalysts. Thus, in order to evaluate the HER kinetics, the LSV curves were converted into the Tafel slopes as shown in Figure 3.9. The Tafel slope is determined by selecting the linear interval in the LSV curves. Water reduction for the evolution of hydrogen occurs by the accepted three-step mechanism, such as, the Volmer (Tafel slope of 120 mV/dec in an acidic electrolyte), Heyrovsky (40 mV/dec), and Tafel (30 mV/dec) steps. It has been regarded that the Tafel slope of 134 mV/dec for the TiO_2 NRs/*p*-Si sample indicates the HER occurred by the Volmer reaction with this cathode structure.[55-57] The large increase in photocurrent is originated from the antireflective properties of the uniform TiO_2 NRs layer. Furthermore, MoS_2 on TiO_2 nanostructures could contribute the catalytic effect as a photocatalyst and also

act as a photoelectrode under the incident light thus probably contribute to the total current density of the photocathode. It should be noted that the enhancement features of the PEC characteristics were different from the synthesis processes: bare *p*-Si → TiO_2 thin film → TiO_2 nanorods → MoS_2 decoration. The features in behaviour of PEC performances for each condition, especially in the TiO_2 seed layer thickness, will be discussed again with the microstructure analysis and the band structure.

The electrochemical impedance spectroscopy (EIS) measurements were carried out to understand the surface kinetics during HER in the electrolyte. The impedance spectra reflect the HER activities of the photocatalysts.[58] and to evaluated the charge-transfer resistances as plotted in Figure 3.10 and 3.11. The thin film samples (H5-1, H10-1, and H20-1) showed a single semicircle in the Nyquist plot due to the negligible series resistance of the thin TiO_2 layer, even though the thickness of the samples was varied from 5–20 nm. However, two semicircles in each plot, were plotted as shown in the others, such as H10-2 and H10-3-b in Figures 3.10 and 3.11. The EIS curves were fitted to the equivalent circuit, which consist of a constant phase element (CPE) and resistances such as series resistance (R_s), charge transfer resistance from the *p*-Si to TiO_2 thin film ($R_{\_Si}$), that from the TiO_2 thin film to the TiO2 nanorods ($R_{\_thin\ film}$) and that from the TiO2 nanorods to the MoS_2 ($R_{\_NR}$), and that from the MoS2 ($R_{\_MoS2}$) to the electrolyte as shown in Figure 3.12. The charge-transfer resistances evaluated from the EIS curve fittings indicates that the charge can transfer from TiO_2 nanorods to electrolyte more comfortably when the hydrothermally synthesized MoS_2 was decorated on the surface of the TiO_2 nanorods. The charge-transfer resistance values were summarized in Table 3.3.

Incident photon to current efficiency (IPCE) values were measured by means of the way to evaluated the conversion efficiency of the absorbed photons into current as shown in Figure 3.13. The IPCE values for all the photocathodes synthesized were measured at 0V vs RHE. The IPCE of the H10-1 is ~30 % under the entire visible light region, of which the conversion efficiency is low. The IPCE of the H10-2 and H10-4, however, is significantly improved up to ~42.7 and ~79.9 %, respectively.

Thus, it can be elucidated that such an excellent enhanced IPCE is due to the effect of the antireflection of the TiO_2 nanorods, to the effective light scattering, and to the proper catalytic effect of the MoS_2.

Table 3.1 The labels of the photocathodes in this thesis, classified by the combinations of the thickness of the seed layer, structures, and MoS_2 precursor concentrations

Seed layer Thickness	Synthesis Conditions		
5 nm	TiO_2 seed layer/*p*-Si	-	**H5-1**
	TiO_2 NRs/seed layer/*p*-Si	-	**H5-2**
	MoS_2/TiO_2 NRs/seed layer/*p*-Si	0.17 mM MoS_2 precursor	**H5-3-a**
		0.51 mM MoS_2 precursor	**H5-3-b**
		0.68 mM MoS_2 precursor	**H5-3-c**
		1.01 mM MoS_2 precursor	**H5-3-d**
10 nm	TiO_2 seed layer/*p*-Si	-	**H10-1**
	TiO_2 NRs/seed layer/*p*-Si	-	**H10-2**
	MoS_2/TiO_2 NRs/seed layer/*p*-Si	0.17 mM MoS_2 precursor	**H10-3-a**
		0.51 mM MoS_2 precursor	**H10-3-b**
20 nm	TiO_2 seed layer/*p*-Si	-	**H20-1**
	TiO_2 NRs/seed layer/*p*-Si	-	**H20-2**
	MoS_2/TiO_2 NRs/seed layer/*p*-Si	0.17 mM MoS_2 precursor	**H20-3-a**
		0.51 mM MoS_2 precursor	**H20-3-b**
		0.68 mM MoS_2 precursor	**H20-3-c**
		1.01 mM MoS_2 precursor	**H20-3-d**

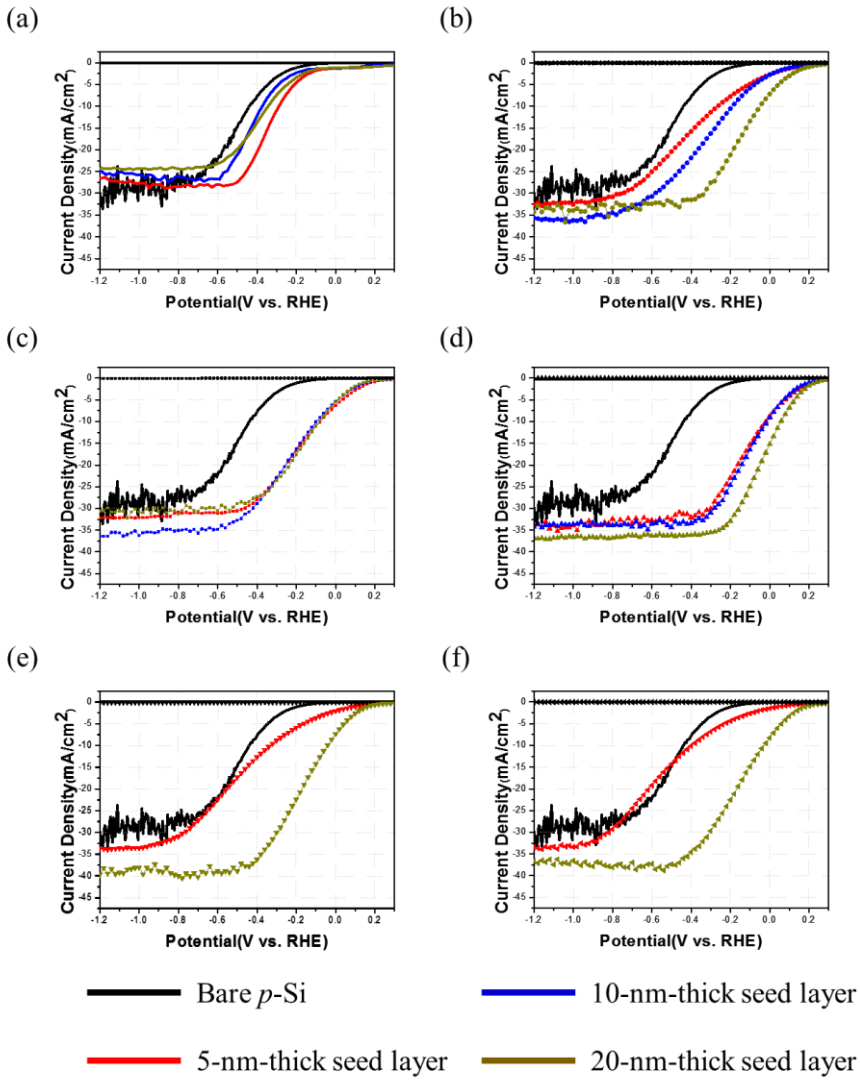

Figure 3.6 The LSV curves of the photocathodes in terms of the synthesis processes; (a) seed layer, (b) TiO_2 NRs/*p*-Si, and the MoS_2 precursor concentrations: (c) 0.17 mM, (d) 0.51 mM, (e) 0.68 mM, and (f) 1.01 mM

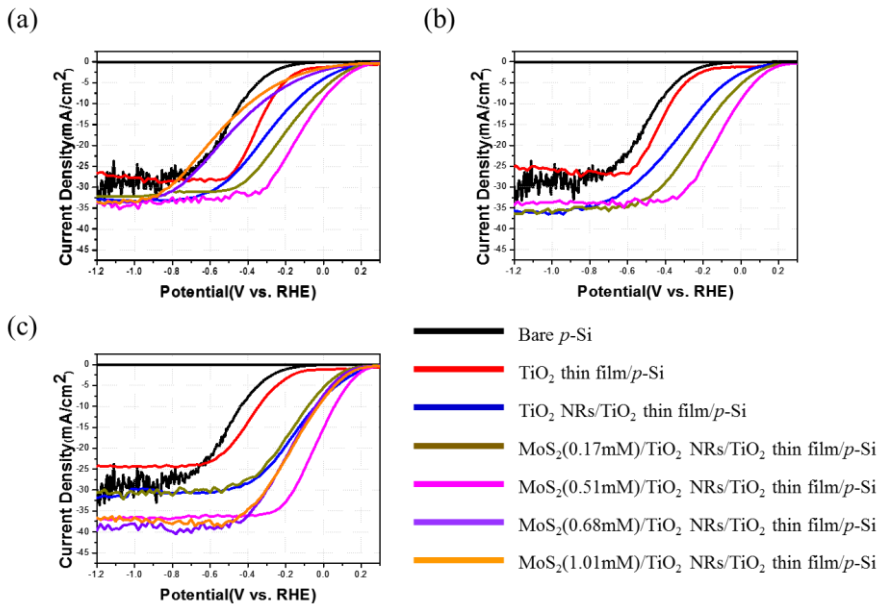

Figure 3.7 The LSV curves of the photocathodes in terms of the seed layer thickness; (a) 5 nm, (b) 10 nm, and (c) 20 nm

Table 3.2 The current density at 0 V vs. RHE and the saturation current density in terms of the seed layer thickness; (a) 5 nm, (b) 10 nm , and (c) 20 nm

(a)	Current density at 0 V vs. RHE (mA/cm^2)	Saturation current density (mA/cm^2)
H5-1	1.26	28
H5-2	3.52	32
H5-3-a	6.36	32
H5-3-b	7.68	33
H5-3-c	2.05	33
H5-3-d	1.31	33

(b)	Current density at 0 V vs. RHE (mA/cm^2)	Saturation current density (mA/cm^2)
H10-1	1.21	26
H10-2	2.76	34
H10-3-a	5.36	34
H10-3-b	9.11	34

(c)	Current density at 0 V vs. RHE (mA/cm^2)	Saturation current density (mA/cm^2)
H20-1	1.15	24
H20-2	7.92	30
H20-3-a	5.51	30
H20-3-b	15.24	36
H20-3-c	7.31	38
H20-3-d	8.26	37

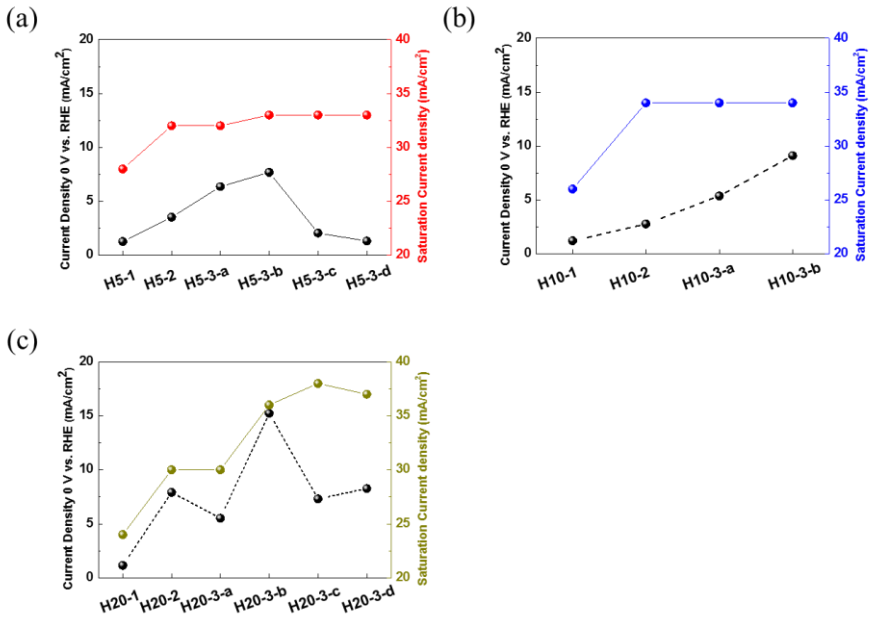

Figure 3.8 The evolution of the current density at 0 V vs. RHE and the saturation current density in terms of the seed layer thickness; (a) 5 nm, (b) 10 nm , and (c) 20 nm

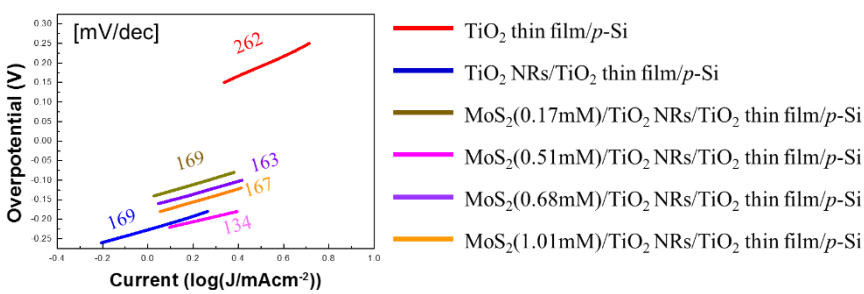

Figure 3.9 The Tafel slopes of the TiO_2 thin film/*p*-Si, TiO_2 NRs/TiO_2 thin film/*p*-Si, and MoS_2/TiO_2 thin film/TiO_2 NRs/*p*-Si

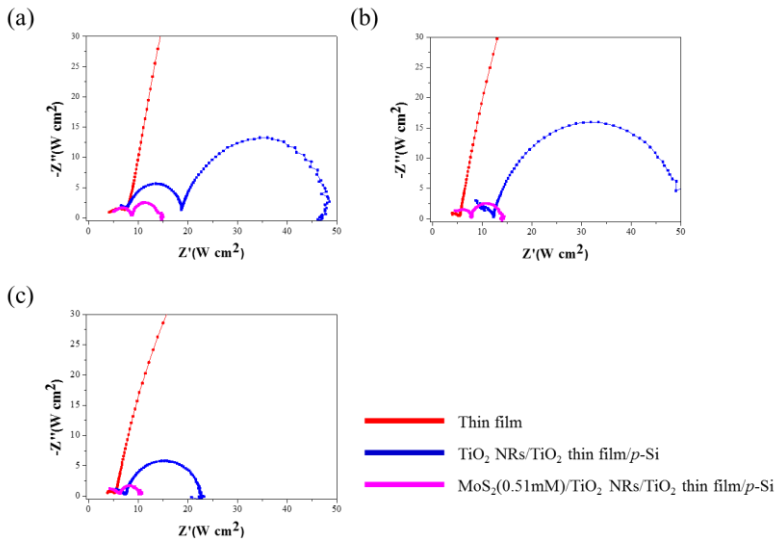

Figure 3.10 The Nyquist impedance plots for TiO_2 thin film/*p*-Si, TiO_2 NRs/TiO_2 thin film/*p*-Si, and MoS_2/TiO_2 NRs/TiO_2 thin film/*p*-Si; (a) 5-nm-thick seed layer, (b) 10-nm-thick seed layer, and (c) 20-nm-thick seed layer

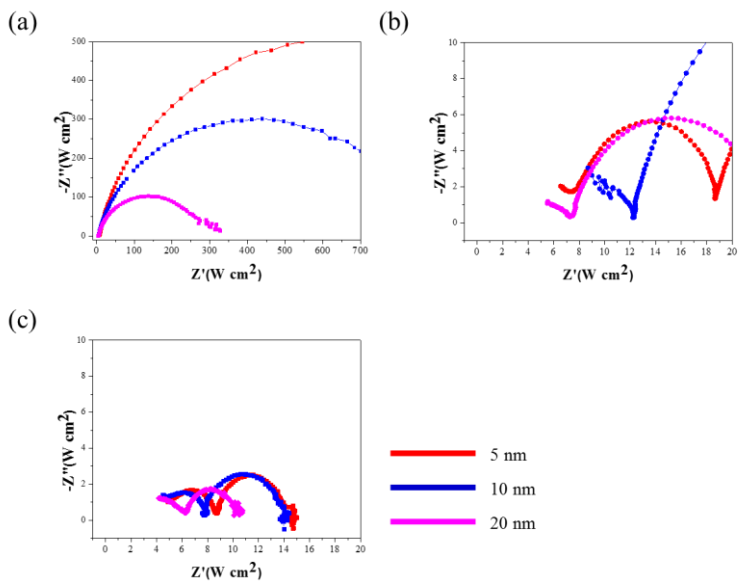

Figure 3.11 The Nyquist impedance plots for (a) TiO_2 thin film/*p*-Si, (b) TiO_2 NRs/TiO_2 thin film/*p*-Si, and (c) MoS_2 (0.51 mM)/TiO_2 NRs/TiO_2 thin film/*p*-Si

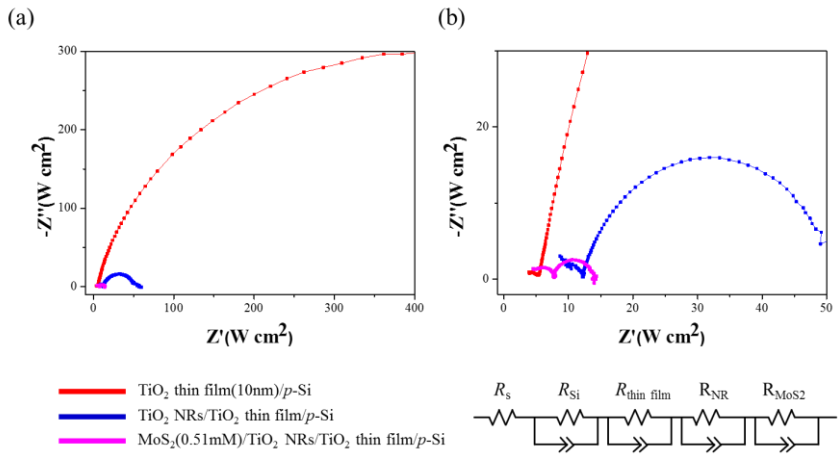

Figure 3.12 (a) the Nyquist impedance plots of TiO_2 thin film/*p*-Si, TiO2 NRs/TiO_2 thin film/*p*-Si, and MoS_2(0.51 mM)/TiO_2 NRs/TiO_2 thin film/*p*-Si, (b) enlarged scale of (a) and its equivalent circuit

Table 3.3 The charge-transfer resistances of the photocathodes

Seed layer Thickness	Synthesis Conditions	R1(+)	R2(+)	R3(+)	R4(+)
H5-1	TiO_2 seed layer/*p*-Si	2.642753	5.532513	1136.668	-
H5-2	TiO_2 NRs/seed layer/*p*-Si	7.524779	11.28648	31.24428	
H5-3-b	MoS_2/TiO_2 NRs/seed layer/*p*-Si	4.440354	4.373032	4.506714	1.091575
H10-1	TiO_2 seed layer/*p*-Si	2.816672	2.591183	730.2261	-
H10-2	TiO_2 NRs/seed layer/*p*-Si	8.632998	3.656403	38.38595	
H10-3-b	MoS_2/TiO_2 NRs/seed layer/*p*-Si	4.246597	3.458692	5.678978	0.483105
H20-1	TiO_2 seed layer/*p*-Si	2.327393	3.177038	266.0313	-
H20-2	TiO_2 NRs/seed layer/*p*-Si	7.080296	1.100367	15.07444	
H20-3-b	MoS_2/TiO_2 NRs/seed layer/*p*-Si	2.073226	4.113184	4.098062	0.131682

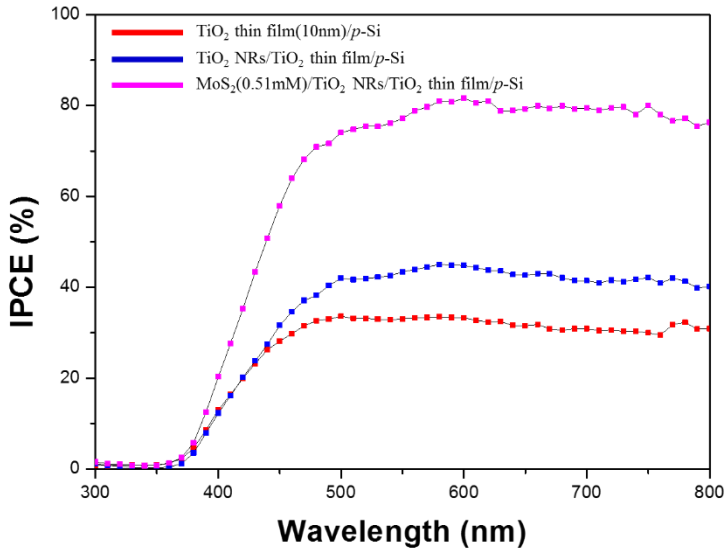

Figure 3.13 The incident photon to current conversion efficiency (IPCE) of TiO_2 thin film/*p*-Si, TiO_2 NRs/TiO_2 thin film/*p*-Si and MoS_2/TiO_2 NRs/TiO_2 thin film/*p*-Si

3.3.3 Microstructure analysis on the 2D-MoS_2/TiO_2 heterostructure

The surface morphology confirmed by STEM as shown in Figure 3.5 could confirm the shape of TiO_2 nanorods, but trace MoS_2 was difficult to identify. Transmission electron microscope (TEM) analysis were performed for the structural analysis of MoS_2, of which exhibits the 2D characteristic, and for the interface analysis with TiO_2 nanorods. Figure 3.14 is a cross-sectional TEM image of MoS_2/TiO_2 nanorods on *p*-Si decorated with hydrothermally synthesized MoS_2 (H10-3-b). The high resolution image (HR image) at the TiO_2 nanorods grown by hydrothermal synthesis and the Fast Fourier transformation (FFT) from the HR images are identified to the rutile single phase. In other words, it was confirmed by the fact that the lattice fringes were well aligned in the HR image, and the interplanar distance of 0.309 nm and the interplanar distance of 0.326 nm were measured in the FFT shown in the inset of

Figure 3.14 (b), which were identified to the $(1\bar{1}0)_{rutile}$ and $(001)_{rutile}$, respectively. As confirmed by SEM analysis in Figure 3.4 and STEM analysis in Figure 3.5, the morphology of hydrothermally synthesized TiO_2 nanorods with respect to the thickness of each seed layer shows different characteristics, in terms of the dimensions as well as the areal density of the nanorods. In order to confirm the presence of MoS_2, the elemental distributions were examined by the scanning transmission electron microscope-energy dispersive spectroscopy (STEM-EDS). As shown in Figure 3.15, the elemental distributions revealed that the presence of Ti, O, Mo, and S without any unexpected elements. However, since the molarity of the MoS_2 precursor (0.17–1.01 mM) is low, the low intensity of the Mo in the elemental mapping can be explained. The MoS_2 particles can be attached onto the surface of the TiO_2 nanorods. Therefore, the spectrum from the scanning area acquired during the elemental mapping was analyzed. The presence of Mo Lα1 peak and S Kα1 peak within the EDS spectrum can be clearly seen in the inset, which is an enlarged view of the part shown in Figure 3.15 (b). In this study, the hydrothermally decorated MoS_2 is introduced to obtain the catalytic effect and the HER performance itself. Therefore, the morphology of MoS_2 is important for the decoration of the thin layered MoS_2 with 2D-structure on the surface of TiO_2 nanorod, which can be obtained mainly by the chemical vapor deposition (CVD) and/or metal organic CVD (MOCVD). The typical morphology of the MoS_2 synthesized by the hydrothermal synthesis[59-61] is a spherical form including many edge sites as shown in Figure 3.16. As shown in the Figure 3.17, even though the morphology of MoS_2 grown on TiO_2 nanorods, which are synthesized on FTO by hydrothermal method, is similar to the morphologies in Figure 3.16, however it is definitely distinguished from that in this thesis. This is because the concentration of MoS_2 precursor is much higher than that of the present thesis (about 10 times or more). Thus, the size of the MoS_2 particles are large and thick enough of a few μm scale, even though the synthesis conditions are similar except the precursor concentration. In addition, at the interface between

the MoS_2 and the TiO_2 nanorods, the MoS_2 are stacked along the direction of the basal plane normal, which are thermodynamically preferred, on the surface of the TiO_2 rod to form a layered structure, and finally the entire rods were covered with the MoS_2 sheets and then were started to form a structure of vertically aligned and connected to each other.

Figure 3.18 (b) shows the HR image of the surface of the TiO_2 nanorod. In the area marked in red. The surface of the nanorod with very clean rutile TiO_2 surface was observed without any defect. However, a faint lattice fringes were observed as shown in the area marked in green in Figure 3.18 (d) and Figure 3.18 (e). In this region a MoS_2 sheet of about 5 nm in size was identified by the FFT analysis of the lattice fringe (Figure 3.18 (f)). Furthermore, it was clearly confirmed that the 2D structure MoS_2 was synthesized properly by observation with various angles. The decoration of 2D-MoS_2 can be influenced by the surface morphology of the nanostructures. It can be more advantageous to decorate the MoS_2 catalysts when as much surface area of the nanorods is exposed even in the solutions. In the case of the H20-3, the decoration effect of MoS_2 was negligible while the enhancement is significantly achieved in the H5-3 and H10-3 in Fig. However, H20-4 showed a large increase in photocurrent density as well as catalytic effect, even though the saturation photocurrent density is maintained for the H5-4 and H10-4, where the concentration of the MoS_2 precursor are identical. The density of the TiO_2 nanorods were smaller than the other two conditions (H5, H10), so that the TiO_2 thin film was much more exposed. Therefore, it can be elucidated that the higher concentration should be required to exhibit the catalytic effect. Figure 3.19 displays the presence of 2D-MoS_2 on the faceted TiO_2 thin film (H20-4). Furthermore, the interesting feature for PEC performance is the large enhancement of the PEC performance for the H20 series. The reason can be elucidated by TEM analysis after hydrothermal synthesis. Figure 3.19 (a) shows the cross-sectional TEM image of the H20-2 specimen. The coverage of the nanorods is much lower. In fact, the regions without nanorods have formed ~ 32 nm thick TiO_2 films with various facets. This thickness was about 50% greater

than the thickness deposited by the e-beam evaporator. The faceted TiO_2 film is well crystallized by heat treatment after the synthesis of the nanorods, resulting in the roughness of the surface, which can more effectively block the reflection from *p*-Si. Hence, it can be explained that the roughness of the thin film surface can contribute to the improvement of PEC characteristics.

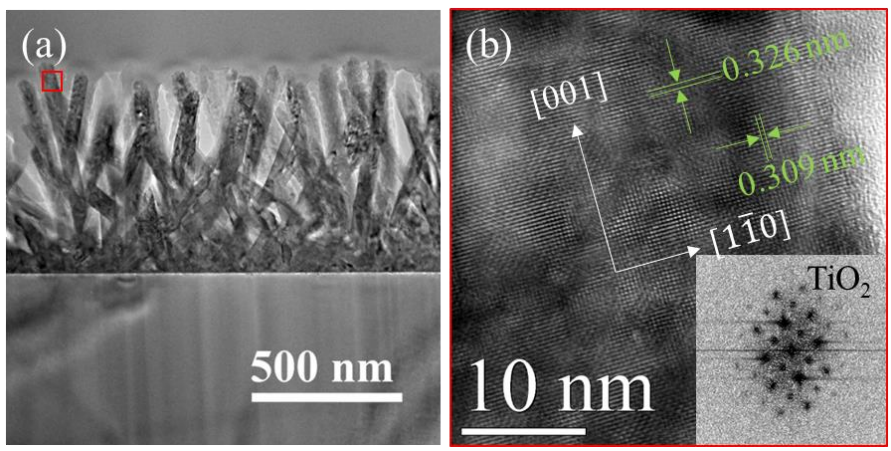

Figure 3.14 (a) cross-sectional TEM image of TiO2 NRs/*p*-Si, (b) high resolution TEM image of the TiO_2 nanorod from marked in red in (a) and its FFT (inset)

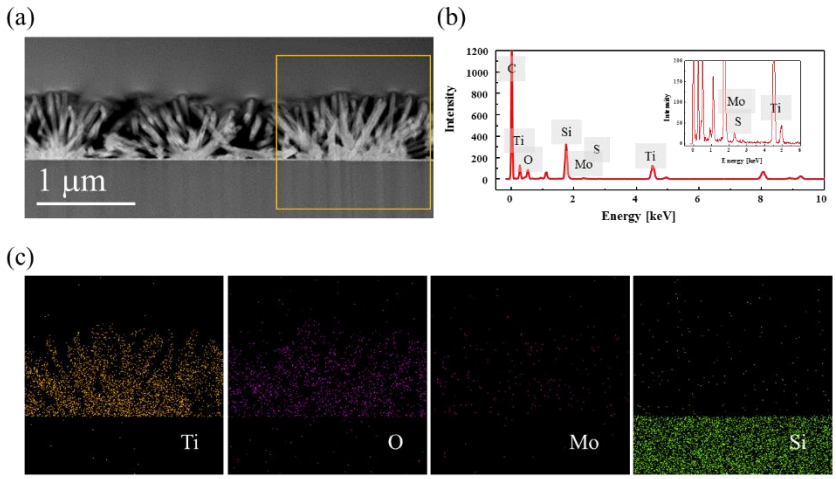

Figure 3.15 (a) cross-sectional STEM image of TiO_2 NRs/*p*-Si, (b) the EDS spectrum collected from the region marked in (a), and (c) the EDS elemental mapping results

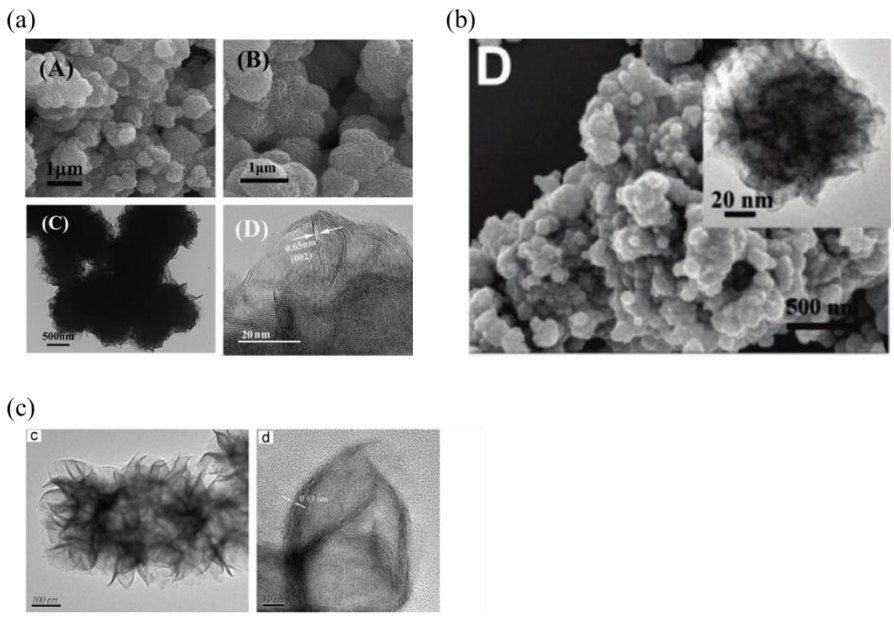

Figure 3.16 The typical morphologies of the hydrothermally grown MoS_2 from the other reports (a) Ma et al.[59], (b) Li et al.[60], and (c) Tang et al.[61]

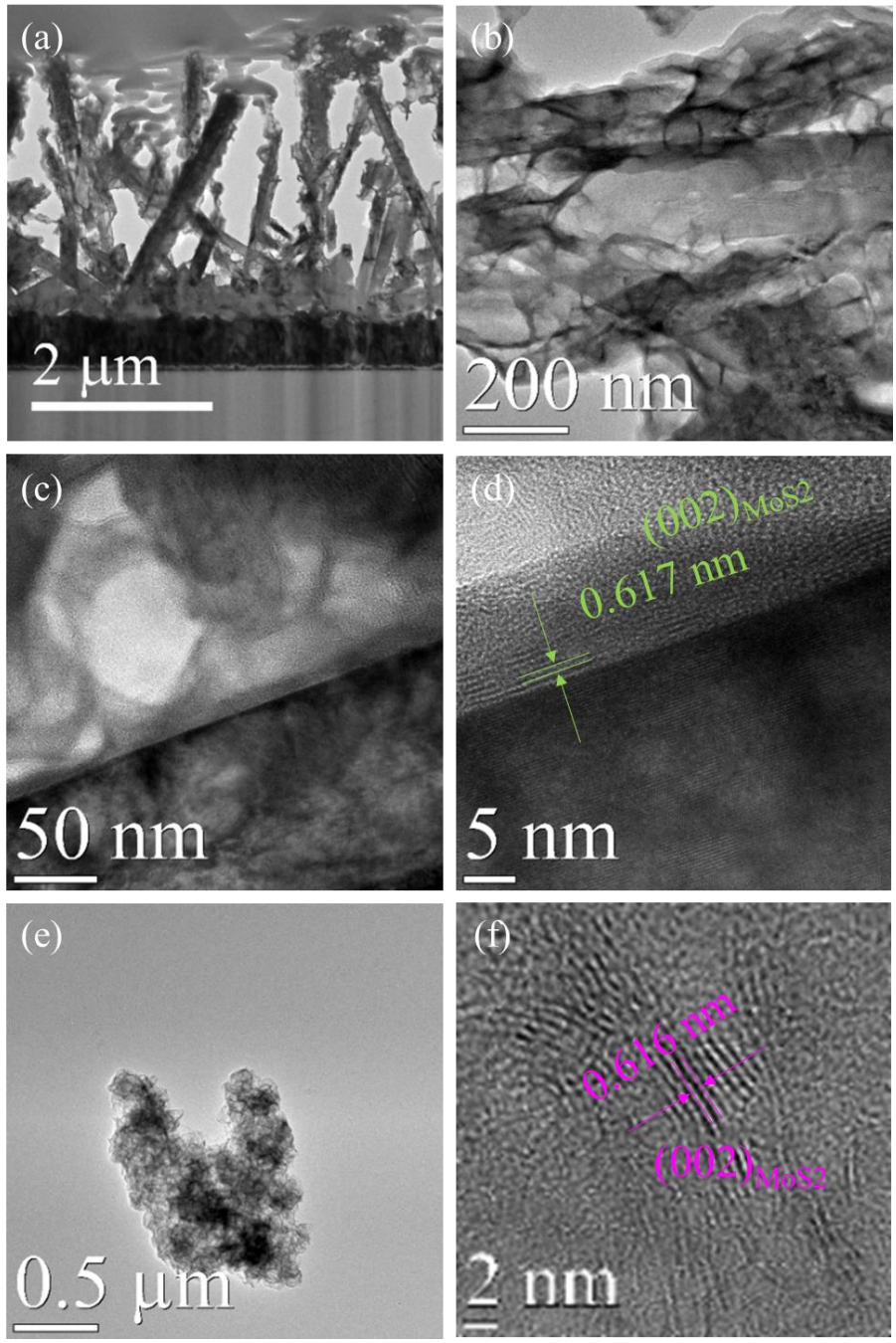

Figure 3.17 (a) low magnification TEM image of the hydrothermally grown MoS_2 on TiO_2 nanorods, (b) high magnification of (a), (c) high resolution image of the interface between MoS_2 and TiO_2, (d) layered structure of the MoS_2 on TiO_2 nanorods, (e) the morphology of a MoS_2 particle, and (f) interplanar spacing of MoS_2 from (e)

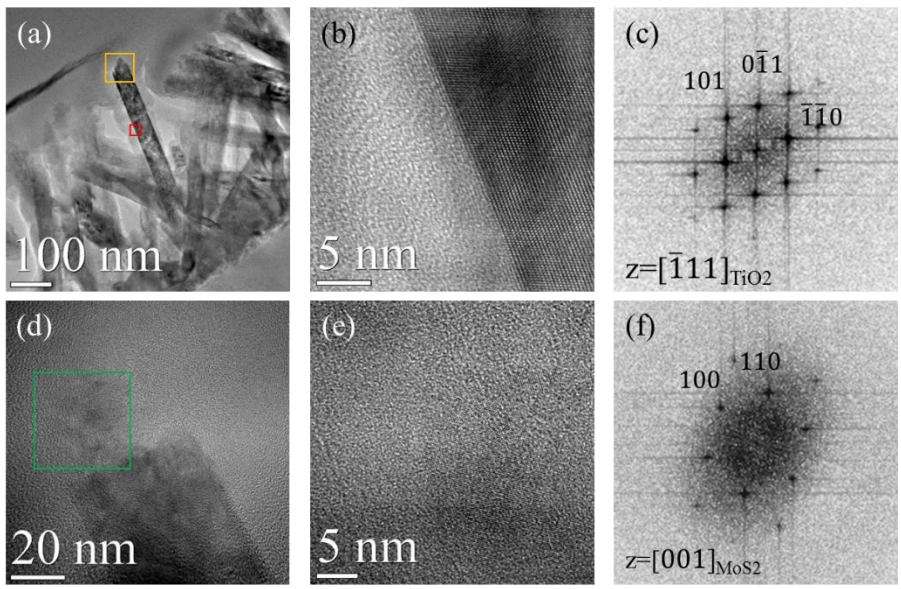

Figure 3.18 (a) low magnification TEM image of MoS_2/TiO_2 NRs heterostructure, (b) high resolution image of a TiO_2 nanorod and (c) its FFT from marked in red in (a), high magnification TEM image of a MoS_2/TiO_2 heterostructure from marked in orange in (a), (e) high resolution image of a MoS_2 and (f) its FFT from marked in green in (d)

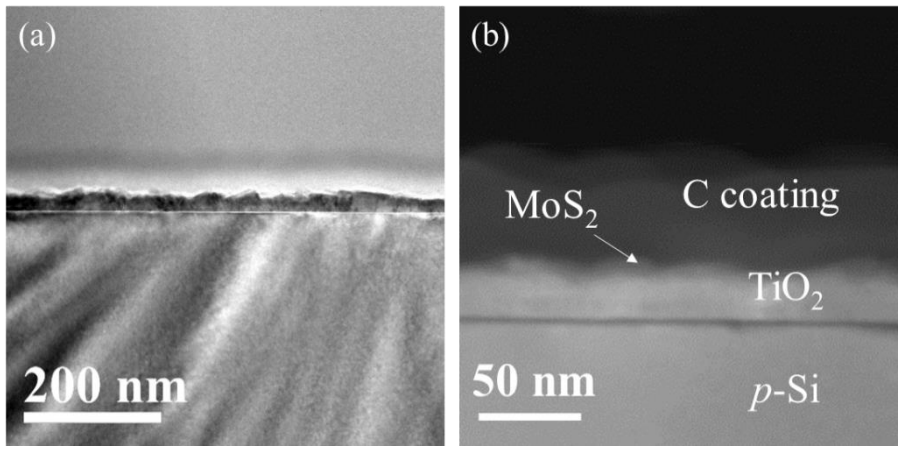

Figure 3.19 (a) cross-sectional TEM image of the thin film region after the TiO_2 hydrothermal process, (b) high magnification STEM image of (a)

3.3.4 Band Alignments of the MoS_2/TiO_2 Heterostructure

The photogenerated electrons in *p*-Si should be efficiently transported to the electrolyte interface via the MoS_2/TiO_2 heterostructure for HER. In the thermodynamical point of view, the band-bending in the $MoS_2/TiO_2/p$-Si heterostructure was investigated to gain insight of the electronic structures of the MoS_2/TiO_2/p-Si heterostructure using X-ray photoelectron spectroscopy (XPS) and ultraviolet photoemission spectroscopy (UPS). Figure 3.20 shows the high resolution XPS spectra of Ti, O, Mo and S. The peaks in Figure 3.20 (c) were identified to Mo^{4+} $3d_{5/2}$ (230.95 eV), Mo^{5+} $3d_{5/2}$(232.68 eV), Mo^{4+} $3d_{3/2}$ (234.26 eV), and Mo^{5+} $3d_{3/2}$ (235.85 eV), respectively. The peak in Figure 3.20 (c) at 226.46 eV was corresponds to S 2*s*.[62, 63] The high resolution XPS spectrum of S in Figure 3.20 (d) were composed of the components corresponding to S $2P_{3/2}$ (162.22 eV) and S $2P_{1/2}$(163.40 eV), respectively. these peaks are broadened, and shift towards the lower binding energy. The broadened peaks indicate that a variety of molybdenum oxides and sulphides exist in the hydrothermal product in addition to MoS_2.[64] In addition, the shift of the

peaks could be attributed to the heterostructure effect between the TiO_2 nanorods and MoS_2.[65-67]

The work function can be calculated from the difference between the cutoff of the highest binding energy and the photon energy of the exciting radiation.[68] After synthesizing TiO_2 nanorods on *p*-Si, the work function of the *p*-Si surface has decreased from 4.9 to 4.6 eV. Finally, the work function of the MoS_2/TiO_2 NRs/p-s- were reduced to 4.4 eV as shown in Figure 3.21 (a). The energy difference between the Fermi level and valence band maximum is increased from 0.4 to 1.1 eV. Furthermore, the work function has further decreased to 4.4 eV after the decoration by the hydrothermally synthesized MoS_2 as displayed in Figure 3.21 (b). The energy difference between the Fermi level and valence band maximum is increased, where the values are 0.4 eV for the *p*-Si, 1.4 eV for the TiO_2 NRs/*p*-Si, and 2.9 eV for the MoS_2/TiO_2 NRs/*p*-Si, respectively, indicating the formation of the heterostructure properly so that the electrons can be effectively transferred. The work functions and energy differences between the Fermi level and valence band maximum are described in Figure 3.21 (c) and (d).

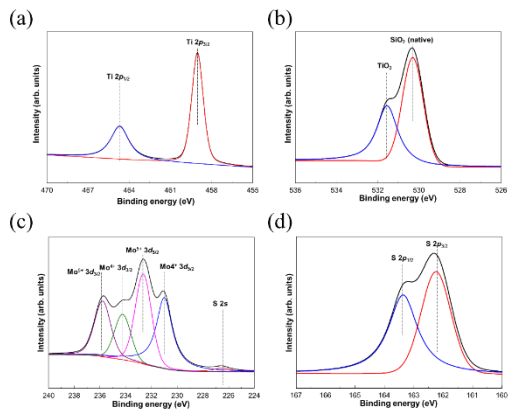

Figure 3.20 The high resolution XPS spectra of (a) Ti, (b) O, (c) Mo and (d) S obtained from the MoS_2/TiO_2 NRs/TiO_2 thin film/*p*-Si

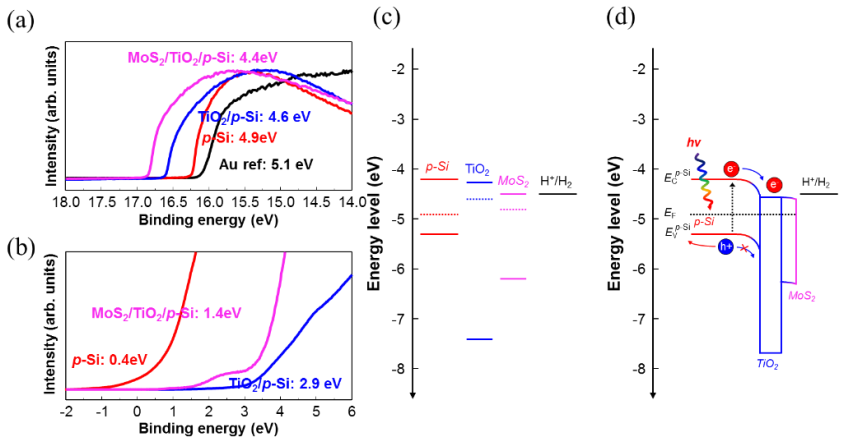

Figure 3.21 (a) UPS spectra of *p*-Si, TiO_2 NRs/TiO_2 thin film/*p*-Si, MoS_2/TiO_2 NRs/TiO_2 thin film/*p*-Si, and reference Au foil. (b) the energy difference between the Fermi level and valence band maximum, (c) the band gap energy of the *p*-Si, TiO_2, and MoS_2 calculated the UPS analysis, (d) Schematic of energy band diagram of the MoS_2/TiO_2/*p*-Si heterojunction photocathode

3.4 Summary

PEC characteristics using a *p*-type Si as a photocathode were measured. The TiO_2 thin films were introduced for a passivation layer of the *p*-Si, where the thicknesses were varied from 5 nm to 20 nm. Moreover, the TiO_2 nanorods were grown on the substrates synthesized by the hydrothermal method to enhance the catalytic effect and to reduce the reflection. Furthermore, as a photocatalyst, the decoration of 2D-MoS_2 increased the photocurrent with decreasing the overpotential remarkably. In detail, in order to achieve high PEC performance, the TiO_2 nanorods were hydrothermally synthesized on the *p*-Si substrates. In this study, the surface morphology can be controlled by varying the thickness of the seed layer., which also affected the PEC characteristics. In terms of surface morphology of the TiO2 nanorods, the PEC performance of H10-2 (10-nm-thick seed layer) is higher than that of the H5-2 (5-nm-thick seed layer) because the light scattering and reflection were reduce, which were originated from the flower-like shape of the nanorods in H10-2. Even though the density of the nanorods were significantly low, the PEC performance was highest in the H20-2. Those highest PEC performances might be achieved by the rough surface of the thin film. Moreover, the additional enhancement was obtained by decoration with 2D-MoS_2, which was confirmed by TEM and XPS analysis, on the surface of the TiO_2 nanorods. By introducing the 2D-MoS_2 as a catalyst, the PEC performance, not only overpotential but also photocurrent, was remarkably enhanced. Thus, it can be elucidated that the Hydrothermally synthesized MoS2 acts as a photocatalyst properly, such as the charge-transfer resistance was reduced and the IPCE was increased. By investigating the work function of the $MoS_2/TiO_2/p$-Si photocathode, the formation of the heterostructure between MoS2 and TiO2 was confirmed, where the electrons can be effectively transferred.

3.5 References

1. M. Gratzel, *Nature*, 2001, **414**, 338-344.
2. A. Fujishima and K. Honda, *Nature*, 1972, **238**, 37.
3. M. J. Choi, J. Y. Jung, M. J. Park, J. W. Song, J. H. Lee and J. H. Bang, *Journal of Materials Chemistry A*, 2014, **2**, 2928-2933.
4. Z. Chen, H. N. Dinh and E. Miller, *Photoelectrochemical Water Splitting: Standards, Experimental Methods, and Protocols*, Springer New York, 2013.
5. S. Hu, M. R. Shaner, J. A. Beardslee, M. Lichterman, B. S. Brunschwig and N. S. Lewis, *Science*, 2014, **344**, 1005-1009.
6. B. Seger, T. Pedersen, A. B. Laursen, P. C. Vesborg, O. Hansen and I. Chorkendorff, *J Am Chem Soc*, 2013, **135**, 1057-1064.
7. D. M. Andoshe, J. M. Jeon, S. Y. Kim and H. W. Jang, *Electronic Materials Letters*, 2015, **11**, 323-335.
8. Y. J. Lin, R. Kapadia, J. H. Yang, M. Zheng, K. Chen, M. Hettick, X. T. Yin, C. Battaglia, I. D. Sharp, J. W. Ager and A. Javey, *J Phys Chem C*, 2015, **119**, 2308-2313.
9. M. Caban-Acevedo, M. L. Stone, J. R. Schmidt, J. G. Thomas, Q. Ding, H. C. Chang, M. L. Tsai, J. H. He and S. Jin, *Nature Materials*, 2015, **14**, 1245-1251.
10. M. A. Lukowski, A. S. Daniel, F. Meng, A. Forticaux, L. Li and S. Jin, *J Am Chem Soc*, 2013, **135**, 10274-10277.
11. H. Kim, J. Park, I. Park, K. Jin, S. E. Jerng, S. H. Kim, K. T. Nam and K. Kang, *Nat Commun*, 2015, **6**.
12. S. M. Sze and K. K. Ng, *Physics of Semiconductor Devices*, Wiley, 2006.
13. Z. Zongyan, L. Zhaosheng and Z. Zhigang, *Journal of Physics: Condensed Matter*, 2010, **22**, 175008.

14. A. Azarpira, M. Lublow, A. Steigert, P. Bogdanoff, D. Greiner, C. A. Kaufmann, M. Krüger, U. Gernert, R. van de Krol, A. Fischer and T. Schedel-Niedrig, *Advanced Energy Materials*, 2015, **5**, 1402148.
15. D. M. Andoshe, S. Choi, Y.-S. Shim, S. H. Lee, Y. Kim, C. W. Moon, D. H. Kim, S. Y. Lee, T. Kim, H. K. Park, M. G. Lee, J.-M. Jeon, K. T. Nam, M. Kim, J. K. Kim, J. Oh and H. W. Jang, *Journal of Materials Chemistry A*, 2016, **4**, 9477-9485.
16. Q. Liu, Z. Pu, A. M. Asiri, A. H. Qusti, A. O. Al-Youbi and X. Sun, *Journal of Nanoparticle Research*, 2013, **15**.
17. J. G. Yu, L. F. Qi and M. Jaroniec, *J Phys Chem C*, 2010, **114**, 13118-13125.
18. J. Yu, J. Zhang and M. Jaroniec, *Green Chemistry*, 2010, **12**, 1611.
19. K. Maeda, A. Xiong, T. Yoshinaga, T. Ikeda, N. Sakamoto, T. Hisatomi, M. Takashima, D. Lu, M. Kanehara, T. Setoyama, T. Teranishi and K. Domen, *Angew Chem Int Ed Engl*, 2010, **49**, 4096-4099.
20. J.-J. Chen, J. C. S. Wu, P. C. Wu and D. P. Tsai, *J Phys Chem C*, 2011, **115**.
21. Z. Chen, D. Cummins, B. N. Reinecke, E. Clark, M. K. Sunkara and T. F. Jaramillo, *Nano Lett*, 2011, **11**, 4168-4175.
22. K. Maeda, N. Saito, Y. Inoue and K. Domen, *Chemistry of Materials*, 2007, **19**, 4092-4097.
23. B. Han and Y. H. Hu, *Energy Science & Engineering*, 2016, **4**, 285-304.
24. X. Fan, P. Xu, D. Zhou, Y. Sun, Y. C. Li, M. A. Nguyen, M. Terrones and T. E. Mallouk, *Nano Lett*, 2015, **15**, 5956-5960.
25. X. Zong, H. Yan, G. Wu, G. Ma, F. Wen, L. Wang and C. Li, *J Am Chem Soc*, 2008, **130**, 7176-7177.
26. X. Ren, X. Qi, Y. Shen, S. Xiao, G. Xu, Z. Zhang, Z. Huang and J. Zhong, *Journal of Physics D: Applied Physics*, 2016, **49**, 315304.
27. S. Bai, L. Wang, X. Chen, J. Du and Y. Xiong, *Nano Research*, 2015, **8**, 175-183.

28. C. V. Ramana, U. Becker, V. Shutthanandan and C. M. Julien, *Geochem Trans*, 2008, **9**, 8.
29. D. J. Late, B. Liu, H. S. Matte, V. P. Dravid and C. N. Rao, *ACS Nano*, 2012, **6**, 5635-5641.
30. M. Daage and R. R. Chianelli, *Journal of Catalysis*, 1994, **149**, 414-427.
31. W. O. Winer, *WEAR*, 1967, **10**.
32. A. R. Beal, J. C. Knight and W. Y. Liang, *Journal of Physics C: Solid State Physics*, 1972, **5**.
33. A. Kuc, in *Chemical Modelling: Volume 11*, The Royal Society of Chemistry, 2015, vol. 11, pp. 1-29.
34. D. Yang, S. J. Sandoval, W. M. R. Divigalpitiya, J. C. Irwin and R. F. Frindt, *Physical Review B*, 1991, **43**, 12053-12056.
35. S. N. Shirodkar and U. V. Waghmare, *Phys Rev Lett*, 2014, **112**, 157601.
36. M. Acerce, D. Voiry and M. Chhowalla, *Nature Nanotechnology*, 2015, **10**, 313.
37. P. Cheng, K. Sun and Y. H. Hu, *Nano Lett*, 2016, **16**, 572-576.
38. P. F. Cheng, K. Sun and Y. H. Hu, *Rsc Advances*, 2016, **6**, 65691-65697.
39. E. S. Kadantsev and P. Hawrylak, *Solid State Communications*, 2012, **152**, 909-913.
40. H. S. Lee, S. W. Min, Y. G. Chang, M. K. Park, T. Nam, H. Kim, J. H. Kim, S. Ryu and S. Im, *Nano Lett*, 2012, **12**, 3695-3700.
41. K. F. Mak, C. Lee, J. Hone, J. Shan and T. F. Heinz, *Phys Rev Lett*, 2010, **105**, 136805.
42. C. Lee, H. Yan, L. E. Brus, T. F. Heinz, J. Hone and S. Ryu, *ACS Nano*, 2010, **4**, 2695-2700.
43. F. A. Frame and F. E. Osterloh, *J Phys Chem C*, 2010, **114**, 10628-10633.
44. X. Zong, Y. Na, F. Wen, G. Ma, J. Yang, D. Wang, Y. Ma, M. Wang, L. Sun and C. Li, *Chem Commun (Camb)*, 2009, DOI: 10.1039/b907307h, 4536-4538.

45. T. F. Jaramillo, K. P. Jorgensen, J. Bonde, J. H. Nielsen, S. Horch and I. Chorkendorff, *Science*, 2007, **317**, 100-102.

46. H. Tributsch and J. C. Bennett, *J. Electroanal. Chem.*, 1977, **81**.

47. A. B. Anderson and Z. Y. Al-Saigh, *J. Phys. Chem.*, 1988, **92**.

48. L. S. Byskova, M. Bollinger, J. K. Nørskova, B. S. Clausenb and H. Topsøe, *Journal of Molecular Catalysis A: Chemical*, 2000, **163**.

49. J. D. Benck, T. R. Hellstern, J. Kibsgaard, P. Chakthranont and T. F. Jaramillo, *Acs Catalysis*, 2014, **4**, 3957-3971.

50. S. S. Mali, J. V. Patil, P. M. Kadam, H. P. Deshamukh, C. S. Shim, P. S. Patil and C. K. Hong, *Journal of Nanoparticle Research*, 2014, **16**.

51. A. B. Laursen, S. Kegnæs, S. Dahl and I. Chorkendorff, *Energy & Environmental Science*, 2012, **5**, 5577.

52. C. C. Weng, K. F. Hsu and K. H. Wei, *Chemistry of Materials*, 2004, **16**, 4080-4086.

53. Y. Liu, H. Yu, X. Quan, S. Chen, H. Zhao and Y. Zhang, *Sci Rep*, 2014, **4**, 6843.

54. Y. H. Fang and Z. P. Liu, *J Am Chem Soc*, 2010, **132**, 18214-18222.

55. S. A. Vilekar, I. Fishtik and R. Datta, *Journal of the Electrochemical Society*, 2010, **157**, B1040-B1050.

56. E. Skulason, V. Tripkovic, M. E. Bjorketun, S. Gudmundsdottir, G. Karlberg, J. Rossmeisl, T. Bligaard, H. Jonsson and J. K. Norskov, *The Journal of Physical Chemistry C*, 2010, **114**.

57. J. Benson, M. Li, S. Wang, P. Wang and P. Papakonstantinou, *ACS applied materials & interfaces*, 2015, **7**, 14113-14122.

58. W. G. Yang, F. R. Wan, Y. L. Wang and C. H. Jiang, *Applied Physics Letters*, 2009, **95**, 133121.

59. L. Ma, L. M. Xu, X. P. Zhou and X. Y. Xu, *Materials Letters*, 2014, **132**, 291-294.

60. Y. Li, H. Wang, L. Xie, Y. Liang, G. Hong and H. Dai, *J Am Chem Soc*, 2011, **133**, 7296-7299.

61. G. G. Tang, J. R. Sun, C. Wei, K. Q. Wu, X. R. Ji, S. S. Liu, H. Tang and C. S. Li, *Materials Letters*, 2012, **86**, 9-12.

62. P. Qin, G. Fang, W. Ke, F. Cheng, Q. Zheng, J. Wan, H. Lei and X. Zhao, *Journal of Materials Chemistry A*, 2014, **2**, 2742.

63. X. Yang, W. F. Fu, W. Q. Liu, J. H. Hong, Y. Cai, C. H. Jin, M. S. Xu, H. B. Wang, D. R. Yang and H. Z. Chen, *Journal of Materials Chemistry A*, 2014, **2**, 7727-7733.

64. X. D. Li, W. Li, M. C. Li, P. Cui, D. H. Chen, T. Gengenbach, L. H. Chu, H. Y. Liu and G. S. Song, *Journal of Materials Chemistry A*, 2015, **3**, 2762-2769.

65. W. Zhou, Z. Yin, Y. Du, X. Huang, Z. Zeng, Z. Fan, H. Liu, J. Wang and H. Zhang, *Small*, 2013, **9**, 140-147.

66. H. W. Wang, P. Skeldon and G. E. Thompson, *Surf Coat Tech*, 1997, **91**, 200-207.

67. M. Mao, L. Mei, D. Guo, L. Wu, D. Zhang, Q. Li and T. Wang, *Nanoscale*, 2014, **6**, 12350-12353.

68. M. L. Tsai, S. H. Su, J. K. Chang, D. S. Tsai, C. H. Chen, C. I. Wu, L. J. Li, L. J. Chen and J. H. He, *ACS Nano*, 2014, **8**, 8317-8322.

Conclusions

The TiO_2 nanorods were synthesized by the hydrothermal methods on the various substrates, such as the FTO, the single crystal TiO_2 substrates, and *p*-Si substrates, respectively for the solar water splitting applications. From the synthesis with the various synthesizing parameters, such as the reaction temperature and time, the concentration of the precursor and HCl, on the FTO, where the lattice mismatch is negligible compared to the TiO_2, on the TiO_2 single crystals, on *p*-Si with TiO_2 seed layer, the growth mechanism of the hydrothermally synthesized TiO_2 nanorods was proposed. The process was determined by the surface energy of TiO_2 and the solution chemistry. In the thermodynamic point of view, the surface energy of the rutile TiO_2 {110} is lowest where as that of TiO_2 {001} is highest. Therefore, the hexahedron with the four {110} planes as side-walls and grown along the [001] direction (the rod shape) is the most stable morphology. Furthermore, in the perspective of the solution chemistry, the increase in synthesis temperature and time, both the longitudinal and lateral growth of nanorods are accelerated because the reaction kinetic can be accelerated. In addition, since the increase of the precursor concentration indicates the increase of the amount of the Ti source in the solution, the growth of the nanorods is promoted besides the increase of the nucleation sites. Finally, the HCl concentration can be regarded as the most dominant factor to control the morphology of the TiO_2 nanorods. In other words, both the surface energy of TiO_2 and the solution chemistry are significantly influenced by the HCl concentration of the solution. Even though the kinetics of the overall growth process is suppressed with the HCl concentration due to the restriction of the hydrolysis of the Ti precursor, the Cl^- ions in the solution selectively were adsorbed on the {110} plane of TiO_2 to inhibit further growth of the {110} plane. Therefore, during the growth progress, the developing the {110} planes are stabilized and the rods shape were generated, resulting in the preferential growth along the [001] direction.

Despite the superior hydrogen revolution reaction (HER) performances, the *p*-Si exhibits the advantages of the photocorrosion and the high reflectance. In order to solve the drawbacks of the p-Si as a photocathode, the hydrothermally synthesized TiO_2 nanorods were introduced. The deposition of the TiO_2 seed layer alone has inhibited the photocorrosion and increased photoelectrochemical (PEC) properties. Moreover, due to the effects of the passivation and antireflection, an additional enhancement of the PEC performances was achieved by the TiO_2 nanorods grown on *p*-Si. In addition, the decoration of the 2D-MoS_2 as a photocatalyst has improved the photocurrent and overpotential significantly. From the HR-TEM, FFT, and XPS analyses, the hydrothermally grown MoS_2 on TiO_2 nanorods was confirmed. Furthermore, the formation of the MoS_2/TiO_2 heterojunction was revealed by the UPS analysis, where the band alignment has been considered. Hence, the remarkable enhancement of the PEC performances in 2D-MoS_2/TiO_2 nanorods/p-Si was achieved.

The superior PEC performances of the MoS_2/TiO_2/*p*-Si photocathode were accomplished synthesized by the hydrothermal method, which is relatively facile solution process compared to other vacuum processes. Furthermore, the new insight for a nanostructure synthesis could be provided from the growth mechanism of the TiO_2 nanorods proposed in the potential hydrogen production researches.

List of Publications

1. **Seung-Pyo Hong**, Seong-Il Kim, Seok Su Sohn, Dong Ho Lee, Jang-Yong Yoo, Chang-Sun Lee, Sunghak Lee, and Young-Woon Kim, "In-situ Observation of Dislocation Motions in Strain-based-design Steels under Combined Environment of the Bauschinger Effect and Strain Aging", **Science of Advanced Materials**, 10, 85-88 (2018)

2. **Seung-Pyo Hong**, Seong-Il Kim, Tae-Young Ahn, Soon-Taik Hong, Young-Woon Kim, "Effects of extended heat treatment on carbide evolution in Cr-Mo steels", **Materials Characterization**, 115, 8-13 (2016)

3. Hyo Kyung Sung, Dong Ho Lee, Sunghak Lee, Byeong-Joo Lee, **Seung-Pyo Hong**, Young-Woon Kim, Jang Yong Yoo, Byoungchul Hwang, and Sang Yong Shin, "Effects of C and Si on Strain Aging of Strain-Based API X60 Pipeline Steels", **Metals and Materials International**, 23, 3, 450-458 (2017)

4. Tae-Young Ahn, **Seung-Pyo Hong**, Seong-Il Kim and Young-Woon Kim, "In situ liquid-cell transmission electron microscopy for direct observation of concentration-dependent growth and dissolution of silver nanoparticles", **RSC Advanced**, 5, 82342-82345 (2015)

5. Bon-Woong Koo, **Seung-Pyo Hong**, Seong-Il Kim, Chan S. Kang, Sang-Sub Han, Kyu Hwan Oh, and Young-Woon Kim, "Design and Application of a Novel In Situ Nano-Manipulation Stage for Transmission Electron Microscopy", **Microscopy and Microanalysis**, 21, 298-306 (2015)

6. Bon-Woong Koo, Young Jin Chang, **Seung-Pyo Hong**, Chan Soon Kang, Shin Woong Jeong, Won-Jong Nam, Il-Jeong Park, Young-Kook Lee, Kyu Hwan Oh and Young-Woon Kim, "Experimental measurement of Young's modulus from a single crystalline cementite", **Scripta Materialia**, 82, 25-28 (2014)

7. Shin Woong Jeong, Ui Gu Kang, **Seung-Pyo Hong**, Young-Woon Kim, Wong-Jong Nam, "Aging behavior and delamination in cold drawn and post-deformation annealed hyper-eutectoid steel wires", **Materials Science and Engineering: A**, 586, 171-177 (2013)

8. Jiwon Park, Sung-Dae Kim, **Seung-Pyo Hong**, Sung-Il Baik, Dong-Su Ko, Choong Yeol Lee, Duk-Lak Lee, Young-Woon Kim, "Quantitative measurement of cementite dissociation in drawn pearlitic steel", **Materials Science and Engineering: A**, 528, 4947-4952 (2011)

Curriculum vitae

Updated on Dec. 7th, 2017

Seung-Pyo HONG

Department of Materials Science and Engineering
College of Engineering

Seoul National University

1 Gwanak-ro Gwanak-gu, Seoul

Mobile: +82-10-4701-0133 e-mail: honghong0133@gmail.com
hong0133@snu.ac.kr

Education

- **M.S. and Ph.D.**, (Sep. 2009 ~ Feb. 2018)

  Department of Materials Science and Engineering, Seoul National University

- **B. S.**, (Mar. 2001 ~ Feb. 2009) (Including military service: Apr. 2002 ~ Sep. 2004)

  School of Advanced Materials Engineering, Kookmin University

Research Area

- **Microstructure Analysis with Various in-situ TEM**

  - Straining
    : In-situ observation of deformation behavior of TWIP steels
    : Direct analysis of dislocation dynamics in strain-based steels
  - Heating
    : Microstructure evolution of carbides during long term heat treatment in steels
    : Aging behavior in post-deformation annealed steel wires
  - Manipulation
    : Measuring Young's modulus of single crystalline cementite

- Environmental Stage

■ : Electron beam induced growth and dissolution of silver nanoparticles

■ **Analysis of metals and those defects**

- Microstructural analysis of metals
  : high alloy steels, including invar and stainless steels, and high Mn steels
  : low alloy ferritic steels
  : deformation structure (grain and/or grain boundary analysis)
  : interaction between dislocation and the precipitates in strain-based steels

■ **Mechanical characterization of thin metal sheets**

- Measuring and analyzing the mechanical properties
- Phase identification of the metal alloy sheets

Technical Proficiency

■ **Transmission Electron Microscopy (TEM)**

- Microscopes
  FEI Tecnai F20, Philips CM20, JEOL JEM 3000F, 2100F, 2010F.
- Analytical TEM
  Bright/Dark-field images, HRTEM, Analysis of Selected area electron diffraction (SAED) and Convergent Beam Electron Diffraction (CBED)
- Scanning TEM (HAADF)
- X-ray Energy Dispersive Spectroscopy (EDS)
- TEM sample preparation
  Cross-sectional and plane-view with tripod instrument and with twin-jet electropolishing, Focused Ion Beam (Seiko SMI 3050SE)

■ **Scanning Electron Microscopy (SEM)**

- Microscopes

  Hitachi SU-70, JEOL JSM 6390
- Secondary/Back-scattered electron image (SE, BSE images)

- Electron Backscattered Diffraction (EBSD)

- SEM sample preparation

- **Simulation Tools**

  - Image simulation for microstructural analysis
    Java version Electron Microscopy (JEMS)

- **Deposition Systems**

  - Metal and/or oxide films deposition by e-beam evaporator (Pt, Au, TiO_2 etc.)

- **Analytical Instruments**

  - Probe station for *I-V* measurement
  - Photoelectrochemical property measurements for Solar Water Splitting

- **Image Editing Tools**

  - ImageJ (stacked image generation and editing)
  - DigitalMicrograph (Gatan, TEM image editing), VirtualDub, Camtasia Studio

- **Design Tools**

  - Autodesk Inventor, AutoCAD, Photoshop

Conferences

International:

1. Seung-Pyo Hong, Seong-Il Kim, Ming-zhe Li, Soon-Taik Hong, and Young-Woon Kim, "Investigation of the carbides evolution under extended heat treatment in Cr-Mo steels", **East Asia Microscopy Conference**, Himeji, Japan (2015)

2. Seung-Pyo Hong, Seong-Il Kim, Seok Su Sohn, Dongho Lee, Chang-Sun Lee, Sunghak Lee, and Young-Woon Kim, "Investigation of Dislocation Behaviors by in-situ Heating and Straining TEM stage" **International Union of Materials Research Societies (IUMRS)**, Jeju, Korea (2015)

3. Seung-Pyo Hong, Seong-Il Kim, Tae-Young Ahn, Chang-Sun Lee, and Young-Woon Kim, "Direct Observation of the Strain Aging Effects Using the in-situ

Heating and Straining Stage for TEM", **Microscopy and Microanalysis**, Portland, USA (2015)

4. Seung-Pyo Hong, Tae-Young Ahn, Seong-Il Kim, Yun-Jo Ro, Chang-Sun Lee, Young-Woon Kim, "Observation of Strain Aging Behavior in Strain Based Line Pipe Steels using in-situ Heating and Straining TEM stage", **International Microscopy Congress (IMC)**, Prague, Czech (2014)

5. Seung-Pyo Hong, Tae-Young Ahn, Seong-Il Kim, Woo-Gyeom Kim, Chang-Sun Lee, and Young-Woon Kim, "Effects of heat treatments on precipitates, microstructures and mechanical properties in off -shore structural steels", **Materials Science and Technology**, Montreal, Canada (2013)

6. Seung-Pyo Hong, Tae-Young Ahn, Young-Hwa Oh Woo-Gyeom Kim, Chang-Sun Lee, and Young-Woon Kim, "Investigation of heat treatment effects on microstructures of marine structural steels by in-situ TEM", **East Asia Microscopy Conference**, Chongqing, China (2013)

7. Seung-Pyo Hong, Sung-Il Baik, and Young-Woon Kim, "In-Situ Observation of Deformation of TWIP steels using TEM", **Pacific Rim International Conference on Advanced Materials and Processing (PRICM)**, Hawaii, USA (2013)

Domestic:

1. 홍승표, 안태영, 김성일, 홍순택, 이창선, 김영운, "장시간 열처리에 대한 Cr-Mo 강 내부의 탄화물 거동 분석", **한국전자현미경학회** (2015)

Abstract (in Korean)

물분해 광전극 응용을 위해 수열 합성 방법을 사용하여 TiO_2 nanorods가 FTO; (001), (101), (110) 방위의 단 결정 TiO_2 기판 그리고 *p*-Si 기판에 합성 되었다. 합성 온도와 시간, precursor 및 HCl의 농도 그리고 각기 다른 기판에서의 수열 합성을 통해 TiO_2 nanorods의 성장 메커니즘을 제시했다. 수열 합성 중에 TiO_2 nanorods의 형상은 TiO_2의 각 면의 표면 에너지와 합성 용액의 화학적 반응에 강하게 의존하는데, 이 두 가지 인자들을 동시에 제어할 수 있는 것이 HCl의 농도이며, 농도 변화에 대한 TiO_2 nanorods의 형상 변화를 확인했다. TiO_2 nanorods 형성에 있어서, rod 모양의 형성은 가장 표면 에너지가 낮은 네 개의 {110} 면의 형성과, 가장 표면 에너지가 높은 {001} 면에 의한 우선 방위 성장에 기인한다. 하지만 다양한 합성 인자들의 조절에 의해 표면 에너지에 의한 형상 제어보다 화학적 kinetic이 강하게 작용하면 rod 형상이 아닌 다른 형상으로의 성장이 가능하다. 이때, HCl의 농도 조절은 표면 에너지와 화학적 kinetic을 조절할 수 있는 인자로써 형상 제어에 가장 지배적인 효과를 나타냈다. 이는 용액 내 Cl^- 이온이 TiO_2 {110} 면에 선택적으로 붙어서 {110} 면에서의 성장을 억제하기 때문이며, 나아가 {110} 면을 안정화 시키는 역할을 한다.

또한 광 촉매 특성이 우수한 2D-TMD 물질 중 하나인 MoS_2를 수열 합성으로 TiO_2 nanorods에 decoration해서 PEC 특성을 측정했으며, photocurrent와 overpotential 측면 모두에서 큰 향상이 확인 되었다. HR TEM과 FFT 및 XPS 분석으로부터

수열 합성된 MoS_2의 존재를 확인했고, TiO_2와의 계면에 decoration이 잘 되었음이 확인되었다. UPS 분석으로부터 $MoS_2/TiO_2/p$-Si사이에 heterojunction이 잘 형성되었음을 확인했다.

물분해 광전극 응용을 위한 MoS2/TiO2 이종계면의 미세구조 분석에 관한 연구

키워드: 광 물 분해, **수열 합성**, rutile TiO_2 nanorod**의 성장 거동**, **표면 에너지**, photoelectrochemical performance, 2**차원** MoS_2, heterojunction

홍 승 표